

**MODEL STUDY OF PLATINUM NANOPARTICLE INTERACTIONS WITH
 γ -ALUMINA SINGLE CRYSTAL SUPPORTS**

by

Zhongfan Zhang

BE, Dalian University of Technology, 2004

MS, Beijing University of Aeronautics and Astronautics, 2007

Submitted to the Graduate Faculty of
Swanson School of Engineering in partial fulfillment
of the requirements for the degree of
Doctor of Philosophy

University of Pittsburgh

2012

UNIVERSITY OF PITTSBURGH
SWANSON SCHOOL OF ENGINEERING

This dissertation was presented

by

Zhongfan Zhang

It was defended on

July 25, 2012

and approved by

John A. Barnard, PhD, Professor, Department of Mechanical Engineering and Materials
Science

Brian M. Gleeson, PhD, Professor, Department of Mechanical Engineering and Materials
Science

Jennifer L. Gray, PhD, Assistant Professor, Department of Mechanical Engineering and
Materials Science

Anatoly I. Frenkel, PhD, Professor, Department of Physics (Yeshiva University)

Dissertation Director: Judith C. Yang, PhD, Professor, Department of Chemical and
Petroleum Engineering

Copyright © by Zhongfan Zhang

2012

MODEL STUDY OF PLATINUM NANOPARTICLE INTERACTIONS WITH γ -ALUMINA SINGLE CRYSTAL SUPPORTS

Zhongfan Zhang, PhD

University of Pittsburgh, 2012

Pt/ γ -Al₂O₃ is arguably the most important heterogeneous catalyst system, as it is used in numerous technologically important processes, including oil refining, catalytic converters and fuel cells. Hence, many investigators have studied Pt/ γ -Al₂O₃ both experimentally and theoretically. Yet, a significant gap exists between experiment and theory since theory models well defined finite systems whereas the commercially available γ -Al₂O₃ is polycrystalline with ill-defined morphologies, crystallography and impurities. The goal of this thesis project is to synthesize a model Pt/ γ -Al₂O₃ heterogeneous catalyst system which is in the appropriate size regime for theoretical modeling. The critical challenge of this project is the creation of single crystal γ -Al₂O₃ thin films. To achieve this goal, the growth of single crystal γ -Al₂O₃ thin film on NiAl(110) surface was systematically investigated by oxidation in dry ambient air to determine the optimal oxidation parameters to form a reasonably flat, defect-free, single crystal γ -Al₂O₃ film. We determined that the optimal oxidation condition was 850°C for 1 hour in air that produced an 80 nm thick film with an RMS value of 10 nm. The model Pt/ γ -Al₂O₃ system was produced by e-beam evaporation of Pt nanoparticles onto the surface of the γ -Al₂O₃. We characterized the Pt/ γ -Al₂O₃ by transmission electron microscopy techniques for morphological and electronic structure of the nanoparticles and interfaces, respectively. We provide two feasibility studies of obtaining benchmark parameters that could be used by theorists: (1) the interfacial energy through a Wulff-Kashiew analysis of the supported Pt nanoparticles' shapes

and (2) information on the density of states at the interface using electron energy loss spectroscopy. During the course of this study, we also discovered aspects of NiAl oxidation kinetics in the intermediate temperature regime of 650-950°C where only γ -Al₂O₃ forms, not the thermodynamically stable α -Al₂O₃. For example, crystallinity, epitaxy, and surface roughness of the oxide depends on the oxidation temperature due to temperature-dependent strain and relative diffusion behaviors.

TABLE OF CONTENTS

ACKNOWLEDGEMENTS	XVIII
1.0 INTRODUCTION	1
2.0 BACKGROUND	5
2.1 PLATINUM/ γ -ALUMINA HETEROGENEOUS CATALYST	6
2.2 POLYMORPH OF ALUMINA: γ -ALUMINA.....	9
2.3 HETEROGENEOUS CATALYST DESIGN	12
2.4 MODEL SYSTEM STUDIES OF HETEROGENEOUS CATALYSIS	14
2.5 FORMATION OF SINGLE CRYSTAL γ -ALUMINA FILM	19
3.0 EXPERIMENTAL PROCEDURE	25
3.1 PREPARATION OF THE PLATINUM/ γ -ALUMINA MODEL SYSTEM	25
3.1.1 Formation of the γ -Al ₂ O ₃ : NiAl(110) oxidation	25
3.1.2 Preparation of Pt nanoparticles supported on γ -Al ₂ O ₃	27
3.2 CROSS-SECTIONAL TEM SAMPLE PREPARATION	32
3.2.1 Dual-beam focused ion beam TEM sample preparation.....	32
3.2.2 Conventional TEM sample preparation	35
3.3 CHARACTERIZATION METHODS.....	37
3.3.1 Surface morphology characterization by AFM and SEM.....	37
3.3.2 High-resolution transmission electron microscopy (HRTEM).....	38

3.3.3	High angle annular dark-field (HAADF) STEM	39
3.3.4	Electron energy loss spectroscopy (EELS).....	40
4.0	γ -ALUMINA THIN FILM FORMATION VIA OXIDATION	42
4.1	EXPERIMENTAL RESULTS	42
4.1.1	Macroscopic structure and morphology of γ -Al ₂ O ₃ (111) formation on NiAl(110).....	42
4.1.2	Analytical electron microscopy analysis of γ -Al ₂ O ₃ film structure and epitaxy	46
4.1.3	Interlayer phase separation	58
4.2	DISCUSSION OF γ -ALUMINA FORMATION	62
4.2.1	γ -Al ₂ O ₃ microstructure and orientation at various oxidation conditions	62
4.2.2	Interfacial strain induced evolution of γ -Al ₂ O ₃ growth epitaxy	64
4.2.3	Driving force for phase separation at 750°C 1hr oxidation.....	67
4.3	CONCLUSIONS	69
5.0	INTERFACIAL STUDIES OF THE INTERACTIONS BETWEEN PLATINUM NANOPARTICLES AND γ -ALUMINA SUPPORT.....	70
5.1	CREATION AND CHARACTERIZATION OF MODEL PLATINUM/ γ -ALUMINA SYSTEM	70
5.2	PLATINUM NANOPARTICLES STRUCTURAL RELATION TO γ -ALUMINA SUPPORT.....	74
5.3	EQUILIBRIUM SHAPE CONSTRUCTION OF PLATINUM NANOPARTICLES	80

5.4	PHYSICAL BONDING BETWEEN THE PLATINUM NANOPARTICLES AND γ -ALUMINA SUPPORT	84
5.5	CONCLUSIONS	87
6.0	ELECTRON ENERGY LOSS SPECTROSCOPY STUDY OF PLATINUM NANOPARTICLES ON γ -ALUMINA SUPPORT	88
6.1	ELECTRONIC STRUCTURE OF PLATINUM/ γ -ALUMINA INTERFACE ..	89
6.2	EXPERIMENTAL PROCEDURES.....	90
6.3	RESULTS AND DISCUSSION.....	92
6.4	CONCLUSIONS	100
7.0	SUMMARY AND FUTURE WORK.....	101
	APPENDIX I	104
	APPENDIX II.....	110
	BIBLIOGRAPHY.....	135

LIST OF TABLES

Table 4.1 γ -Al ₂ O ₃ thin film parameters and orientation relation at various oxidation conditions, the error bars denote the standard deviation.....	45
Table 5.1 A comparison between experimental adhesion energy data and density-functional calculated results.	82
Table 5.2 LDA calculated adsorption energies for Pt particles dispersed on monolayer γ -Al ₂ O ₃ with preferred sites (Al, O) were compared with experimental results [74,122].....	84
Table AII.1 Classical rate constants for the growth kinetics of γ -Al ₂ O ₃ on β -NiAl (110) at given temperatures	118

LIST OF FIGURES

Figure 2.1 Pt ₁₀ bound to surface O atoms at elevated temperatures on γ -Al ₂ O ₃ surface [39].	7
Figure 2.2 (a). Commercial γ -Al ₂ O ₃ polycrystalline has an irregular surface structure. (b). The spinel γ -Al ₂ O ₃ crystal structure consists of an almost cubic-close-packed array of oxygen ions, with aluminum ions at the tetrahedral and octahedral sites.....	8
Figure 2.3 Au particle size and shape on the titania-support for CO oxidation, 30×30 nm [65]..	15
Figure 2.4 HRTEM micrograph of a Rh particle on MgO(001) in (110) view [5].....	15
Figure 2.5 In situ TEM image of a Cu/ZnO catalyst exposed to 1.5 mbar of H ₂ at 220 °C, (a). The electron beam is parallel to the [011] zone axis of the copper, (b). The corresponding Wulff constructions of the Cu nanocrystals [60].	16
Figure 2.6 (a). Atomic-resolution images of crystalline nanosize Pd clusters. (b). Cross section of a Pd cluster based on the Wulff construction using theoretical surface energies for the three low-index Pd surfaces [74].	16
Figure 2.7 (a). The height measurements on an oxidized NiAl(001) surface. (b). STM images of the surface oxidized after 600 L of oxidation at 1025 K followed by 1 h of annealing [87]......	21
Figure 2.8 STM image of an early stage oxidized NiAl(110) surface(500Å×500Å) [90].	22
Figure 2.9 DFT (a) and STM (b) based model for the ultrathin aluminum oxide film on NiAl(110) [43].	23

Figure 3.1 (a). Regular $\theta/2\theta$ XRD scan of as-prepared NiAl sample, (b). Texture XRD scan of the the bulk sample confirm NiAl(110) crystallinity and orientation.....	26
Figure 3.2 SEM images of the polished NiAl(110) surface, (a). Mechanical polish to 0.01 μ m, (b). after vibration polishing.....	27
Figure 3.3 (a). HAADF image of Pt NPs on ultra-thin carbon film formed by electron beam evaporation of Pt at 2 \AA /s at 500 $^{\circ}$ C heating stage for 3 sec. (b). Corresponding size histogram of Pt NPs.	28
Figure 3.4 HAADF images and corresponding size distribution histogram of Pt NPs on ultra-thin carbon film deposited by electron beam evaporation at various parameters on heating stage, (a). 293K 0.1 \AA /s for 0.1s, (b). 293K 0.1 \AA /s for 30s, (c). 773K 2 \AA /s for 3s, (d). 973K 2 \AA /s for 4s	30
Figure 3.5 HAADF image and corresponding HRTEM image of Pt NPs on ultra-thin carbon film deposited by electron beam evaporation at 700 $^{\circ}$ C at 2 \AA /sec and post annealed at 850 $^{\circ}$ C for 1h.	31
Figure 3.6 DB-FIB cross-sectional sample preparation procedure of the Pt NPs/ γ -Al ₂ O ₃ /NiAl system: (a). Protective layer deposition of platinum film, (b). Bulk Milling by Ga+ ions, (c). “U” cut (d). Omniprobe weld, (e). Sample lift out, (f). Transference to Omnigrid, (g). Sample welded to grid, (h). Further polishing at low 2 keV Ga+ ions, (i), Final thinned cross-sectional TEM sample.	33
Figure 3.7 (a) BF TEM image of the Cross-sectional TEM sample of the NiAl/ γ -Al ₂ O ₃ where the γ -Al ₂ O ₃ was formed by NiAl(110) oxidized at 850 $^{\circ}$ C for 1hr, (b) cross-sectional HRTEM image after Pt NPs are deposited onto the γ -Al ₂ O ₃ showing ~3-5 nm dispersed on the oxide surface.	34
Figure 3.8 Cross-sectional TEM image of after nanomilled Pt/oxide interface.	35

Figure 4.1 $\theta/2\theta$ XRD scans for NiAl(110) specimens oxidized at different temperatures for 1 or 2 hrs: γ -Al₂O₃ (222) and (444) peaks were observed; fine scan from 37 to 42 deg was applied to 750°C 2hrs sample which also showed a γ -Al₂O₃ (222) peak at 39.5 deg. 43

Figure 4.2 SEM images of oxidized NiAl(110) surface at various oxidation conditions in dry air 44

Figure 4.3 AFM images of oxides surface morphology under different oxidation conditions..... 45

Figure 4.4 Cross-sectional TEM images of the γ -Al₂O₃ film by NiAl oxidation at 850°C 1hr. (a). Continuous oxide film formed on NiAl surface projected along NiAl[110] || γ -Al₂O₃[211]. (b). Oxide film HRTEM image conserve γ -Al₂O₃ lattice structure with Fast Fourier transformation (FFT). 47

Figure 4.5 Cross-sectional HRTEM image of 850°C 1hr oxidized NiAl/ γ -Al₂O₃ interface: (a). Interface of (111) γ -Al₂O₃ film on (110)NiAl. (b). NB-EDP from upper γ -Al₂O₃ film, (c). SAD from NiAl/ γ -Al₂O₃ interface. 48

Figure 4.6 Schematic diffraction pattern of superimposed NiAl[110]|| γ -Al₂O₃ [211] 49

Figure 4.7 HAADF image (a) of 850°C 1hr sample NiAl/ γ -Al₂O₃ interface and corresponding O-K edge (b), Ni-L edge (c) EELS mapping, no nickel is detected inside the oxide film. 50

Figure 4.8 EELS line scan spectrum across γ -Al₂O₃/NiAl interface indicated the probable interface (1Å probe size) and the absence of Ni inside of the oxide film. 51

Figure 4.9 EELS Ni L₂₃ edge spectrum from interface and bulk NiAl 52

Figure 4.10 EELS O K₁ edge from γ -Al₂O₃ film and interface. 52

Figure 4.11 Cross-sectional HRTEM image of 650°C 2hr oxidized NiAl/ γ -Al₂O₃ interface, 53

Figure 4.12 Top view schematic rigid atom matching of 650°C 2 hrs oxidized γ -Al₂O₃(111) overlay on NiAl(110) with γ -Al₂O₃[211]||NiAl[113] axis matching. γ -Al₂O₃ (111)[1

10] NiAl(110)[$\bar{1}\bar{1}\bar{1}$] with γ -Al ₂ O ₃ [$\bar{1}\bar{0}\bar{1}$] 5.26° away from NiAl[001] can be achieved which is the KS O.R.	54
Figure 4.13 Cross-sectional HRTEM image of 750°C 2hr oxidized γ -Al ₂ O ₃ NiAl interface,.....	55
Figure 4.14 (a). NB-EDP from 750°C 2hr oxidized γ -Al ₂ O ₃ film confirmed γ -Al ₂ O ₃ with (111) twin defects, (b). Intensity profile of NB-EDP from the lower dotted area shows the twin diffraction with respect to ($\bar{1}\bar{1}\bar{1}$) mirror plane. (c). Schematic γ -Al ₂ O ₃ (111) twin diffraction pattern at [011] zone axis.....	56
Figure 4.15 Cross-sectional TEM images γ -Al ₂ O ₃ film structure from 950°C 1hr oxidation. (a).BF image of ~300nm γ -Al ₂ O ₃ film on NiAl(110), with SAD from γ -Al ₂ O ₃ film (upper corner) and NiAl substrate (lower corner) inset. (b). γ -Al ₂ O ₃ DF image of (222) diffraction spot showed textured polycrystalline with preferred in-plane (111) orientation. (c) and (d). Corresponding DF images using γ -Al ₂ O ₃ (440) and (400) diffraction spots indicated nano sized oxides formation.....	57
Figure 4.16 Cross-sectional TEM image of 750°C1hr oxidized NiAl/ γ -Al ₂ O ₃ interface showed Ni ₃ Al precipitation with corresponding Ni-K edge (b) and Al-K edge (c) EDS mapping.....	58
Figure 4.17 Relative concentration profiles of Ni, Al and O elements across NiAl/ γ -Al ₂ O ₃ interface of 750°C 1hr oxidized NiAl. (a). EDS line scan across Ni ₃ Al separation region, (b). EDS line scan across non-phase separation region, (c). Cross-sectional TEM BF image of 750°C 1hr oxidized NiAl(110), (d). Large cavities formation was observed along the NiAl/ γ -Al ₂ O ₃ interface.....	59
Figure 4.18 HRTEM interface image of NiAl and Ni ₃ Al precipitate at 750°C 1hr oxidation indicated NiAl(110)[001] Ni ₃ Al($\bar{1}\bar{1}\bar{1}$) [011] epitaxy: (a). FFT pattern of NiAl substrate. (b). FFT pattern of Ni ₃ Al phase.....	60

Figure 4.19 Epitaxy stability diagram of γ -Al₂O₃ growth as a function of r and l , KS transforms into NW O.R. with l increasing, a γ -Al₂O₃ {111} twinning defects regime is expected along the KS/NW boundary. 66

Figure 5.1 Typical TEM imaging of Pt NPs seating on the γ -Al₂O₃ support are shown in (a)~(d). The corresponding histogram of Pt NPs size distribution from HAADF and HRTEM measurements shows a 2~5nm distribution of Pt particles. 71

Figure 5.2 HAADF image (a) and HRTEM image (b) shows the Pt NPs is intimately contact with the γ -Al₂O₃(111) support with Pt(111)|| γ -Al₂O₃(111), interface matching is Pt(220)|| γ -Al₂O₃(440). 72

Figure 5.3 (a). Pt NP with orientation relation of Pt(100)[011]|| γ -Al₂O₃(111)[211], and interfacial epitaxy: Pt(220) || γ -Al₂O₃(440), (b). 3 dimensional truncated octahedron of Pt, the beam direction is indicated as the solid arrow, (c). Side view of the Pt NP. 74

Figure 5.4 ES Pt NP with high index (062) exposing surface: Pt(111)[110] || γ -Al₂O₃ (111) [211]. 75

Figure 5.5 (a). HRTEM images of Pt NP with (110) facets and corresponding FFT (upper right), with epitaxy Pt(100) || γ -Al₂O₃(111) and Pt[011]|| γ -Al₂O₃[211], and interfacial planes Pt(220) || γ -Al₂O₃(440) , (b). schematic of the Pt truncated octahedron with (110) facets; the beam direction is indicated as the solid arrow and (c) corresponding schematic of side view. 76

Figure 5.6 (a). Pt NP with high index (062) facet: Pt(062)[013] || γ -Al₂O₃ (111) [211], interfacial planes are Pt(100)|| γ -Al₂O₃(110), (b), schematic diagram of the Pt NP on γ -Al₂O₃. 78

Figure 5.7 The equilibrium shape of an FCC single crystal at zero temperature obtained via the Wulff construction from the computed surface energies [119]. 79

Figure 5.8 Schematic diagram of the observed Pt particle with equilibrium shape seating on γ - $\text{Al}_2\text{O}_3(111)$ support. h_i and h_{AB} are the normal distances from Wulff point O to the surfaces i and the interface AB. $h_{AB} > 0$ means Wulff point O is above the support. .	81
Figure 5.9 Experimental results vs LDA-DFT calculated adsorption energies for Pt NPs on γ - Al_2O_3 with Al, O and sites [74,122].	85
Figure 6.1 HAADF images Pt NPs directly supported on γ - Al_2O_3 . Due to γ - Al_2O_3 is a low Z oxide, the contrast contributed by γ - Al_2O_3 is relatively low compared with Pt NPs..	90
Figure 6.2 The HAADF image of Pt particles with corresponding EELS spectra. The arrow indicates the position where EELS line scan spectrum was taken. O K edge EELS line scan spectra were recorded point by point across the Pt/ γ - Al_2O_3 interface with a step of 4.2Å.	93
Figure 6.3 O K edge EELS line scan spectra obtained from the Pt/ γ - Al_2O_3 interface and γ - Al_2O_3 support.	93
Figure 6.4 Standard O K edge EELS spectrum from α - Al_2O_3 acquired from EELS ATLAS, K edge start 530 eV, peak at 536 eV [137].	94
Figure 6.5 The measured EELS spectra from the Pt/ γ - Al_2O_3 interface indicated representative Pt M_4 and Al $L_{2,3}$ peaks. O K prepeak observed at various Pt/ γ - Al_2O_3 interfaces at energy edge 525.5 eV is compared with the typical O K spectrum collected at non-symmetrical (interface1) and more symmetrical (interface 2) Pt particle and γ - Al_2O_3 interfaces. The oxygen K edge peak spectrum as well as the Al $L_{2,3}$ and Pt M_4 edge peak spectrum were collected using a 0.1 eV energy resolution with an exposure time of 3 sec from various interfacial regions.	96
Figure 6.6 EELS of O K edge (Right) acquired from beam damaged area under STEM (Left)..	97
Figure 6.7 Comparison of O K edge EELS acquired from beam damaged area and interfacial regions under STEM.	98

Figure AI.1 (a). Illustration of contact angle of a liquid drop L on a solid substrate S with partially wetting angle θ . (b). Schematic diagram illustrating the Wulff construction yields the equilibrium shape polyhedron of crystal (inner dashed line) which are normal to the radius vectors (outer light dashed line), with corresponding polar plot of surface free energy (solid line) [73]. 105

Figure AI.2 Schematic diagram of reconstructed ES Pt NP on γ - Al_2O_3 support. h_i and h_{AB} are the normal distances from the Wulff point O to the facet i , and the interface AB , respectively. $h_{AB} < 0$ implies that the Wulff point is located within the support. ... 106

Figure AII.1 Cross-sectional TEM image of 750°C 1 h oxidized NiAl(110): (a). Ni_3Al phase formation with a large cavity portion at the interface, (b) Ni-K edge EDS mapping, (c) Al-K edge EDS mapping [9]..... 111

Figure AII.2 Cross-sectional TEM image of 750°C 2 h oxidized NiAl/ γ - Al_2O_3 interface with corresponding EDS elemental mapping confirmed no phase formation..... 112

Figure AII.3 Diffusion profile and boundary conditions of NiAl alloy oxidation to form a continuous γ - Al_2O_3 oxide layer: (a) no intermediate phase separation at the metal/oxide interface, (b) Ni_3Al phase formation at the interface. See text for a definition of term shown in the schematics..... 113

Figure AII.4 XRD scans of various temperature oxide thin films grew on NiAl(110) 117

Figure AII.5 Thermogravimetric analyses of NiAl (110) early stage oxidation at 750 (a), and 850 °C (b) shows an ideal parabolic growth, the Arrhenius diagrams of $\log k_p$ vs $1/T$ for oxidation of NiAl (110) was compared with former NiAl oxidation results (c). 118

Figure AII.6 Growth kinetics of γ - Al_2O_3 on NiAl(110) alloy at 650°C obey an inverse-logarithmic ($1/x$ vs. $\ln t$) behavior at the initial stage when $x < x_I$ (a), and transit into the parabolic (x^2 vs. t) regime at thicker regime when $x > L_D$ [25]..... 120

Figure AII.7 Ni-Al binary phase diagram..... 122

Figure AII.8 Interfacial composition of Al (N_{Al}^i) profile compared with the equilibrium composition of γ' phase formation ($N_{Al}^{\beta/\gamma'}$) at corresponding temperatures. (a). At 650 °C, N_{Al}^i was solved by inverse-logarithmic kinetics according to equation (17); (b) and (c), at 750 and 850°C, N_{Al}^i was obtained from parabolic kinetics according to equation (18). 125

Figure AII.9 The Al flux arrives at the Ni₃Al/ γ -Al₂O₃ interface through the Ni₃Al phase is shown as a function of subsurface γ' layer thickness at 750 and 850°C. 127

Figure AII.10 Schematics of Ni₃Al phase formation and recession process at the oxide subsurface. See text for a definition of term shown in the schematics. See text for a definition of term shown in the schematics. 128

Figure AII.11 Kinetic stability diagram of γ' phase formation as a function of d_{cr} and time indicates the stable/unstable zone of γ' at oxidation temperature of 750 and 850°C. 131

ACKNOWLEDGEMENTS

I would like to gratefully and sincerely thank my mentor, Dr. Judith C. Yang, for her support and guidance during my studies at University of Pittsburgh. She advised me to overcome many obstacles of my research and encouraged me to think independently. Her extensive knowledge in materials science and electron microscopy led me to the success of research. Moreover, her dedication to research and teaching educated me how to be a dedicated researcher, a warm mentor, and a genuine person.

I would also like to thank our senior group member and my friend, Long Li, for his guidance and assistance in my graduate career. He provided me the foundation for becoming an experimentalist and advised me to go deeper with my research.

I would like to acknowledge the Department of Mechanical Engineering and Materials Science at University of Pittsburgh, especially my doctoral committee, Dr. Gleeson, Dr. Barnard, Dr. Gray and Dr. Frenkel, for their valuable discussions and active participation. In particular, I would like to thank Albert Stewart, Matthew France, Susheng Tan, Cole Van Ormer for their training, analytical services, patience, and their hard work. I am also gratefully acknowledge the scientific and technical assistance of Jianguo Wen, Mike Marshall (University of Illinois at Urbana-Champaign), Junhai Liu, Rocco R Cerchiara (Fischione Instruments), Tom Nuhfer (Carnegie Mellon University), Eric Stach, Dong Su (Brookhaven National Laboratory).

The completion of this dissertation would not be possible without help from my friends and colleagues. I would like to thank Yihong Kang, Keeyoung Jung, Malay Shah, Mike Melia,

Zhenyu Liu, Wei Zhao, Xiahao Sang, Andreas Kulovits, Mengjin Yang, Xu Liu, Mingjian Hua, Chao Fang as well as Tom Gasmire from the Chemistry machine shop. I would also like to express my appreciation and respect to Dr. Ken Goldman for his considerate guidance and help.

Finally, and most importantly, I would like to thank my wife, Yan, who always encourages me and accompanies me to come through the experience of graduate school.

Pittsburgh, Pennsylvania, March 2012

Zhongfan Zhang

1.0 INTRODUCTION

Heterogeneous catalyst materials are nanometer-sized metal nanoparticles (NPs) that are supported on a low Z material, such as oxides. Though catalysis is critical to a wide variety of essential technologies, the properties of such ensembles of atoms, for all but the most special cases, remain very poorly defined. It remains beyond our current understanding to predict the local structure due to the support and adsorbate interactions and their impact on their chemical properties. Of particular importance is the role of the metal NP/support interface, since it is well known that the selection of support material will dramatically impact the chemical behavior of the NPs [1–6]. In heterogeneous catalyst, it has been widely recognized that the size, structure and shape are the major factors that have significant effects on their catalytic activity and selectivity [2,7–11]. The application conditions of catalysts are usually under severe environments with high gas pressure during reactions. In order to maintain the nanoclusters with the high specific surface area and high activity, a strong bonding between the support and particles will be beneficial to result in a strong thermal stability [12–15]. Therefore, the physical and electronic states at the particle/support interface will also be critical to understand and interpret its stability. Furthermore, recent experiments demonstrate that anomalous behavior in supported NP systems are support-dependent, being strongly evidenced on some supports and essentially absent on other supports [16]. For the catalyst design, the ability to control the dispersion, morphology and stability of the NPs on its oxide-support is of the most importance

where the nature of the metal-support interaction is critical to understand. It therefore remains a significant need to fundamentally understand and predict the local structure of the NP/oxide system and the role of the interface on the structural and electronic features that control catalytic properties [10,17–19].

Many recent theoretical studies have provided significant insights as to the origin of the support influence on catalyst structure and properties, but are limited to exceptionally well-defined model systems, where crystal orientations are pre-defined with no impurities present. Real catalyst systems are polycrystalline with various impurities which are highly depending on the synthesis method and/or commercial supplier. Hence, only a few single crystal model catalyst systems were examined, where the selection was based on the availability of their single crystal form, to resolve the nanoparticle/support structure and shape relations that can be directly compared to the theoretical simulations, and thus guide the design of optimal heterogeneous catalysts [7,18–20]. In the present study, the goal is to bridge the gap between theoretical and experimental studies through preparation and study of a model heterogeneous catalyst system. The most arguably, technological important heterogeneous catalyst system, Pt NPs supported on γ -Al₂O₃, is systematically studied. Pt NPs dispersed on γ -Al₂O₃ oxide represents the most popular heterogeneous catalyst used in fuel cells, gas sensor applications and the chemical refining industry [7,9,21,22]. Among all of the catalysts, platinum (Pt) nanoparticles dispersed on γ -Al₂O₃ oxide is, arguably, the most technological important catalyst system. It shows the highest efficiency in oxygen reduction reaction (ORR) that is the critical heterogeneous catalyst in a fuel cell. It is also used for gas sensor applications and the oil refining industry [7,9,21,22]. In addition, platinum catalysts have been shown to enhance the activity of electro-oxidation of carbon monoxide (CO) and promote the oxidative conversion of methane to a methanol to

promote the natural gas applications in the fuel cell industry [23,24]. Pt is widely used in the catalytic converter of the auto's exhaust systems to combine carbon monoxide (CO) and unburned fuel with oxygen to form (CO₂) and water vapor (H₂O) [21,25]. Moreover, Pt is also used as a catalyst in the production of sulfuric acid (H₂SO₄) and in the cracking of petroleum products [26]. Pt is one of the most important heterogeneous catalysts, and, hence, extensively studied by materials chemists experimentally and theoretically [5,7,19,23,27]. .

In this work, the structural behavior of Pt on γ -Al₂O₃ support within the mesoscopic size regime of 1.6 to 5 nm will be ascertained by HRTEM. It is well known that support selection may alter catalytic performance significantly, and, hence, the nanoparticle support interaction must play a role in determining the catalytic behavior overall. Characterization of the atomic and electronic arrangements of the nanoparticle/oxide interface through primarily transmission electron microscopy (TEM) methods, including high resolution TEM (HREM), scanning transmission electron microscopy (STEM) and electron energy loss spectroscopy (EELS) will also be performed to understand and interpret the Pt NPs shape, epitaxial relationship with the oxide support, as well as interfacial electronic density of states . These are critical issues in understanding the nanoparticles' catalytic activity, selectivity and lifetime.

Commercially available γ -Al₂O₃ are small-grained and polycrystalline. To produce single crystal γ -Al₂O₃ , we oxidized NiAl(110). A systematic oxidation study of NiAl(110) alloy was performed to synthesize a flat single crystal γ -Al₂O₃ film as the catalyst support, where the temperatures ranged from 650 to 950°C in a dry air atmosphere or low pressures of oxygen (10⁻⁸ ~ 10⁻⁴ atm) for 1 or 2 hours, where it was found that oxidation of β -NiAl(110) at 850°C for 1 hour in dry air produced the best crystallinity of γ -Al₂O₃ with relative flat surface roughness.

This systematic study also led to new insights into the oxidation kinetics of NiAl. To create the Pt/ γ -Al₂O₃ model system, Pt nanoparticles (2 to 5nm) are deposited onto the γ -Al₂O₃ surface by electron beam evaporation in ultrahigh vacuum.

The format of the current study is as follows: Chapter 2 is the relevant background information, including previous theory and experiments on the structural characterization of heterogeneous catalyst systems, as well as an introduction to the phases of alumina and NiAl oxidation; Chapter 3 describes the experimental procedure for creating the γ -Al₂O₃ film and the Pt/ γ -Al₂O₃, as well as the methods and tools used for cross-sectional TEM sample preparation and studies; Chapter 4 focuses on the experimental characterization of the oxide film formed on the (110)NiAl after systematic oxidation, the cross-sectional TEM results of the NiAl/ γ -Al₂O₃ interface where the γ -Al₂O₃ growth epitaxy with respect to the NiAl substrate is discussed; Chapter 5 presents the cross-sectional TEM results of the Pt/ γ -Al₂O₃, including the evaluation of the interfacial adhesion energy using the Wulff-Kaischew theorem [28,29]; Chapter 6 presents the electron energy loss spectroscopy study at the Pt/ γ -Al₂O₃ interface where changes in the O-K EELS spectra indicates changes in the density of states and shift of the Fermi energy; Chapter 7 summarizes this body of work and suggests future directions. The potential of the development of the model γ -Al₂O₃ includes the understanding of the supports effects to electronic structure, morphology, and preferred anchoring sites which all play critical roles in the complexity of heterogeneous catalysis.

2.0 BACKGROUND

A catalyst enables a chemical reaction to proceed at a faster rate or under low temperature conditions. In the past century, heterogeneous catalysis are used in numerous chemical industries, such as petroleum refining, natural gas processing, polymers manufacturing as well as environmental protections [30–34]. Oxide supported metal particles represent a typical heterogeneous catalyst system that has a wide range of applications, such as chemical fabrication and exhaust control in automobiles. The main advantage of using heterogeneous catalyst is due to its convenience of application, being a solid material, it is much easier to separate from the gas or liquid reactants and products of the overall chemical reactions. Most solid catalysts consist of an active phase, often an expensive transition metal, finely dispersed onto a high-surface-area porous support. The key of the heterogeneous catalyst involves the active sites of the catalyst at the surface of solid materials. The catalyst typically provides a high specific surface area (e.g. $10 \sim 1000 \text{ m}^2\text{g}^{-1}$) to maximize the number of active sites for catalytic reaction. In heterogeneous, it has been widely recognized that the size, structure and shape are the major factors that have significant effects on their catalytic activity and selectivity [2,7–10]. The ability to control the shape, size and stability of oxide-supported metal catalysts is a primary goal of catalyst synthesis where the nature of the metal-support interaction is a one of the most critical enabling components [10,17–19].

2.1 PLATINUM/ γ -ALUMINA HETEROGENEOUS CATALYST

Platinum nanoparticles based catalyst shows the highest efficiency in oxygen reduction reaction [1]. Pt dispersed on γ -Al₂O₃ oxide represents the most famous and commonly used heterogeneous catalyst in fuel cell, gas sensor and chemical refining industry [2-4]. Numerous studies have been devoted to elucidating the critical parameters that affect the Pt catalytic performance such as their size, interaction with the support and oxidation state(s) [5,7,19,23,27]. The interaction of Pt particles with the γ -Al₂O₃ oxide support can alter the electronic properties of the metal and can play a critical role in determining particle morphology and maintaining dispersion.

The γ -Al₂O₃ support impacts the Pt nanoparticles shape and structure. For example, the surprising behavior of the negative thermal expansion (NTE)—the marked contraction of the Pt-Pt bonding distances with increasing temperature—was found in the γ -alumina catalyst system [16]. Also, Pt nanoclusters were found to exhibit size-dependent crystallinity where the size range between amorphous to crystalline structure depends on the support [35].

Dispersion of the precious metal (e.g., Pt, Pd, and Rh), which are the most widely used industrial catalyst materials, on the oxide support is an especially critical factor because of the expense of the metal. Several recent investigations suggested that the defect structure of the oxide acts as pinning sites for the metal nanoparticles and thus sustains dispersion. Koningsberger and co-workers revealed that specific interactions between “defect sites” of γ -Al₂O₃ and Pt clusters play an essential role of anchoring where a Pt-O bonding was suggested for the X-ray study [36]. By using nuclear magnetic resonance spectroscopy, Ja Hun Kwak et al., revealed that the unsaturated penta-coordinate Al³⁺ (Al³⁺ pentahedral coordination sites) centers present on the (100) facets of the γ -Al₂O₃ surface are the anchoring sites of the catalytically

active Pt. In addition, Pennycock and co-workers reported that oxygen vacancies are the anchoring sites of mono-atomically dispersed Pt on γ -Al₂O₃ as seen in high angle annular dark-field scanning transmission electron microscopy (HAADF STEM) images [37,38].

Meanwhile, theoretical simulations have been reported on the γ -Al₂O₃ surface structure, Pt/ γ -Al₂O₃ interfacial structure, the supported Pt nanocluster fluctuations, bond-lengths changes, and charge transfer on the γ -Al₂O₃ support. [2,37,39–41]. Interfacial energy and adhesion energy between the NPs and their support were also quantitatively studied by theoretical calculations [39,42]. Theoretical simulations have been extensively conducted to resolve the nanoparticle/support structure, shape relations and preferred anchoring sites on a single crystal support [17–20,41]. Figure 2.1 shows a Pt₁₀ cluster motion under elevated temperatures to be thermally stabilized on the oxygen sites [39].

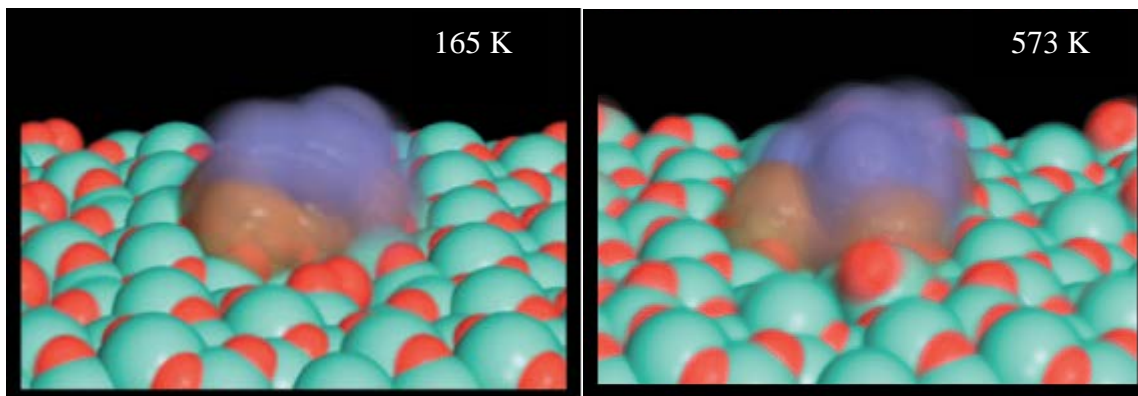


Figure 2.1 Pt₁₀ bound to surface O atoms at elevated temperatures on γ -Al₂O₃ surface [39].

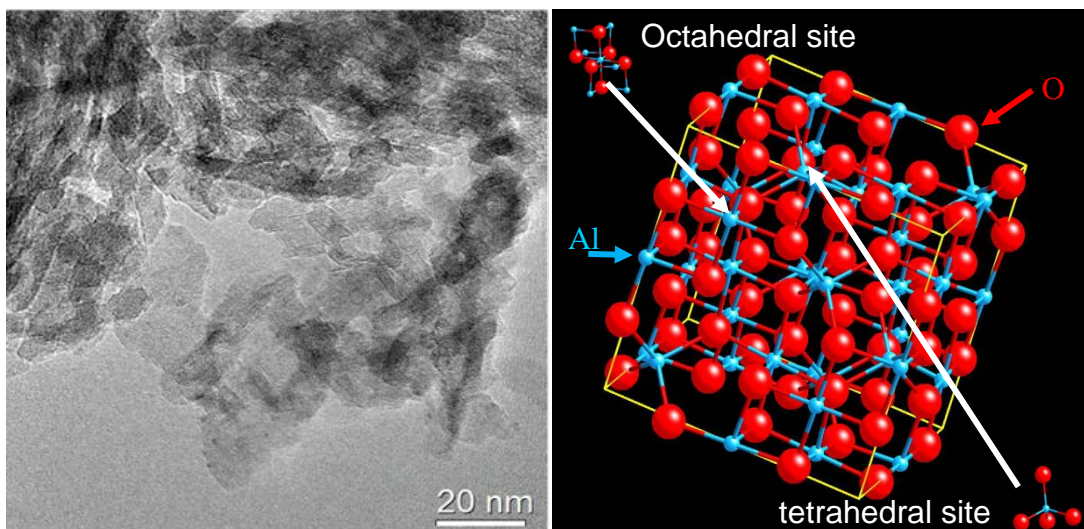


Figure 2.2 (a). Commercial γ - Al_2O_3 polycrystalline has an irregular surface structure. (b). The spinel γ - Al_2O_3 crystal structure consists of an almost cubic-close-packed array of oxygen ions, with aluminum ions at the tetrahedral and octahedral sites.

Numerous theoretical simulation efforts on the physics and chemistry effects of support-nanoparticle interactions have been reported [41,43]; however, all of these simulations assume single crystal γ - Al_2O_3 with specific orientations and no impurities. Commercially available γ - Al_2O_3 is polycrystalline, irregular in shape, and contains impurities (Figure 2.2). Though extensive research efforts seeking to elucidate the origins of the catalytic properties of such supported catalysts have been and continue to be conducted, fundamental understandings of their properties and catalytic mechanisms remain far from complete [44]. Thus, the creation of single crystal γ - Al_2O_3 thin films is essential for the direct comparison between experiments and theoretical simulations on Pt/γ - Al_2O_3 , which will guide the development of optimal heterogeneous catalyst materials of this important catalyst system.

2.2 POLYMORPH OF ALUMINA: γ -ALUMINA

Aluminum oxide (alumina, Al_2O_3) exists in many metastable polymorphs besides the thermodynamically stable α - Al_2O_3 (corundum form). Amongst the numerous metastable (transient) polymorphs of alumina (e.g. amorphous, γ , δ , κ , η , θ), γ -Alumina (γ - Al_2O_3) is perhaps the most advanced alumina material with a variety of applications such as adsorbents, catalysts or catalyst carriers, thermal and semiconductor coatings, and soft abrasives in the automotive and petroleum industries, due to its distinctive chemical, electrical, mechanical and thermal properties [45–49].

In the semiconductor and optical industry, because of its moderate dielectric constant (~ 10) and thermodynamic stability, well-ordered γ - Al_2O_3 layer is expected to be used either as a thick oxide or as a thin buffer barrier when combined with amorphous or epitaxial oxides of higher dielectric constants. An attractive feature of this material is that, in contrast to most high- k materials for which higher dielectric constants usually come at the expense of a narrower band gap, and consequently lower barrier height for electrons and holes which determines leakage current, γ - Al_2O_3 has a band gap similar to SiO_2 and a dielectric constant that is double that of SiO_2 . Thus, γ - Al_2O_3 gate oxides had been used in metal oxide semiconductor (MOS) devices in the early developments of the integrated circuit and infrared (IR) image sensors [50–53]. In addition, Al_2O_3 thin films have been used as a high temperature protective coating against corrosion [54], mechanical wear and as an insulating films in semiconductor devices [55].

The usefulness of this oxide can be traced to a favorable combination of its textural properties, such as surface area, pore volume, and pore size distribution and its acid/base characteristics, which are mainly related to surface chemical composition, local microstructure,

and phase composition. Nevertheless, the well chemical and hydrothermal stability of $\gamma\text{-Al}_2\text{O}_3$ under chemical reactions are still the critical points for its extensively catalytic applications.

The structure of $\gamma\text{-Al}_2\text{O}_3$ is a cubic defective spinel structure, whose experimental unit cell is illustrated in Figure 2.2b. The spinel structure (sometimes called garnet structure) is named after the mineral spinel (MgAl_2O_4); the general composition is AB_2O_4 . It is essentially cubic of 56 atoms per unit cell, with the O - ions forming an fcc lattice. The cations (usually metals) occupy 1/8 of the tetrahedral sites and 1/2 of the octahedral sites and there are 32 O-ions in the unit cell. The spinel structure is very flexible with respect to the cations it can incorporate [56].

AB_2O_4 is represented by a $2 \times 2 \times 2$ array of an fcc packed oxygen subcell, with the A and B cations occupying the $8a$ tetrahedrally and the $16c$ octahedrally coordinated interstitial sites (Figure 2.2b) [57]. The symmetry of the spinel structure is described by the $Fd\bar{3}m$ space group (No. 227), which is a maximal subgroup of the $Fm\bar{3}m$ group. It is sometimes useful to describe the spinel as a layered structure on the $\{111\}$ planes packing of the oxygen anion layers form an ABCABC sequence, whereas the packing of the aluminum cations can be described by two types of alternating layers: either (i) layers containing only octahedrally coordinated cations or (ii) mixed layers containing both octahedrally and tetrahedrally coordinated cations. The commonly accepted structural model of $\gamma\text{-Al}_2\text{O}_3$ is related to that of ideal spinel, and it is assumed to contain oxygen ions in $32e$ Wyckoff positions, which are approximately close packed, while $21\frac{1}{3}$ aluminum cations (to satisfy Al_2O_3 stoichiometry) are distributed over the $16c$ octahedral and $8a$ tetrahedral sites. In $\gamma\text{-Al}_2\text{O}_3$, $8/3$ aluminum vacancies have been assumed to be randomly distributed over the tetrahedral and octahedral sites, so that the cation sublattice is

partially disordered as compared to an ideal spinel. Despite this disorder vacancy, the symmetry relations between the equivalent cation positions remain those of the $Fd\bar{3}m$ space group.

The defective nature derives from the presence of only trivalent Al cations in the spinel like structure, i.e., the magnesium atoms in the ideal spinel $MgAl_2O_4$ are replaced by aluminum atoms. The oxygen lattice is built up by a cubic close-packed stacking of oxygen layers, with Al atoms occupying the octahedral and tetrahedral (Mg^{2+}) sites. To satisfy the γ - Al_2O_3 stoichiometry, some of the lattice positions remain empty (vacancies), although their precise location is still controversial [48,56]. The defective spinel structure contains vacancies as a regular part of the crystal. If all Mg^{2+} is converted into Al^{3+} , charge balance requires a net formula of $Al_{21,33}O_{32}$ per unit cell and this means that 2.67 sites must be vacant, and that is the reason it is called a defective spinel. In a way, the composition is now $Al_{21,33}Vac_{2,67}O_{32}$; Their unit cell could be considered as having lots of vacancies as an integral part of the structure in γ - Al_2O_3 , the aluminum ions are considered to be arranged randomly on the octahedral and tetrahedral sites. A formula for this structure can be written:



where \square represents vacant cation sites, and x and y are the fraction of occupied tetrahedral and octahedral sites, respectively, such that $(x + 2y) = 8/3$, to preserve stoichiometry. By using powder x-ray diffraction method, Shirasuka et al., suggested that 62.5% of the aluminum ions occupy two 16-fold octahedral sites and assumed the remaining aluminum ions to be distributed equally over the eight-fold tetrahedral sites [58]. The high percentage of octahedral sites could also be compared with nuclear magnetic resonance (NMR) spectroscopy revealed coordinatively unsaturated Al^{3+} centers [i.e., the penta-coordinate Al^{3+}] on the γ - Al_2O_3 surface as the anchoring sites for Pt [41].

2.3 HETEROGENEOUS CATALYST DESIGN

The key attributes of heterogeneous catalysis with excellent performance could be summarized as following [30,59],

- The catalyst should exhibit good selectivity for production of desired reaction and minimal production of undesired byproducts;
- The catalyst could achieve adequate rates of reaction at desired reaction conditions of process;
- The catalyst should have a good stability to maintain a high specific surface area at reaction conditions over a long period of time;
- The catalyst should have good accessibility of reactants and products to the active sites.

In heterogeneous catalysis design development, it has been widely recognized that the size, structure, shape and electronic states of the catalyst nanoparticles are the major factors which have a significant effects on the above discussed catalytic activity and its final performance [2,7–10]. Precious metals (e.g., Pt, Pd, and Rh) supported on oxide surfaces are the most widely used industrial catalyst materials. For these classes of catalysts, dispersion of the precious metal on the oxide support is an especially critical factor because of the expense of the metal. Furthermore, because of the severe condition of the catalyst application environment, the surface of catalyst could be adapted to a more stabilized geometrical structure to sustain under high temperature and pressure [60,61]. Therefore, the ability to understand and control the dispersion and morphology (typical characteristics that determine the performance of catalysts) of oxide-supported metal catalysts is a primary goal of catalyst design and can be enabled by understanding the nature of metal–support surface interactions.

For Pt NPs of similar size (0.8~1 nm diameter) but different geometric structure (shape), it was found that the different structure displayed distinct catalytic properties. In particular, a decreasing onset reaction temperature for 2-propanol oxidation was observed with increasing number of missing bonds at the NP surface[2]. In addition, oxidative catalytic activities of methanol and formic acid on various shape of Pt nanoparticles indicated a surface dependency on specific Pt facet. The specific activities of the Pt catalysts in methanol oxidation and formic acid oxidation follows Pt(111) > Pt(100) > Pt nanoparticle > Pt(poly) in the measurement [62]. In fact, the Pt(111) surface was found to be one of the most active surface for catalytic reaction. The isomerization of trans olefins to their cis counterparts is also found to be promoted by (111) facets of platinum [17]. Furthermore, to have an efficient nanoparticle in terms of mass activity, the particle size should be small as much as possible to provide a wide surface area. However, when the size of Pt nanoparticle is less than 1.8 nm, aggregation of Pt NPs takes place to reduce surface area which leads to a decreasing in its catalytic activity [62]. Meanwhile, all these parameters of catalyst NPs are interact with each other. It is shown that Pt NPs lattice dynamics and thermal behavior of NPs is affected by their geometric properties [63]. A significant shortening of the Pt-Pt bond lengths might lead a drastic increase in the Debye temperatures of Pt NPs that are synthesized by inverse micelle encapsulation and supported on γ -Al₂O₃ crystalline. However, heterogeneous catalysts are complex materials (nano-size with irregular shapes and structures) and it is difficult to achieve this goal due to the presence of various possibilities, active sites and the complexities of the catalytic systems.

2.4 MODEL SYSTEM STUDIES OF HETEROGENEOUS CATALYSIS

Model catalyst systems using metal particles, supported on well-ordered thin film oxide of appropriate thickness, allow investigations with the modern surface science methods to grasp essential aspects of the complexity of real catalysts systems. Valuable insights into the details of geometric and electronic structure, as well as adsorption and reaction properties could be obtained from the model catalyst systems. Studies using model systems, in particular single crystals, have shown that different surface planes can show widely different chemistries. The pioneering work of Ertl [10,64], who investigated a model catalyst system of Fe nanoparticles, revealed significant variations in nitrogen activation rate on different planes of the iron surfaces (an observation recognized by the Nobel Prize in Chemistry in 2007). An innovative study on the activity of Au particles support on TiO_2 , Figure 2.3, demonstrated that the Au catalytic activity is sensitive to their size and shape and that only particles in the range of 2 to 3 nm are active [65]. Previous studies on the model catalyst system of Rh on MgO by cross-section TEM, Figure 2.4, revealed an NP equilibrium shape with a cube-on-cube epitaxy where $\text{Rh}(100)||\text{MgO}(100)$ with a (100) surface becoming more prominent after carbon monoxide exposure at 600 K [19]. The examination of crystalline metal nanoparticles on single crystalline support has already been successfully applied to many catalyst systems, such as Au/TiO_2 , Ag/CeO_2 , Ag/MgO , Pd/TiO_2 , etc [11,19,59,65–70].

Former structural studies of the nanoparticle/support interface provide critical information on the surface morphology and interfacial energy. Previous investigators used the Wulff construction [71–73] to describe the observed nanoparticles shape and surface facets as well as determine the interfacial adhesion energies [74,75] (see APPENDIX I).

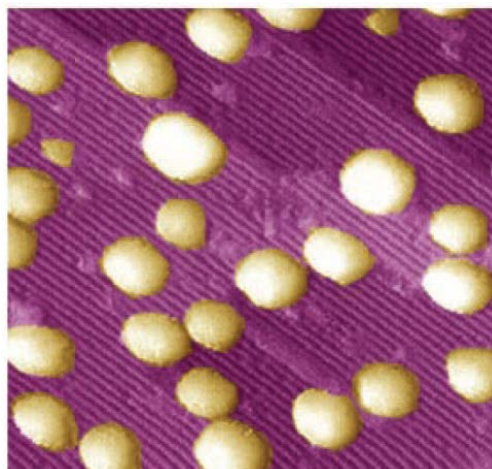


Figure 2.3 Au particle size and shape on the titania-support for CO oxidation, 30×30 nm [65].

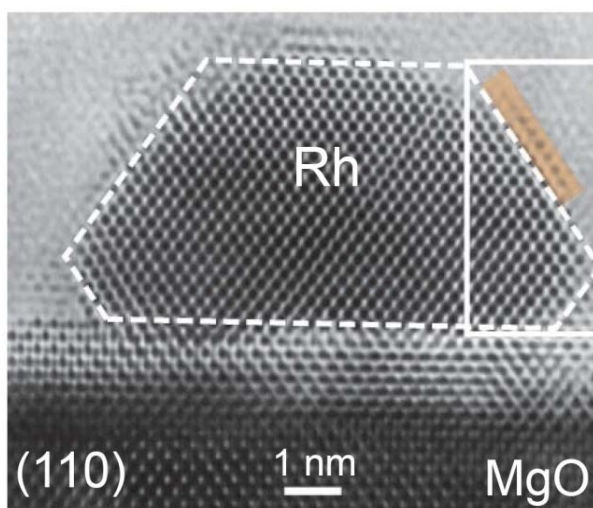


Figure 2.4 HRTEM micrograph of a Rh particle on MgO(001) in (110) view [5].

Meanwhile, model catalysts of Cu/ZnO were also prepared and characterized by in situ HRTEM under gaseous atmosphere [60]. The Cu nanoparticles' surface structure reversibly changed due to adsorbate-induced changes in surface energies and changes in the interfacial energy was observed, where the Wulff construction was used to estimate the interfacial energy. Figure 2.5

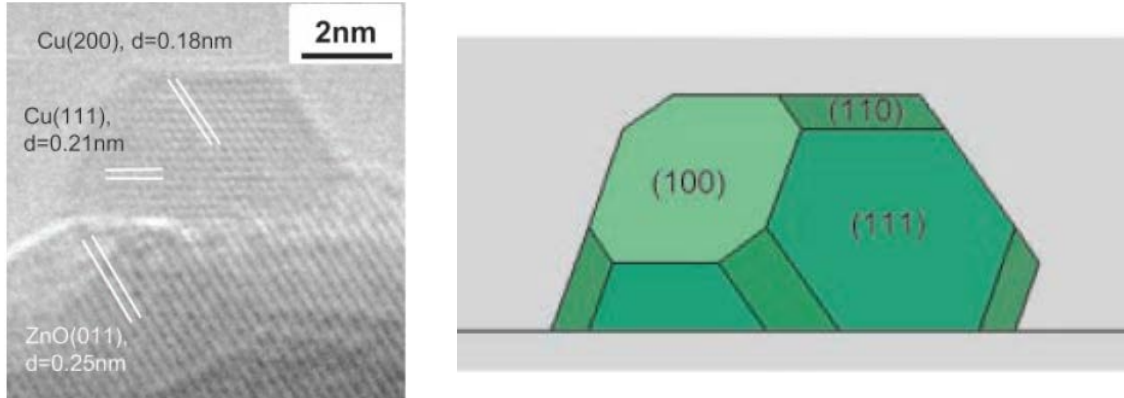


Figure 2.5 In situ TEM image of a Cu/ZnO catalyst exposed to 1.5 mbar of H₂ at 220 °C, (a). The electron beam is parallel to the [011] zone axis of the copper, (b). The corresponding Wulff constructions of the Cu nanocrystals [60].

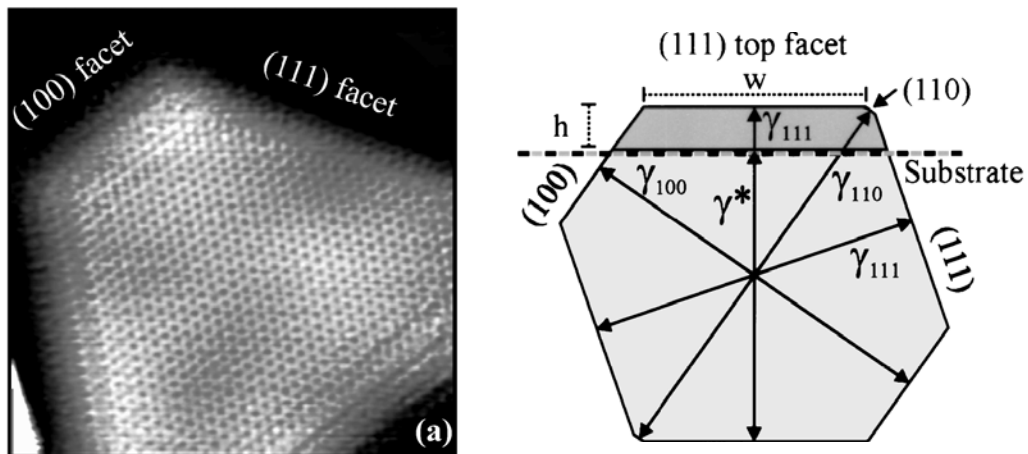


Figure 2.6 (a). Atomic-resolution images of crystalline nanosize Pd clusters. (b). Cross section of a Pd cluster based on the Wulff construction using theoretical surface energies for the three low-index Pd surfaces [74].

shows the Cu/ZnO catalyst model system with the corresponding Wulff-construction to calculate the interfacial energy. By applying the Wulff theorem, K. Højrup Hansen et al., studied the well-

ordered Pd clusters on $\gamma\text{-Al}_2\text{O}_3$ to obtain quantitative information on the work of adhesion (adhesion energy) of metal clusters deposited on oxides, $W_{\text{adh}} = 2.8 \pm 0.2 \text{ J/m}^2$. Figure 2.6 shows the Pd/ $\gamma\text{-Al}_2\text{O}_3$ scanning tunneling electron image with the corresponding Wulff-constructed shape. However, this result disagrees with values recently derived by the ab initio density-functional theory [74]. Thus, a more advanced model is needed to describe the equilibrium shape of NPs, such as the Wulff-Kaischew theorem (APPENDIX I).

In practice, heterogeneous catalysis nanoparticles must be supported, thus the support effects on the NPs shape adaptation need to be considered which is the limit of the Wulff construction for free standing particles. Considering that the catalyst support, especially $\gamma\text{-Al}_2\text{O}_3$ support, impacts the structural shape and the electron density around the catalytic nanoparticle which would modify the NPs shape, Kaischew's theorem [28,76,77] was taken into account to analyze the support effects to particle shape (see APPENDIX I). The present work suggests that the Kaischew theorem could be applicable to understand support Pt NPs' facets structure and will estimate the adhesion energy for the Pt/ $\gamma\text{-Al}_2\text{O}_3$ system. The benefits of the interfacial studies of the model nanoparticle/support heterogeneous catalyst could be classified into several categories:

- (1). To understand the support interactions to the morphology of metal particles, including shape, surface structure and decoration;
- (2). To determine the support effects on the thermal stability of the metal particles from studying the physical bonding between the catalyst and support at the interface;
- (3). To clarify the support effects on the electronic structure of the metal particles and around the metal particles sites, such as charging states and electronic defects;

(4). To determine the support effects on the catalytic properties of the metal particles with respect to specific shape, structure, size and electronic states, which is a consequence of the above considerations.

In the present study, a model catalyst system of Pt/ γ -Al₂O₃ will be prepared to investigate the particle/support interactions at the interface by using electron microscopy methods. To achieve this goal, the growth of single crystal γ -Al₂O₃ thin film on NiAl(110) surface was systematic investigated by oxidation method in dry ambient air. By formation and characterization of the model catalyst system, the γ -Al₂O₃ support interactions to the Pt catalyst equilibrium shape, structural epitaxy, thermal stability, electron states of the catalytic nanoparticle could be further elucidated to guide the catalyst design and development direction.

2.5 FORMATION OF SINGLE CRYSTAL γ -ALUMINA FILM

Typically, γ - Al_2O_3 is derived by thermal dehydration of aluminum hydroxide precursors. A well-known sequence of dehydration reactions starts from boehmite/amorphous $\text{Al}_2\text{O}_3 \rightarrow \gamma\text{-Al}_2\text{O}_3 \rightarrow \delta\text{-Al}_2\text{O}_3$ (tetragonal structure) $\rightarrow \theta\text{-Al}_2\text{O}_3$ (monoclinic structure) $\rightarrow \alpha\text{-Al}_2\text{O}_3$ (rhombohedral structure). $\gamma\text{-Al}_2\text{O}_3$ has been reported to appear at temperatures between 350°C and 1000 °C when it is formed from crystalline or amorphous precursors, and is stable at temperatures as high as 1200 °C when the $\alpha\text{-Al}_2\text{O}_3$ is used as the starting material [48]. When aluminum monohydrate or tri-hydrate is dehydrated by heating, the product first formed is amorphous. With continued heating at higher temperatures of about 500°C, a new crystalline phase begins to appear, which has been identified by its x-ray pattern and named $\gamma\text{-Al}_2\text{O}_3$. Continued heating at higher temperatures-above 1200°C results in its conversion into alpha-alumina. Conventional γ -alumina is typically prepared by thermal dehydration of coarse particles of well-defined boehmite at a temperature above 400–450°C. The oxide obtained usually presents a surface area and pore volume below $250 \text{ m}^2\text{g}^{-1}$ and $0.50 \text{ cm}^3\text{g}^{-1}$, respectively [15]. Also, its stability is greatly affected by steam, which accelerates the transformation of $\gamma\text{-Al}_2\text{O}_3$ into $\alpha\text{-Al}_2\text{O}_3$, with a consequent marked drop of surface area as a result of sintering. Besides thermal decomposition, several methods for $\gamma\text{-Al}_2\text{O}_3$ synthesis that use traditional techniques of preparative chemistry, such as precipitation and hydrolysis, have been developed to improve its textural properties and hydrothermal stability [78–80]. With this fabrication method, the commercial $\gamma\text{-Al}_2\text{O}_3$ is polycrystalline with irregular surface, as shown in Figure 2.2a.

Considering the technological and industrial importance of $\gamma\text{-Al}_2\text{O}_3$ single crystals, various research groups have initiated the preparation of single crystal $\gamma\text{-Al}_2\text{O}_3$ thin film

formations for the catalyst design and semiconductor applications. By using mixed-sources molecular-beam epitaxy (MBE), single crystal γ - Al_2O_3 films were reported to grow on Si (111) [81,82]. However, the deposited species consisted of Al_2O_3 molecules or clusters which will lead to poor crystallinity of γ - Al_2O_3 . MBE systems are expensive and sophisticated instruments.

An alternative way of producing γ - Al_2O_3 single crystals is by the oxidation of β -NiAl. β -NiAl intermetallic oxidation mechanisms have been extensively investigated because of its excellent oxidation resistance due to the formation of a slow growing α - Al_2O_3 layer at high temperatures as well as its ability to grow ultrathin γ - Al_2O_3 layers under extremely well controlled oxidation conditions [83,84]. Moreover, at temperatures below 1000 °C, the presence of metastable alumina, such as γ - Al_2O_3 that will later transform to θ - Al_2O_3 with increasing temperature, causes fast oxidation kinetics [84–86].

From oxidizing the NiAl intermetallic, surface scientists have reported Al_2O_3 layers formation on $\text{Ni}_3\text{Al}(111)$, $\text{NiAl}(100)$, and $\text{NiAl}(110)$ surfaces. Structural properties of such aluminum oxide layers strongly depend on surface orientation of the NiAl crystals [87]. By using the atomic-resolution scanning tunneling micrography (STM) method, N. Frey et al., have studied the initial stages of growth of alumina on a $\text{NiAl}(001)$ surface at 1025 K. An island by island growth of amorphous Al_2O_3 , and well-ordered θ - Al_2O_3 were found on the (100) surface, Figure 2.7a. The surface was completely covered by oxide strips which were equally oriented along the [100] and [010] directions at all coverage. Figure 2.7(b) shows the STM images characteristic of the increasing coverage of the surface by oxide strips. In addition, several Al_2O_3 phases have been reported by J. Doychak and co-workers during the oxidation of $\text{NiAl}(111)$. Between 1075 and 1375 K, δ - Al_2O_3 and θ - Al_2O_3 have been observed with θ - Al_2O_3 becoming the major phase with increasing oxidation time independent of the substrate orientation. γ - Al_2O_3 as

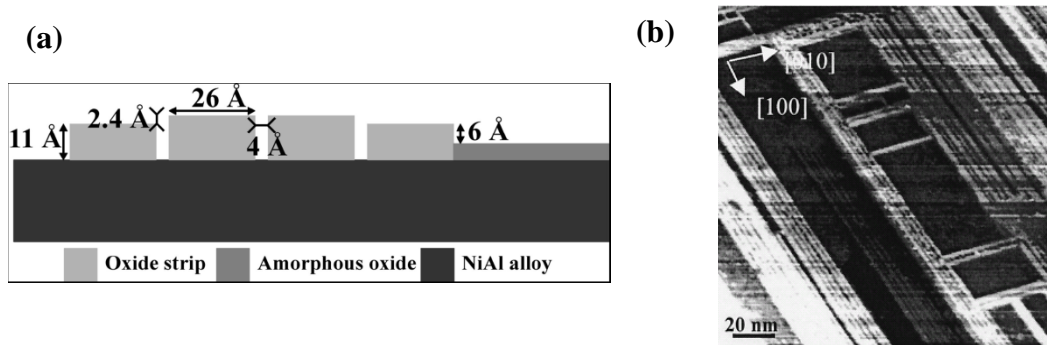


Figure 2.7 (a). The height measurements on an oxidized NiAl(001) surface. (b). STM images of the surface oxidized after 600 L of oxidation at 1025 K followed by 1 h of annealing [87].

the major formation specie, has been observed with δ - and θ - phases at the early stage oxidation of NiAl(111) [86]. In the case of NiAl(110), layer-by-layer growth mode of well-ordered alumina on NiAl(110) surface was observed during oxidation under well-controlled ultra-high vacuum (UHV) conditions [31,88]. By using low-energy electron diffraction (LEED) method, Jaeger et al, firstly reported a ~ 5 Å well-ordered epitaxial film Al_2O_3 layer grown on NiAl(110) surface by 1200 L oxygen introduction at 550 or 650 K, followed by heating without oxygen at 1200 K under UHV [89]. Later, the growth mode of this thin oxide was observed using the STM method, Figure 2.8 shows a large-scale scanning tunneling micrograph (STM) of the film. Detailed low-temperature STM images revealed that the morphology of the film is very smooth and the film spreads itself over the NiAl(110) surface (“carpet” phenomenon) which proved the layer-by-layer growth of this thin film. The different growth behavior of oxide formation on various NiAl surface could be due to the alteration of its surface energy caused the transition of growth model between that of layer by layer mode (higher surface energy NiAl (110)) to the island growth behavior (lower surface energy of NiAl (100) or (111)).

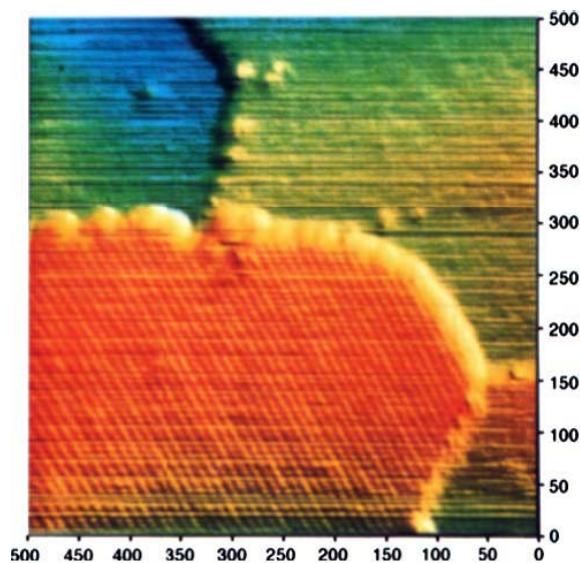


Figure 2.8 STM image of an early stage oxidized NiAl(110) surface(500Å×500Å) [90].

It is generally believed that such overlays have a γ -Al₂O₃ crystal and has then been extensively used to understand the γ -Al₂O₃ support effects in heterogeneous catalysis [20,91,92]. The choice of this system has several advantages. Through Al₂O₃ formation on the surface by oxidation, the free Ni dissolves in the NiAl bulk through heating because the thermodynamically most stable phase in the NiAl system is the nickel-rich Ni₃Al. The dissolution of nickel in the bulk can be monitored, for example, by electron spin resonance (ESR) spectroscopy [31,90].

However, a $\sim 5\text{\AA}$ thin film is less than one unit cell of γ -Al₂O₃ with a lattice constant of 7.9\AA , and may not maintain a periodical atomic structure as a crystal, thus it is still an open question whether it can be compared to bulk-like γ -Al₂O₃ used in heterogeneous catalysis or not. Despite an enormous effort, its structure has remained unresolved, impeding progress in a detailed understanding of the influence of the oxide support on the catalytic reactivity [43,93]. Recently, A. Stierle and G. Kresse revisited this thin Al₂O₃ oxide layer grown on a NiAl(110) surface respectively through a meticulously designed experiment with surface x-ray diffraction

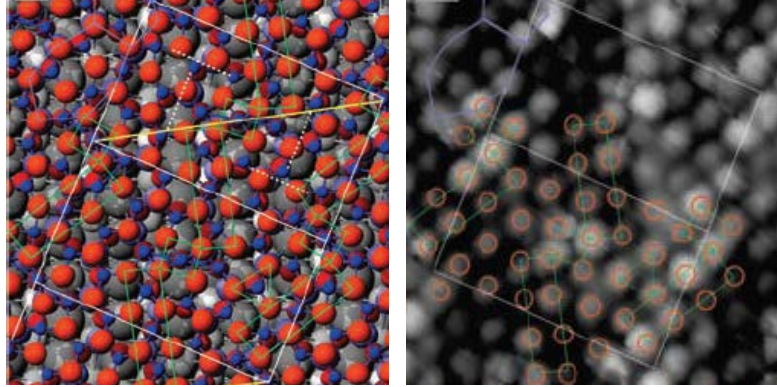


Figure 2.9 DFT (a) and STM (b) based model for the ultrathin aluminum oxide film on NiAl(110) [43].

(SXR), STM, and LEED as well as ab initio density functional theory (DFT) methods. Both investigators denied that the oxide layer persists as a native γ - Al_2O_3 structure. The ultrathin oxide film formed on NiAl(110) was reported to be a κ - Al_2O_3 -like film with orthorhombic crystalline structure, as determined by surface x-ray diffraction and theoretical simulation [93]. STM measurements (Figure 2.9b) observed square features on the surface (marked by green rectangles and squares) which could be explained as a square arrangement of oxygen atoms, as shown in the DFT model (Figure 2.9a). The stacking sequence and stoichiometry of the film is $4(\text{Al}_4\text{O}_6\text{Al}_6\text{O}_7)$ and thus deviates from the commonly assumed Al_2O_3 stoichiometry.

Although the well-ordered oxide film is not γ - Al_2O_3 at the initial stage oxidation, oxidation researchers have proved the metastable alumina phase appearance at some stage of oxidation by controlled temperature and time. Yang et al. and J. Doychak et al., reported γ - Al_2O_3 thin film formation on NiAl by oxidation in air at 950°C for 1 hour [86,94]. The transition of γ - $\text{Al}_2\text{O}_3 \rightarrow \theta$ - $\text{Al}_2\text{O}_3 \rightarrow \alpha$ - Al_2O_3 has also been systematically studied by H.J. Grabke and co-workers [84]. Meanwhile, one must consider any mixed oxides that are known to form. For instance,

NiAl₂O₄ is known to form at the NiAl/Al₂O₃ interface when oxidizing NiAl at 800°C [86]. γ -Al₂O₃ (7.908Å) and NiAl₂O₄ (8.048Å) are both favorable phases during oxidation with similar spinel structures since the Gibbs free energy of formation are both negative. Both were observed under similar oxidation exposure [86,94,95]. Besides, as a metastable alumina, γ -Al₂O₃ will later transform to θ -Al₂O₃ and then eventually to α -Al₂O₃ [85,94]. To control the oxidation process and sustain metastable phase growth without phase transformation or other favorable phase precipitation, is still a challenge for the fabrication of a thin film of γ -Al₂O₃ [86,96]. In addition, the high density of {110} and {111} growth twins would impede the γ -Al₂O₃ catalyst performance [86].

Hence, I plan to synthesize a well ordered epitaxial γ -Al₂O₃ film on the NiAl (110) alloy. The structural relation of the γ -Al₂O₃ scale with respect to the NiAl, as well as the thermal stability of the γ -Al₂O₃ and its growth kinetics on NiAl will be systematically studied as a function of temperature in order to determine the optimal growth conditions to form a flat single crystal γ -Al₂O₃ as a model catalyst support.

3.0 EXPERIMENTAL PROCEDURE

The details of the γ -Al₂O₃ thin film synthesis, TEM sample preparation and characterization are described in this chapter. The facilities used for this research include the Materials Micro-Characterization Laboratory at the Department of Mechanical Engineering and Materials Science, Nanoscale Fabrication and Characterization Facility (NFCF), at the University of Pittsburgh, and the Frederick Seitz Materials Research Laboratory at University of Illinois at Urbana-Champaign, Center for Functional Nanomaterials at Brookhaven National Laboratory, Carnegie Mellon University and Fischione Instruments, Inc.

3.1 PREPARATION OF THE PLATINUM/ γ -ALUMINA MODEL SYSTEM

3.1.1 Formation of the γ -Al₂O₃: NiAl(110) oxidation

Equiatomic single-crystal NiAl (110) (obtained from General Electric and fabricated by the Bridgman technique with typical C and O contents of ~6 ppm wt. each) was oriented to its (110) surface which was confirmed by texture X-ray diffraction (XRD). By using x-ray back reflection Laue diffraction method, single crystal NiAl was oriented to its (110) surface [89]. The surface orientation was checked by both Bragg–Brentano ($\theta/2\theta$) scan and texture x-ray diffraction (XRD), as shown in Figure 3.1. In the $\theta/2\theta$ scan, the diffraction peaks at 44.36° and 97.95° have

a narrow full width at half maximum (FWHM) and a sharp intensity which corresponds to the NiAl (110) and (220) planes and indicate a single crystallinity. Moreover, the crystallographic texture of the oxidized NiAl samples was characterized within a four-circle Philips X'pert X-ray diffractometer using the texture scan geometry. The texture XRD results also show the (110) surface plane orientation and single crystallinity. $5 \times 5 \times 1.5$ mm square pieces were cut from the bulk NiAl by electrical discharge machining. The specimens were polished up to 1200 grit and fine polished to $0.05\mu\text{m}$, as shown in Figure 3.2. Vibratory fine polishing (BUEHLER VibroMet® 2 Vibratory Polisher) was applied to all specimens in a $0.05 \mu\text{m}$ Al_2O_3 slurry to remove the surface scratches, Figure 3.2. The surface was then cleaned by plasma cleaner cycles with Oxygen mixed Ar gas (O:Ar ratio 1:4) in high vacuum to remove the surface contaminants.

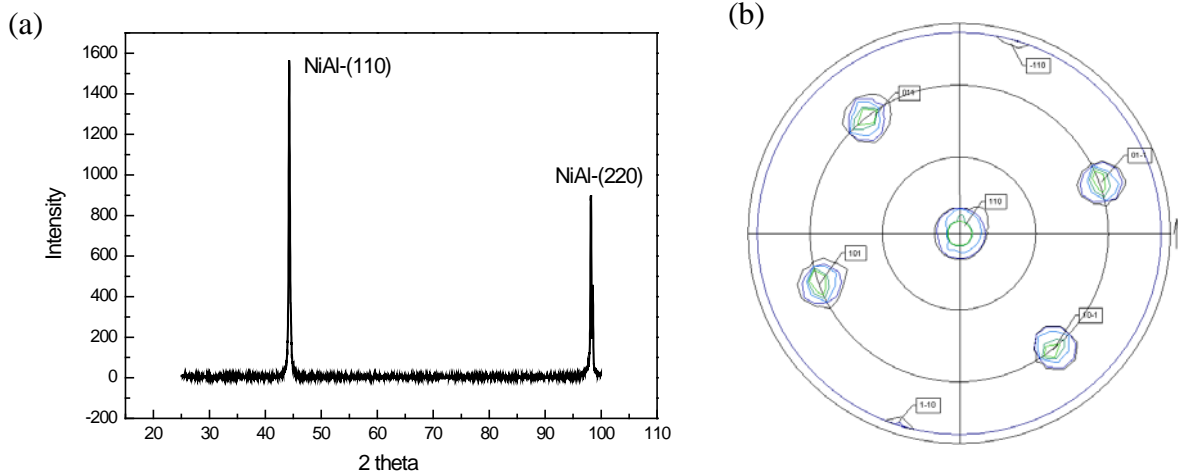


Figure 3.1 (a). Regular $\theta/2\theta$ XRD scan of as-prepared NiAl sample, (b). Texture XRD scan of the the bulk sample confirm NiAl(110) crystallinity and orientation.

Oxidation in dry air of the polished NiAl was conducted in a conventional tube furnace with an air flow rate of 0.2L/min for 2hrs at 650 or 750°C, or 1hr at 850 or 950°C. The

specimens were allowed to cool down to room temperature under Ar gas atmosphere and then slowly unloaded to avoid surface spallation of the oxide due to the abrupt temperature change.

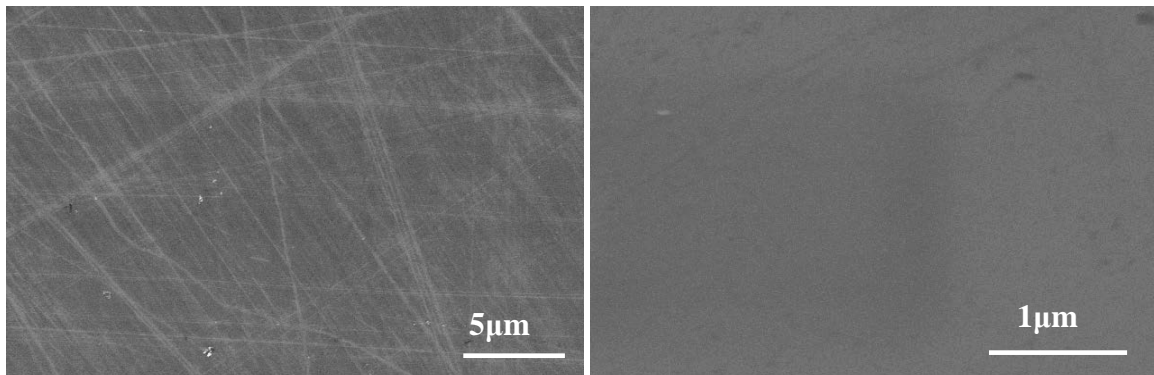


Figure 3.2 SEM images of the polished NiAl(110) surface, (a). Mechanical polish to 0.01 μm , (b). after vibration polishing.

3.1.2 Preparation of Pt nanoparticles supported on $\gamma\text{-Al}_2\text{O}_3$

A plasma cleaner was applied for 5 minutes with an oxygen to argon ratio equal to 1:4 to clean the oxidized sample surface. The sample was then placed into a Pascal dual e-gun UHV e-beam evaporator system, which has a base pressure of 6×10^{-9} torr.

To determine the optimal e-beam evaporation conditions for the deposition of Pt NPs in the appropriate size range and low dispersion appropriate for cross-sectional TEM imaging, various deposition parameters for Pt deposition onto ultra-thin carbon TEM support was explored. Ultra-thin TEM supports are easily obtained commercially, whereas single crystal NiAl is very costly and the preparation time for creating $\gamma\text{-Al}_2\text{O}_3$ thin film is significant (as described in section 3.2). Hence, deposition parameters were explored first using ultra-thin C

TEM grids to determine the optimal deposition conditions to form Pt NPs within the size range of 2-5 nm with reasonably low dispersion for cross-sectional TEM imaging and spectroscopy. Another advantage of using TEM grids is that the sample may be placed directly into the TEM to evaluate the size and dispersion of the NPs without any prior TEM sample preparation. Figure 3.3 and 3.5 are the HAADF STEM images of the Pt NPs and the size histogram for various deposition conditions. The optimal deposition condition was determined to be 2 Å/sec, substrate temperature of 500 °C, for 3 sec, as shown in Figure 3.3 where the mean size is 1.1 ± 0.2 nm.

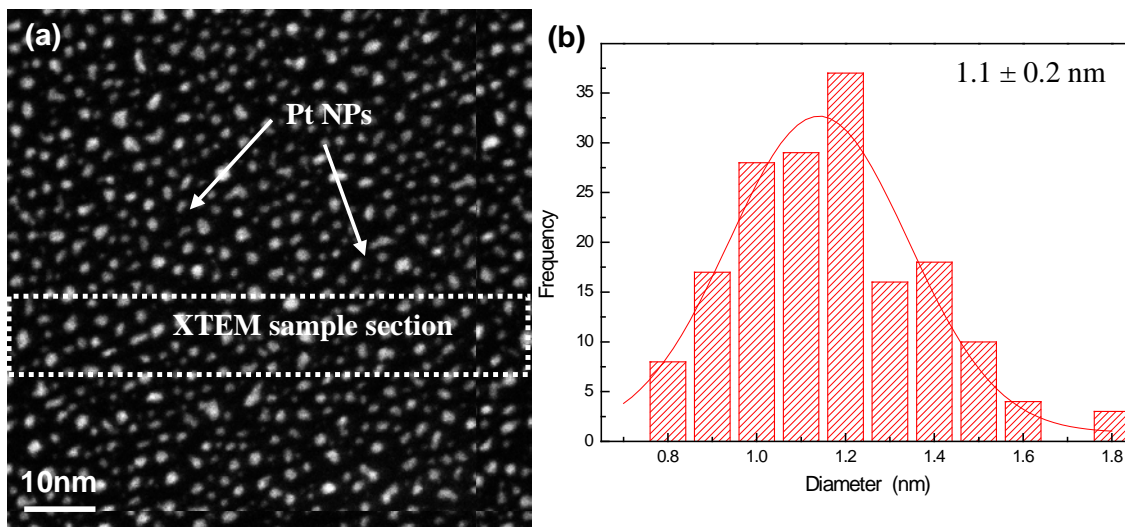
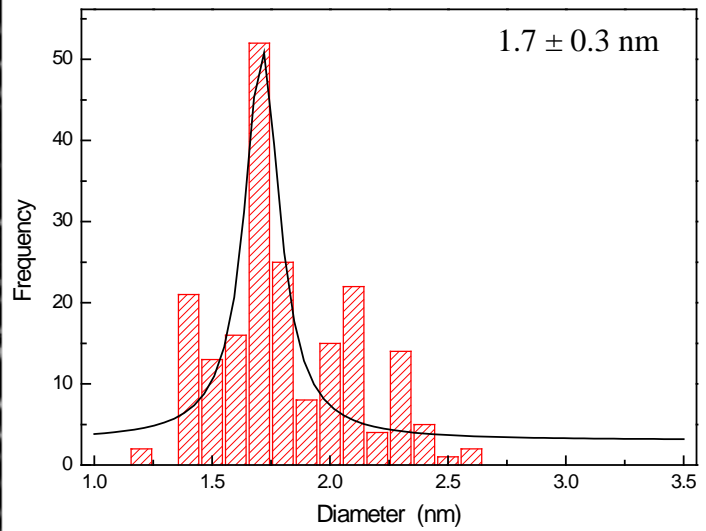
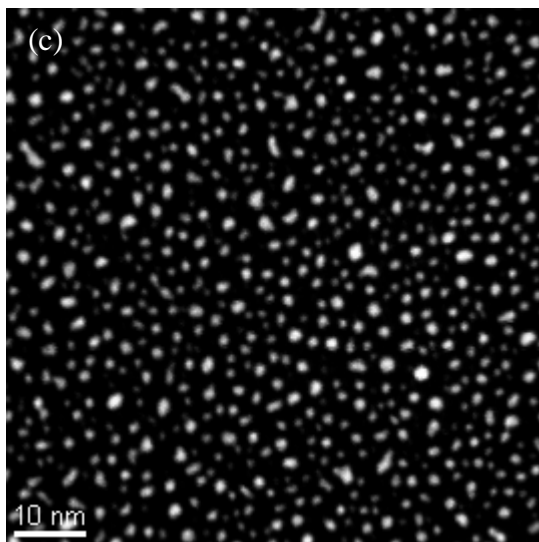
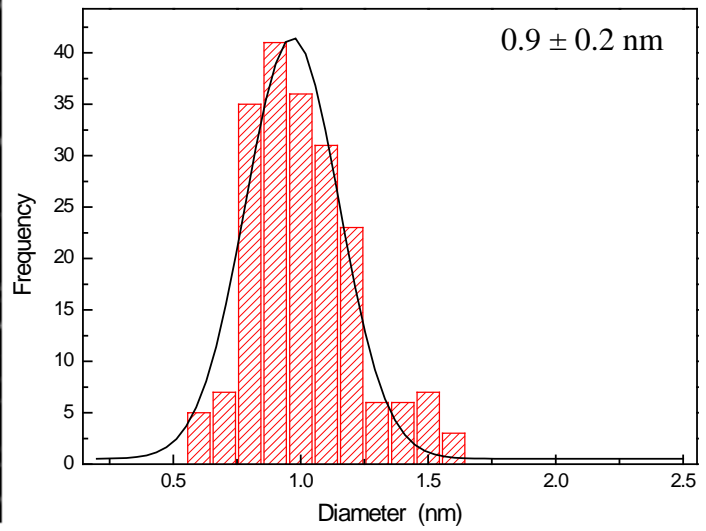
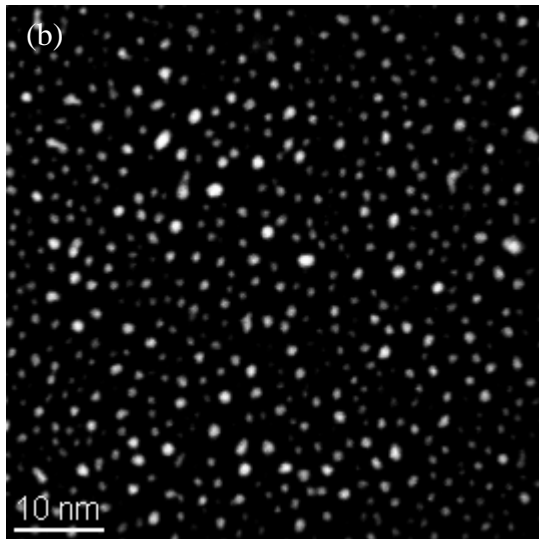
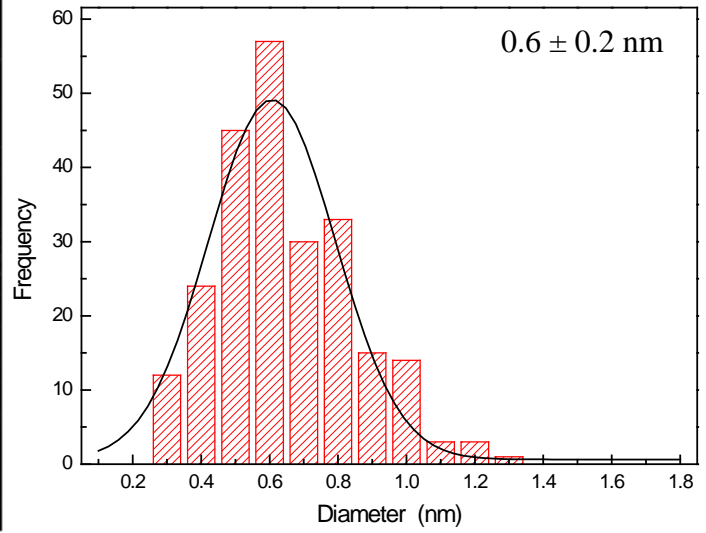
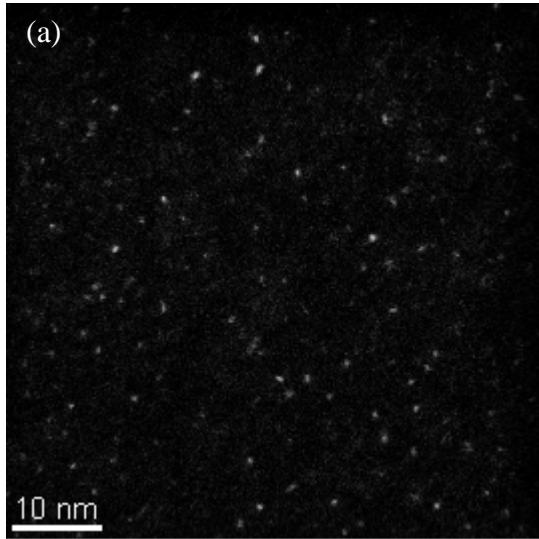


Figure 3.3 (a). HAADF image of Pt NPs on ultra-thin carbon film formed by electron beam evaporation of Pt at 2 Å/s at 500°C heating stage for 3 sec. (b). Corresponding size histogram of Pt NPs.



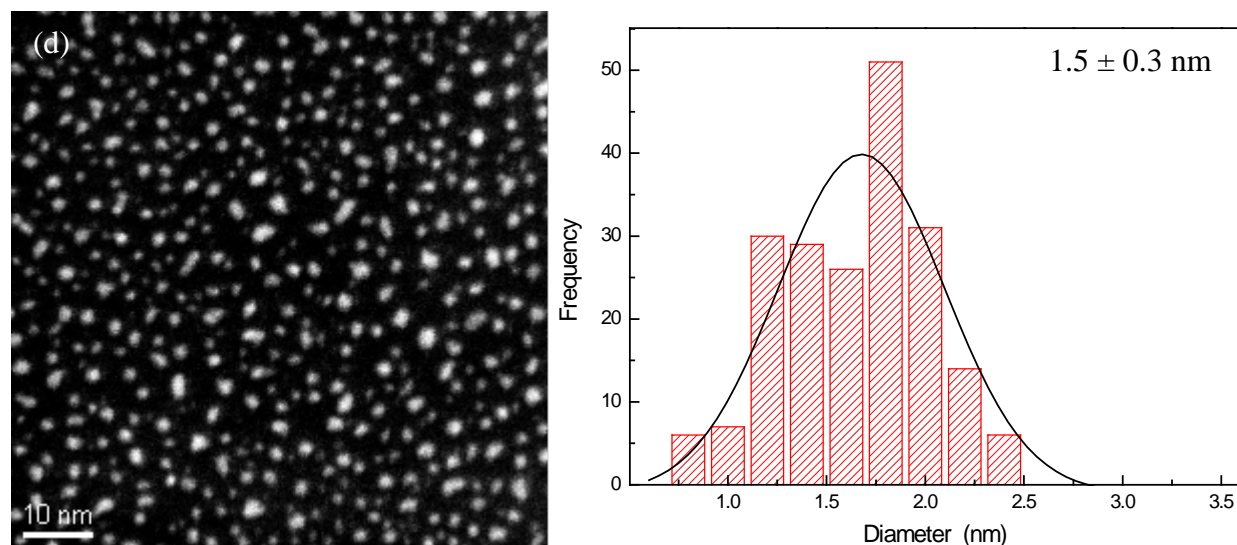


Figure 3.4 HAADF images and corresponding size distribution histogram of Pt NPs on ultra-thin carbon film deposited by electron beam evaporation at various parameters on heating stage, (a). 293K 0.1 Å/s for 0.1s, (b). 293K 0.1 Å/s for 30s, (c). 773K 2 Å/s for 3s, (d). 973K 2 Å/s for 4s

In order to enhance the Pt nanoparticles probability of becoming their equilibrium shape, a post annealing experiment of Pt on ultrathin carbon support was also conducted. The as-deposited Pt/C sample obtained from 700 °C at 2 Å/sec deposition rate was post annealed at 850 °C for 1h under ultrahigh vacuum chamber and characterized by HRTEM and STEM, Figure 3.5, where the selected condition, 850 °C and 1h, was the desired oxidation condition for single crystal γ -Al₂O₃ formation. The dominant particles size was still kept around 1.5 nm without evident size change. This could be due to the small diffusion coefficient of Pt atoms at 850 °C. Therefore, no further annealing treatment was applied to the prepared samples.

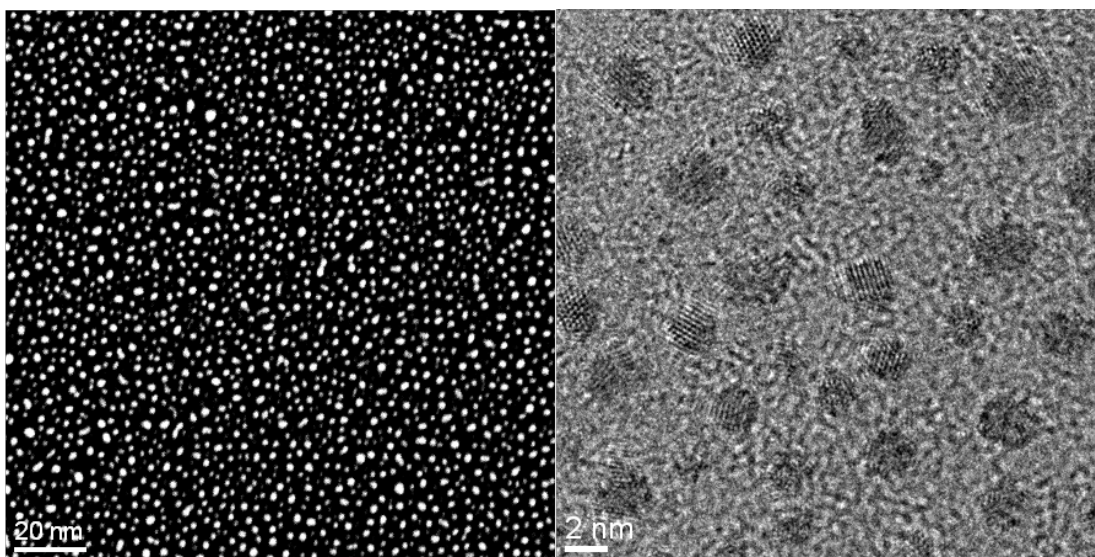


Figure 3.5 HAADF image and corresponding HRTEM image of Pt NPs on ultra-thin carbon film deposited by electron beam evaporation at 700 °C at 2 Å/sec and post annealed at 850 °C for 1h.

From this systematic study of deposition parameters and post-anneal onto ultra thin C TEM grids, the deposition condition of 2 Å/sec at $T = 500$ °C for 3 sec was selected as the Pt deposition condition to create the model Pt/ γ -Al₂O₃ system.

3.2 CROSS-SECTIONAL TEM SAMPLE PREPARATION

3.2.1 Dual-beam focused ion beam TEM sample preparation

Cross-sectional TEM samples were prepared by cutting a 50 nm thin NiAl/ γ -Al₂O₃ or NiAl/ γ -Al₂O₃/Pt NPs section using dual-beam focused ion beam (DB-FIB). A FEI-DB235 DBFIB at Frederick Seitz Materials Research Laboratory at the University of Illinois at Urbana-Champaign, a Seiko Instruments SMI3050SE FIB-SEM at the Nanoscale Fabrication and Characterization Facility (NFCF) at University of Pittsburgh or a FEI Nova at Carnegie Mellon University were used to prepare XTEM samples. A protective 300nm carbon film was sputtered on the sample surface by an AGAR carbon coater system to prevent FIB damage. Figure 3.6 highlights the cross-sectional TEM sample preparation procedure. After initial deposition of a 1 μ m Pt protective layer onto the sample top surface (Figure 3.6a), a XTEM sample was sliced out of the sample by Ga⁺ ion bulk milling (Figure 3.6b). The Omniprobe was used for the sample lift out (Figure 3.6e) and transfer to the Omnigrid (Figure 3.6f and g). A final DB-FIB thinning was performed to the sample to obtain a 150~50 nm thick cross-sectional TEM (Figure 3.6h and i).

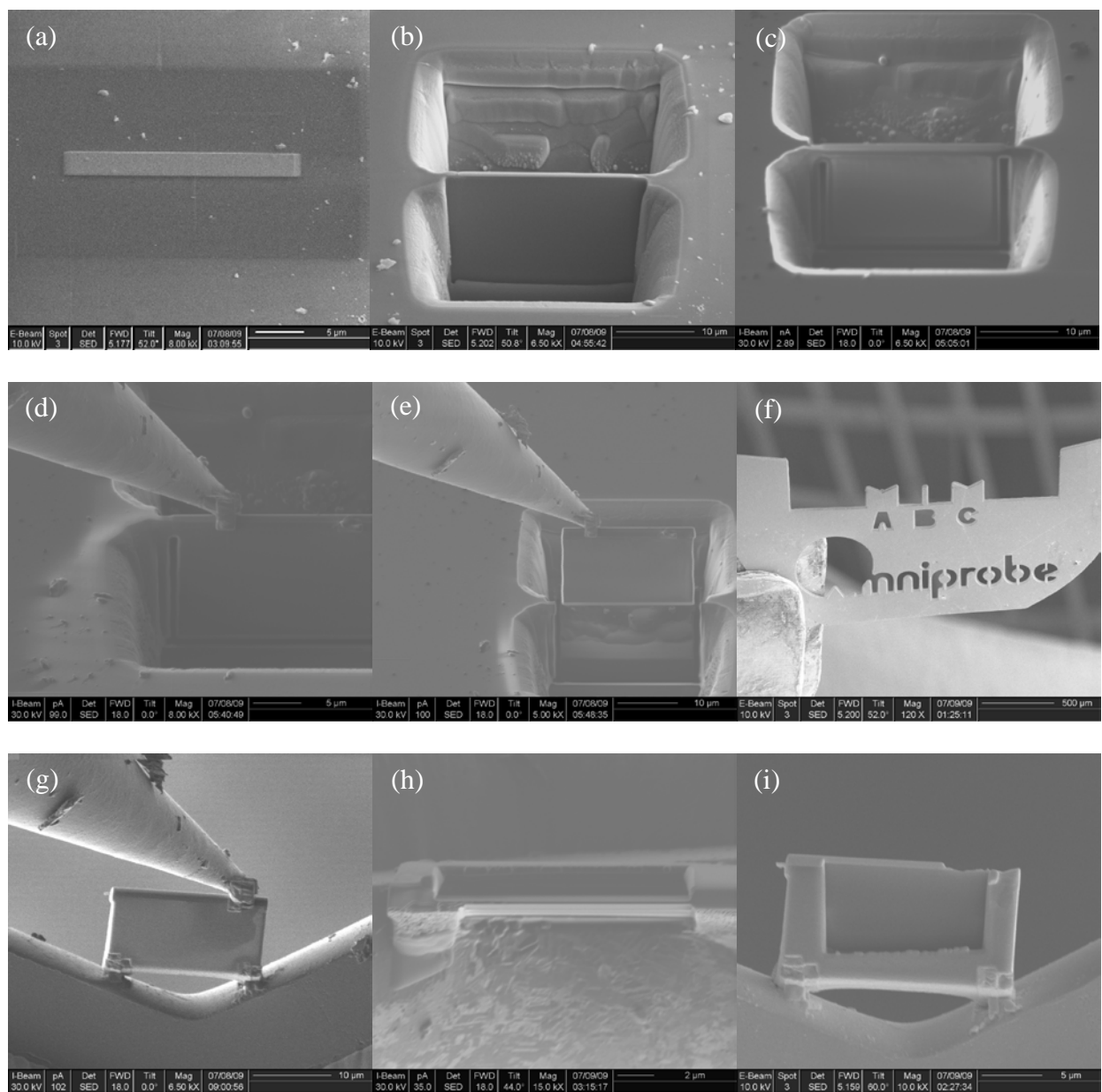


Figure 3.6 DB-FIB cross-sectional sample preparation procedure of the Pt NPs/ γ -Al₂O₃/NiAl system: (a). Protective layer deposition of platinum film, (b). Bulk Milling by Ga⁺ ions, (c). “U” cut (d). Omniprobe weld, (e). Sample lift out, (f). Transference to Omnigrid, (g). Sample welded to grid, (h). Further polishing at low 2 keV Ga⁺ ions, (i), Final thinned cross-sectional TEM sample.

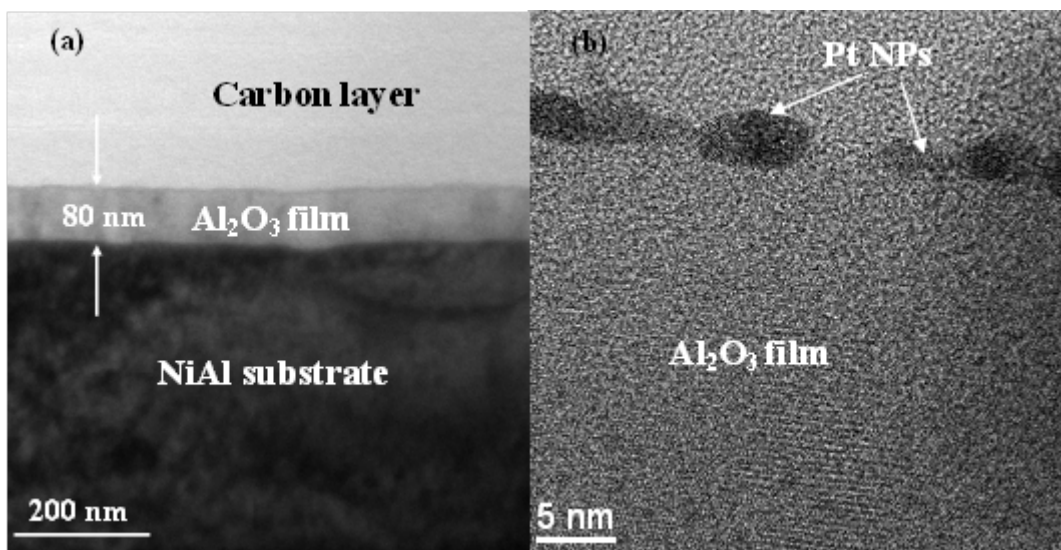


Figure 3.7 (a) BF TEM image of the Cross-sectional TEM sample of the NiAl/ γ -Al₂O₃ where the γ -Al₂O₃ was formed by NiAl(110) oxidized at 850°C for 1hr, (b) cross-sectional HRTEM image after Pt NPs are deposited onto the γ -Al₂O₃ showing ~3-5 nm dispersed on the oxide surface.

Figure 3.7 shows a XTEM bright field image of the NiAl/ γ -Al₂O₃ (Figure 3.7a) and γ -Al₂O₃/Pt interface (Figure 3.7b), where the XTEM samples were prepared in a Seiko DB-FIB at the NCF. However, the surface of the sample was damaged by the Ga⁺ ion during FIB milling. Further low energy ion-milling is needed to remove the damaged surface layer and improve the sample quality, especially for HRTEM and EELS analysis. The samples were further thinned with a low energy Ar⁺ ion beam at low angles (10° ~ 15°) using a Fischione Model 1040 NanomillTM. The thinning procedure was performed at E=900eV for 30 min per side, at then change to E=400eV for 15 min per side to obtain atomic resolution in HRTEM imaging, Figure 3.8. By comparing before and after nanomilled sample in Figure 3.7 and Figure 3.8, the damage of the γ -Al₂O₃ support has been removed significantly for improved HREM imaging.

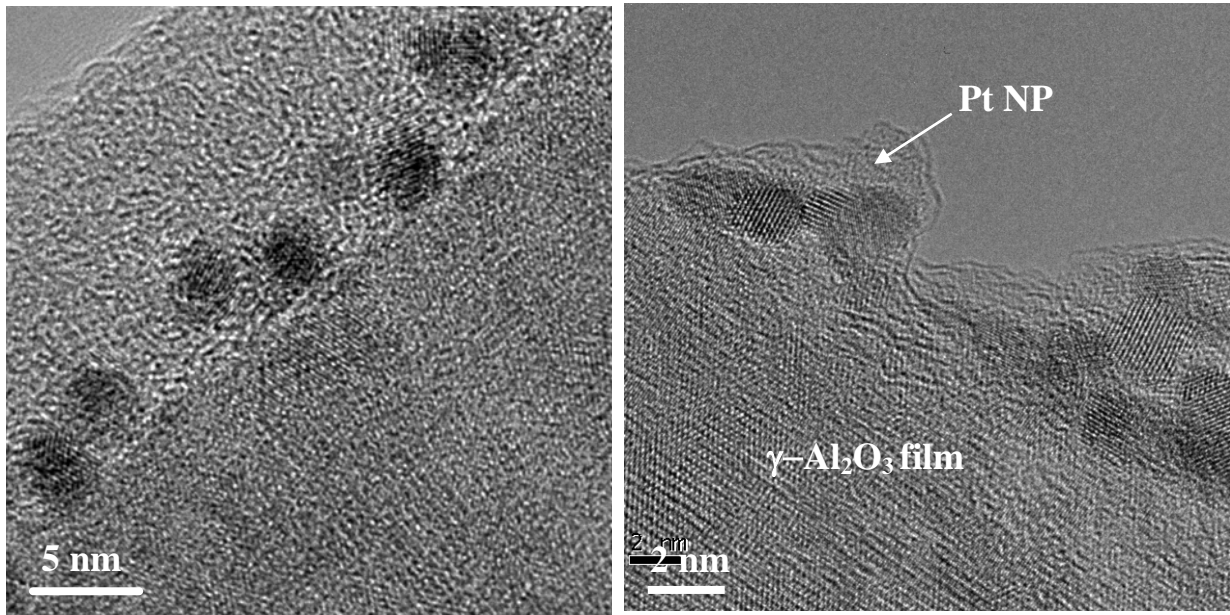


Figure 3.8 Cross-sectional TEM image of after nanomilled Pt/oxide interface.

3.2.2 Conventional TEM sample preparation

Since DB-FIB introduces much damage due to the Ga⁺ ions, conventional cross sectional TEM sample preparation method and tripod method were also tried on the Pt/ γ -Al₂O₃/NiAl sample. Other investigators have reported atomic level imaging and/or atomic-column spectroscopy using conventional TEM sample preparation [97], including nanoparticle/support interfaces [98], or with tripod polishing [99,100]. The sample was glued to a Si wafer with Gatan G1 glue to make a sandwich Si/ Pt/ γ -Al₂O₃/NiAl sample. The glue was cured under pressure at 120 °C for 12 h. Then, sandwiched specimen was cut in half parallel to the NiAl [100] zone axis, so that the desired epitaxial relation can be imaged during TEM characterization. The sample was put into a copper tube with an inner diameter of 2.3 mm to hold cross-sectional samples. The sample was

then sliced into several pieces with a thickness of 0.8 mm for polishing. Each side of sample was mechanically grinded in alumina lapping films with varying coarseness, from 3 μm down to 0.05 μm with a final sample thickness of 150 μm . Gatan dimple was used to reduce the center of specimens to 10 ~ 25 μm . Gatan Precision Ion Polishing System (PIPSTM) was applied for the final stage etching to obtain an electron transparent sample. A 10 mA, 5 keV of Ar^+ ions beam was used to remove sample materials by sputtering. The sector control on the ion mill was adjusted so that the ion beam was only incident when the Si wafer piece was normal to the beam direction in order to protect the glue line from faster etching. The sample was ion milled for both sides at the same time at an incident beam of 10 deg. The total milling time was around 1~2 h and stopped during milling to check the process of the thinned area. When a hole started to appear in the sample, a thin area around the hole will be electron transparent and a cross-sectional TEM sample could be obtained for view under TEM.

However, due to the high density of Pt NPs on top of the sample, the Gatan G1 glue could not be sustained during sample preparation indicating a weak Pt/ $\gamma\text{-Al}_2\text{O}_3$ interface. Future direction could be to produce larger Pt NPs with much lower dispersion so that the G1 glue contacts more with the $\gamma\text{-Al}_2\text{O}_3$ but the Pt NPs being larger will provide more Pt/ $\gamma\text{-Al}_2\text{O}_3$ interface for study. Thus, only a few of cross sectional TEM samples survived from the prolix procedure with continuous glue line as a protective layer. Due to the high failure rate of the conventional methods sample preparation, they were used in the current work.

3.3 CHARACTERIZATION METHODS

3.3.1 Surface morphology characterization by AFM and SEM

The surface topology and root mean square (RMS) surface roughness were measured by Veeco Manifold “Multimode V” scanning probe microscope (SPM) in tapping mode. The measurements were done on the as-prepared sample and the oxidized sample. In tapping mode AFM, a tip is attached to the end of a cantilever and scanned across the sample surface. The surface signal is acquired by the deflection of cantilever which is measured with the help of a laser and a split photodiode detector. A feedback loop maintains a constant deflection for each point on the surface by moving the cantilever vertically. The vertical movements of the scanner are recorded as a function of lateral position on the sample and a topographic image of the sample surface is formed.

In addition, the oxide surface morphology was also visualized within a Philips XL-30 field emission scanning electron microscope (SEM). The equipment includes secondary electrons, back-scattered electrons (BSE), and characteristic X-rays detectors. Secondary electron imaging shows the topography of surface features up to a few nm resolutions. Backscattered electron imaging could be applied to indicate the spatial distribution of elements or compounds within the top micron of the sample, and the topology of the specimen surface. The characteristic X-rays give information about the chemical composition of the material. The energy dispersive X-ray spectroscopy (EDS) enables the detection of chemical elements from Boron to Uranium in a qualitative and even quantitative manner.

3.3.2 High-resolution transmission electron microscopy (HRTEM)

Cross-sectional samples were characterized in a JEOL-2100F that resides in the NCF. The JEOL 2100F is an energy filtering, field-emission analytic TEM/STEM. The point-to-point resolution of the microscope is 0.24nm. Under HREM mode, the incident parallel electron beam interacts elastically while passing through the specimen, and the resulting modulations of its phase and amplitude are present in the electron wave leaving the specimen. Thus, the exit wave function contains the information about the object structure. To obtain lattice images, a large objective aperture has to be selected that allows many beams including the direct beam to pass. The image is formed by the interference of the diffracted beams with the direct beam by phase contrast. If the point resolution of the microscope is sufficiently high and a suitable crystalline sample oriented along a zone axis, then high resolution electron microscopy images could be obtained. In many cases, the atomic structure of a specimen can directly be investigated by HREM, including surface facets and atomic structure of heterogeneous catalysts and their changes when environmental TEM is used [61,101,102]

In amplitude contrast image, the angular distribution of scattered intensities varies as a function of the atomic composition and density of the object. Electron opaque object introduces substantial scattering with relatively large deflection. Therefore, many of the incident electrons on such objects are debarred at the lens aperture which makes the intensity of the images of these objects is relatively low. Conversely, electron transparent regions in the object, which are of lower average atomic number and/or thickness (mass density) produces little scattering beyond the lens aperture. The intensity of images of these objects will be correspondingly higher. Amplitude contrast can be controlled to some extent by a) changing of the acceleration voltage of electron and b) changing of objective aperture. Contrast could be enhanced at lower voltages

and with smaller apertures. However, unless the specimen is very thin, the higher chromatic aberration at lower accelerating voltages may lead to unacceptable loss of resolution. Gun brightness also decreases as the accelerating voltage is decreased.

In phase contrast image, contrast arises from differences in phase between scattered and unscattered rays in different parts of the image and interference between these rays. In a fully transparent (i.e. no variation in refractive index) object, there are no phase differences and, hence no phase contrast in the image. Defocusing, in which path lengths for scattered rays are changed more than for the unscattered rays, can be used to enhance phase contrast. Contrast due to phase differences is more important for thin objects and when working near the resolution limit than contrast due to amplitude differences.

Besides the HREM imaging, the JEOL 2100F is also able to perform high-angle annular dark-field (HAADF) STEM, nano-beam diffraction (NBD), and spatially resolved electron energy loss spectroscopy (EELS) as well as energy-dispersive X-ray spectroscopy (EDS) that operates at 200kV and uses a Schottkey field emitter for analytical studies purpose [103].

3.3.3 High angle annular dark-field (HAADF) STEM

High-angle annular dark-field STEM is using an focused electron beam (probe) scanning on the sample. Different interactions occur between the electron beam and the sample due to elastic scattering and inelastic scattering. It is understood that electron which are scattered by the sample through high angles (of the order of 50 mrad) contain information about the atomic number of the column being probed. Therefore, this HAADF signal is proportional to atomic number, Z [103].

However, the electromagnetic lens used in electron microscopes is not an ideal but has aberrations (astigmatism, spherical Cs and chromatic Cc aberration) that reduce image quality. Therefore, an aberration-corrected JEM-2200FS, that resides at UIUC, equipped with a CEOS probe Cs-corrector, and an in-column energy filter (Omega Filter) was applied for elemental analysis and imaging characterization. It allows elemental and chemical analysis of specimens with a small probe size of ~ 0.1 nm, thus atomic level high-angle annular dark-field (Z-contrast) images with corresponding EELS spectrum imaging can be obtained.

The chemical composition of specific samples can be analyzed inside of the TEM/STEM by using the electron dispersive X-ray (EDX) analysis in a STEM mode.

3.3.4 Electron energy loss spectroscopy (EELS)

When fast electrons enter a thin foil of a material, they interact with the constituent atoms via electrostatic forces and transfer energy to the material. As a result, inelastic scattering occurs between the incident electrons and the atomic electrons surrounding each nucleus. The excited states decay by emitting the transferred energy in the form of an X-ray, a visible photon, Auger electron, heat. Electron energy loss spectroscopy (EELS) probes the primary excitation and therefore recognizes the excitation event and its mechanism independently. Inelastic scattering is incoherent and involves a loss in the energy of the incident electrons. Some of the inelastic processes can be understood in terms of the excitation of a single atomic electron into a Bohr orbit of higher quantum number or a higher energy level. It is the energy analysis of the inelastically scattered electron beam that forms the basis for EELS. In general, the electron

energy loss spectroscopy can be considered as an absorption spectroscopy since energy and intensity from the incident electron beam is absorbed by the electronic interactions [104].

Three energy regions in energy loss spectra can be distinguished. Energy losses of a few meV to a few hundred meV are predominantly due to vibrational excitation (phonons), but unfortunately they can only be studied with energy resolution significant better than the typical EELS systems. Collective excitations (plasmons), intraband and interband transitions cause energy losses between a few eV and about 40eV. An energy loss above around 40eV, one finds the inner shell excitations. These occur at energies, $\Delta E \geq E_f - E_b$, where ΔE is the energy loss, E_f is the Fermi level energy, and E_b is the binding energy of the inner shell. The corresponding feature in an energy spectrum is an inner shell loss edge, whose threshold energy usually agrees to within few eV with the known ionization energy for the appropriate electron shell of the atom. Electron energy loss spectroscopy of inner shell losses therefore provides a standard method of identifying atoms of different types in the thin foil of a material. The various inner shell edges that can arise are then identified following standard spectroscopic notation.

The analysis of experimental EELS data is usually based on the comparison of the observed spectrum to data from a set of reference materials and yields information only through changes relative to such a standard. Here we focus on measuring the electronic states that directly determine the electrical properties of the interface, which we do with atomic-scale EELS. EELS line scan was also employed to study the unoccupied electronic density of states site by site. These measurements give localized information about both chemical composition and electronic properties [105–108].

4.0 γ -ALUMINA THIN FILM FORMATION VIA OXIDATION

In this chapter, β -NiAl(110) was oxidized in dry air to form a γ -Al₂O₃ single crystal layer which could ultimately serve for model catalyst support studies. The oxide structure, epitaxy, growth kinetics and mechanism for γ -Al₂O₃ formation were studied by XRD, AFM, SEM, cross-sectional TEM and STEM methods at the oxide surface and the metal/oxide interface analysis.

4.1 EXPERIMENTAL RESULTS

4.1.1 Macroscopic structure and morphology of γ -Al₂O₃(111) formation on NiAl(110)

β -NiAl(110) was oxidized in air for 1 to 2 hours within the temperature range 650-950°C, and the structure and morphology of the oxide films were characterized by a cross-sectional transmission electron microscopy (TEM) method. Figure 4.1 shows the $\theta/2\theta$ XRD scans for NiAl(110) oxidized in air for 1 hour at 850 and 950°C and for 2 hours at 650 and 750°C. At 650°C, no peaks besides the NiAl(110) peak were noted in the $\theta/2\theta$ scan. As for the $T \geq 750^\circ\text{C}$, a small peak at 39.5° was detected by XRD fine scan using a longer collection time which is close to γ -Al₂O₃(222), $2\theta = 39.52^\circ$. Moreover, a probable γ -Al₂O₃(444) peak was seen from the scale formed after 1h at 950°C. Although other transition alumina phases could not be ruled out due to

their similar d-spacing to the (222) γ - Al_2O_3 , the peak presence at (222) position with the absence of other peaks suggests epitaxial γ - Al_2O_3 (111) film growth on the NiAl (110) surface. The low X-ray intensities indicate that the oxide films are ultrathin. A better understanding of the oxide growth kinetics was conducted to better interpret the resulting thickness and formation behavior of the thermally grown films (APPENDIX II).

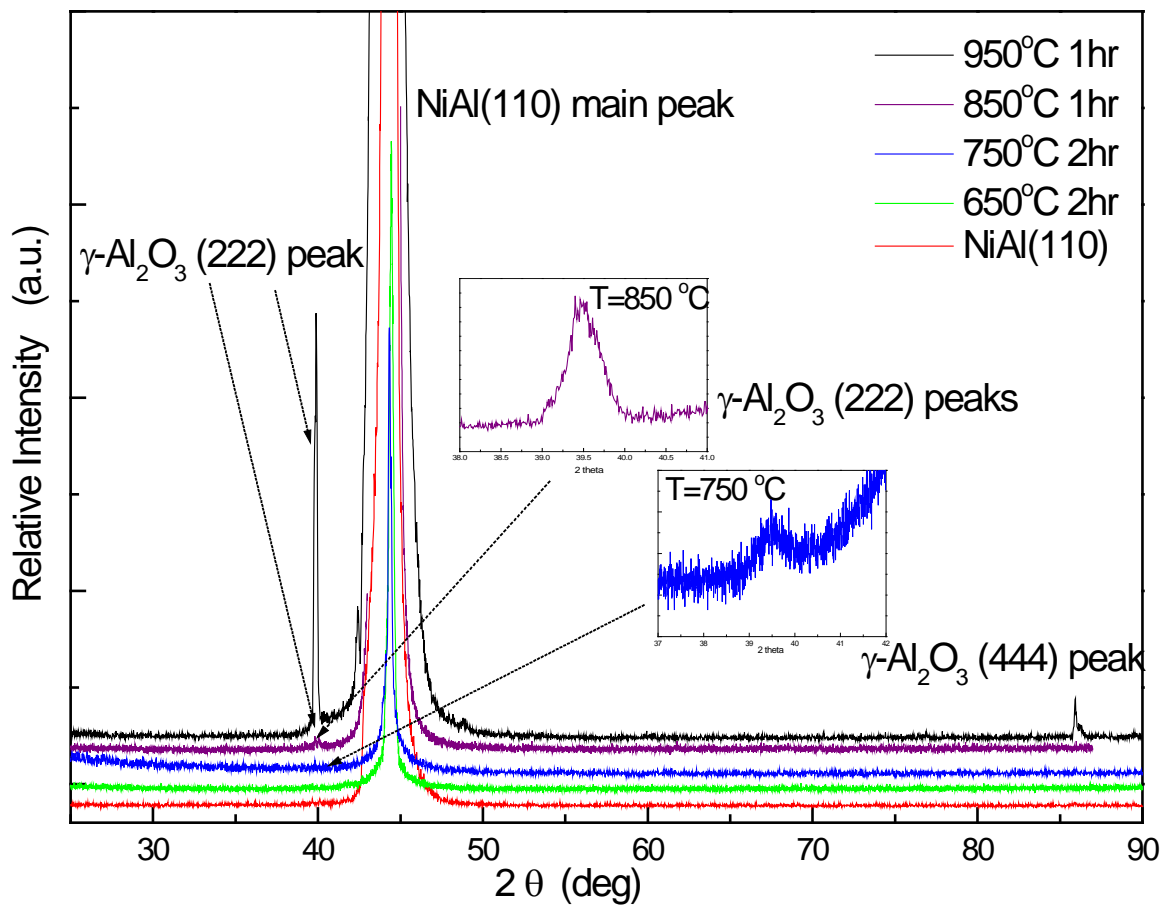


Figure 4.1 $\theta/2\theta$ XRD scans for NiAl(110) specimens oxidized at different temperatures for 1 or 2 hrs: γ - Al_2O_3 (222) and (444) peaks were observed; fine scan from 37 to 42 deg was applied to 750°C 2hrs sample which also showed a γ - Al_2O_3 (222) peak at 39.5 deg.

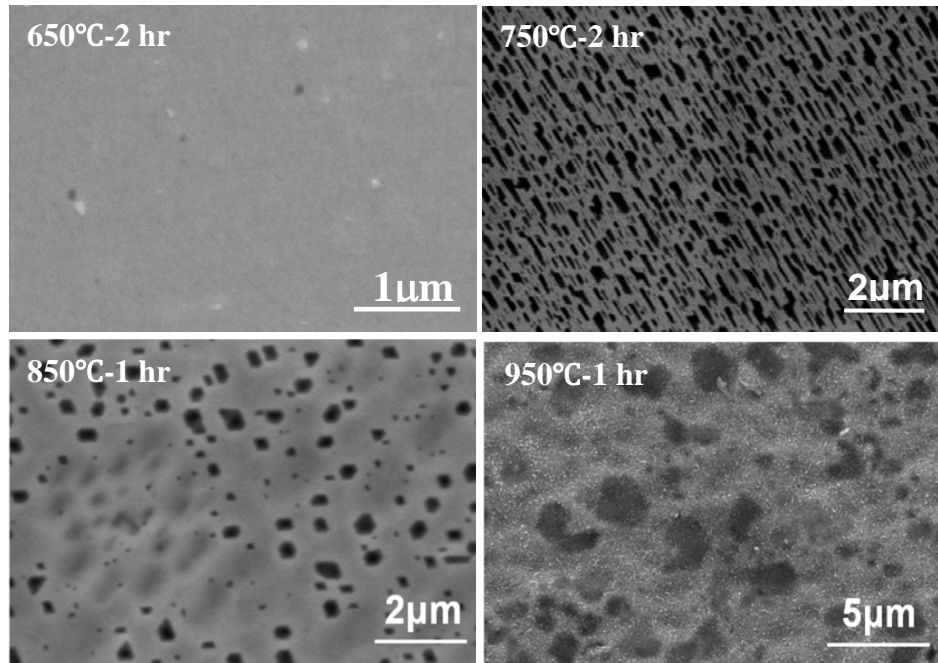
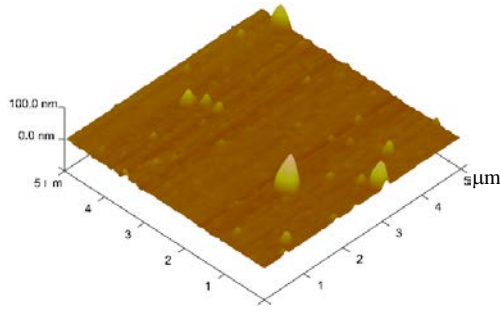
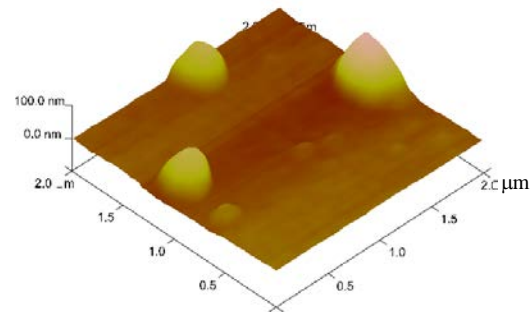


Figure 4.2 SEM images of oxidized NiAl(110) surface at various oxidation conditions in dry air

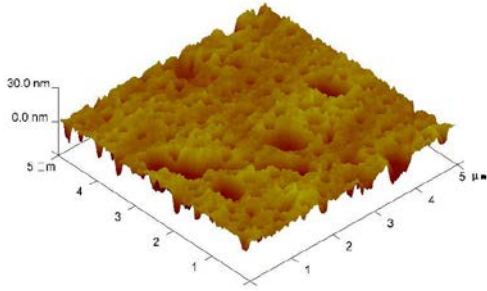
SEM images shown in Figure 4.2 indicate a continuous and flat alumina film produced at 650°C. With increasing reaction temperature to 750 and 850°C, the surfaces became increasingly rumpled. The dark contrast observed at 750 °C for 2h oxidation was due to a large portion of kirkendall voids in the alloy subsurface, beneath the γ -Al₂O₃ thin film, formed due to vacancy condensation associated with the γ -Al₂O₃ growth being predominated by Al³⁺ diffusion. A plate-like morphology formed after oxidation at 950°C where some spalled oxide areas were also observed. The surface roughness was characterized by atomic force microscopy (AFM), as shown in Figure 4.3. Below 750°C, the oxidized surfaces developed uniformly. AFM images showed needle-like nano-rods that appeared during the 550°C oxidation with a root mean square (RMS) surface roughness around 1.8nm. At higher temperatures, more nucleation sites led to dense and rough nodular features. The RMS surface roughness increased from 1~2 nm below 650°C to 8nm at 850°C. The morphology gradually changed from a fine flat surface with



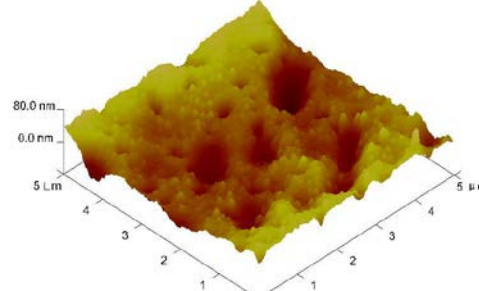
550 °C 1 hr RMS roughness 1.4nm



650 °C 2 hr RMS roughness 1.5nm



750 °C 2 hrs RMS roughness 3.1 nm



850 °C 1 hr RMS roughness 10.3nm

Figure 4.3 AFM images of oxides surface morphology under different oxidation conditions

Table 4.1 γ -Al₂O₃ thin film parameters and orientation relation at various oxidation conditions, the error bars denote the standard deviation.

T (°C)	t (hr)	Thickness (nm)	RMS of Surface Roughness (nm)	<i>l</i>	NiAl/ γ -Al ₂ O ₃ O.R.
650	2	13.77 ± 0.10	1.5	(3.71 ± 0.01) <i>l</i> ₀	KS
750	2	46.08 ± 1.85	3.1	(6.79 ± 0.13) <i>l</i> ₀	KS + twin defects
850	1	78.41 ± 1.03	10.3	(8.85 ± 0.06) <i>l</i> ₀	NW
950	1	271.65 ± 18.35	36.5	—	Textured Polycrystalline

submicron nodular features to widespread coarse whiskers with a rough morphology. To obtain a flat surface, nucleation sites should be controlled at a relatively low ratio. At low temperatures, the oxidation surface was smooth and even, however, needle-like grains scarcely had already formed on the sample surface and grew larger with time. Continuous alumina films were obtained at 650°C with flat morphology. Attaining uniform morphology features is crucial for model catalyst support application. The surface roughness was measured with AFM; the RMS surface roughness ranged from 1.5 to 36 nm with increasing oxidation temperature. The oxide thickness, surface roughness, epitaxial relationship and oxide morphology as a function of the oxidation conditions are summarized in Table 4.1.

4.1.2 Analytical electron microscopy analysis of γ -Al₂O₃ film structure and epitaxy

TEM was used to confirm and characterize the oxide scale that formed on the NiAl(110) surface after oxidation at 850°C. Analytical TEM is necessary to clearly distinguish the spinel structure of γ -Al₂O₃ ($a_o = 0.7908$ nm) from the spinel structure of NiAl₂O₄ ($a_o = 0.8048$ nm) [86]. Conventional TEM and high-resolution TEM (HRTEM) characterization were carried out with a JEOL JEM 2000FX and JEM 2100FEG, respectively.

Figure 4.4 ~ 4.7 are the cross-sectional TEM results from the NiAl/ γ -Al₂O₃ interface formed by oxidation at $T = 850^\circ\text{C}$. Figure 4.4a is a bright-field TEM image showing a uniform and continuous 80nm oxide film. The HRTEM image of the oxide film (Figure 4.4b) and its Fast Fourier transforms (FFT) (Figure 4.4b inset) confirms the spinel structure of γ -Al₂O₃, as projected along γ -Al₂O₃ [211]. The γ -Al₂O₃ (222) interplanar spacing is 2.28Å which matches remarkably with the γ -Al₂O₃ data from powder diffraction file (PDF, 100425, 2.280Å).

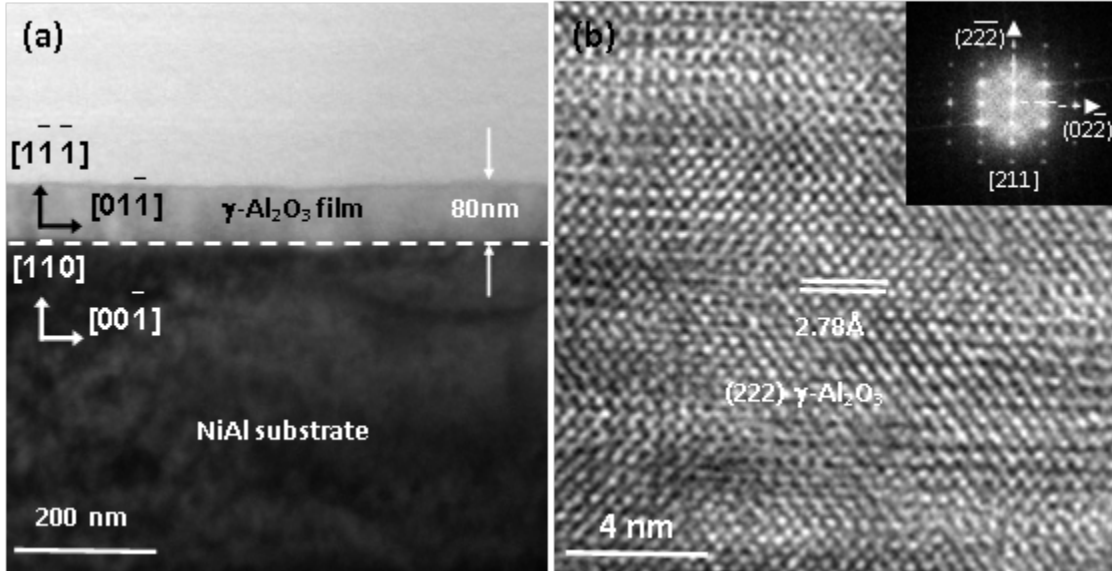


Figure 4.4 Cross-sectional TEM images of the $\gamma\text{-Al}_2\text{O}_3$ film by NiAl oxidation at 850°C 1hr. (a). Continuous oxide film formed on NiAl surface projected along NiAl[110] || $\gamma\text{-Al}_2\text{O}_3$ [211]. (b). Oxide film HRTEM image conserve $\gamma\text{-Al}_2\text{O}_3$ lattice structure with Fast Fourier transformation (FFT).

In order to obtain direct information on the crystallinity of the oxide thin film, nano-beam electron diffraction pattern (NB-EDP) was employed with a 20nm beam. Both HRTEM (Figure 4.5a) and NB-EDP (Figure 4.5b) revealed single crystal $\gamma\text{-Al}_2\text{O}_3$ thin film formation without planar defects, e.g., {111} twins. Since several metastable oxide phases exist with similar crystal structures, though different crystal symmetries, it is important to confirm that the oxide phase is the spinel crystal structure corresponding to $\gamma\text{-Al}_2\text{O}_3$. The NB-EDP from the oxide film prepared at 850°C and 1 hr showed a 2mm symmetry, thus, the monoclinic $\theta\text{-Al}_2\text{O}_3$ was ruled out; since twins were not observed, then the 2mm symmetry cannot be from a twinned $\theta\text{-Al}_2\text{O}_3$. $\delta\text{-Al}_2\text{O}_3$ is

orthorhombic with triple the lattice spacing of $\gamma\text{-Al}_2\text{O}_3$ along the c axis; hence, the absence of superlattice spots from the EDP demonstrate that the oxide is not $\delta\text{-Al}_2\text{O}_3$ [109]. $\eta\text{-Al}_2\text{O}_3$ and $\gamma\text{-Al}_2\text{O}_3$ are both spinel structures, but the measured lattice constant 7.90\AA is more consistent to the $\gamma\text{-Al}_2\text{O}_3$ powder diffraction file (PDF, 100425) than $\eta\text{-Al}_2\text{O}_3$ ($a_o = 7.98\text{\AA}$) [110]. Hence, the oxide is concluded to be single crystal $\gamma\text{-Al}_2\text{O}_3$.

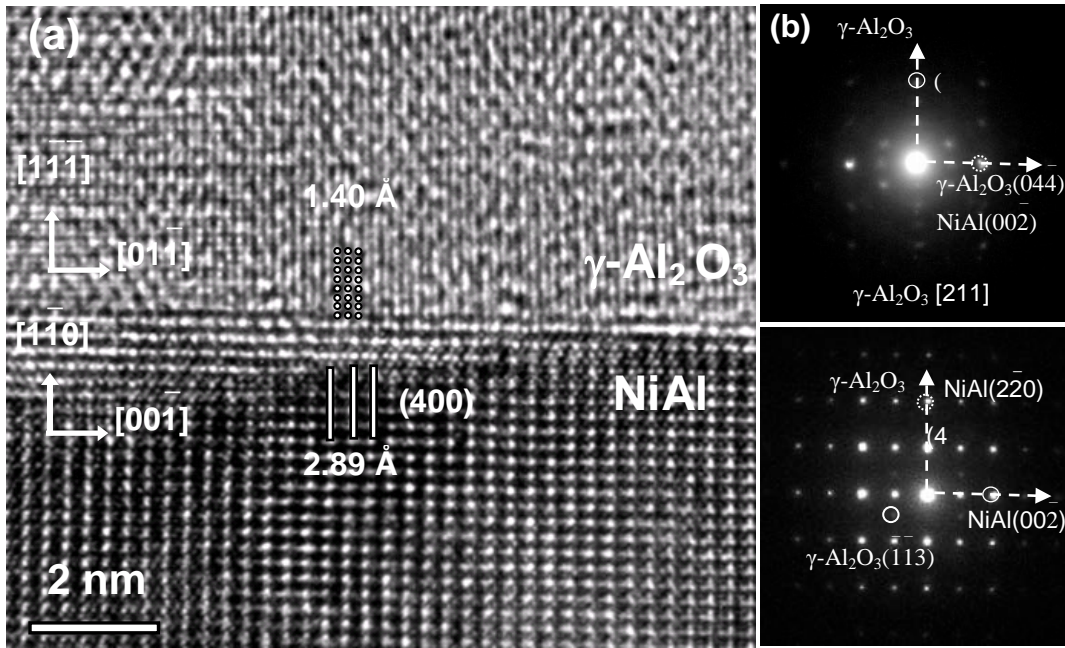


Figure 4.5 Cross-sectional HRTEM image of 850°C 1hr oxidized NiAl/ $\gamma\text{-Al}_2\text{O}_3$ interface: (a). Interface of (111) $\gamma\text{-Al}_2\text{O}_3$ film on (110)NiAl. (b). NB-EDP from upper $\gamma\text{-Al}_2\text{O}_3$ film, (c). SAD from NiAl/ $\gamma\text{-Al}_2\text{O}_3$ interface.

The selected area diffraction pattern (SAD) (Figure 4.5c) and the HRTEM image (Figure 4.5a) at the interface confirmed the relative O.R.: NiAl($\bar{1}\bar{1}0$)[110] $\parallel\gamma\text{-Al}_2\text{O}_3$ ($\bar{1}\bar{1}\bar{1}$)[211] along the zone axis and NiAl($\bar{1}\bar{1}0$)[001] $\parallel\gamma\text{-Al}_2\text{O}_3$ ($\bar{1}\bar{1}\bar{1}$) [011] along the interface. A schematic diffraction pattern of this O.R. is shown in Figure 4.6, which represents a cross-sectional view of the

NiAl[110]|| γ -Al₂O₃ [211] where the diffraction patterns were overlapped with each other. A good match can be seen between the SAD from NiAl/ γ -Al₂O₃ interface (Figure 4.5c) and simulated diffraction pattern (Figure 4.6).

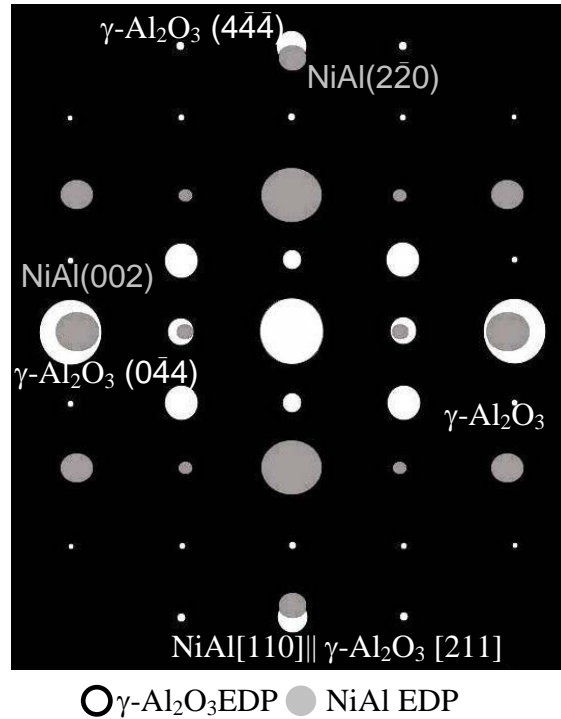


Figure 4.6 Schematic diffraction pattern of superimposed NiAl[110]|| γ -Al₂O₃ [211]

The elemental composition across the metal/oxide interface was probed by EELS on a Cs-corrected JEOL JEM 2200FS S/TEM (probe corrected with resolution better than 0.1nm). Energy dispersive spectroscopy (EDS) was also performed by Hitachi HD-2300 FESEM/STEM with point resolution of 0.2nm, to analyze the Ni and Al composition change across the NiAl/ γ -Al₂O₃ interfacial region. Figure 4.7 shows a high-angle annular dark field (HAADF) image and EELS mapping obtained with the Cs-corrected JEM 2200CF S/TEM (0.1 nm probe with probe-

corrected STEM) with an in-column Omega Filter. The O-K edge and Ni-L edge maps were taken across the NiAl/ γ -Al₂O₃ interface, and EELS analysis combined with the atomic resolution HAADF image indicated an abrupt interface. Z-contrast imaging directly exhibited uniform contrast in the NiAl substrate at the atomic level indicating no elemental segregation (i.e. below the limit of detection, which is 0.01 at. %). The signal intensity variation is attributed to the contribution of electrons at the given energy level, which can be affected by the collective excitations variation due to sample thickness, interfacial elemental distribution and strain field at the interface. Continuous and full colored maps were constructed to illustrate the intensity distribution/fluctuation in the corresponding region. The intensity code, green to blue, relates to no signal of elements or signal background noise. While the intensity of red to white represents detectable signal of corresponding element. No NiAl₂O₄ or NiO was found in the vicinity of the interface by EELS or HRTEM analysis. The signal intensity variation could be directly observed from the EELS line scan spectra across the interface. To better understand the interfacial atomic bonding, 20 EELS line spectra were collected with a 0.1 nm probe size in the 10nm EELS line scans conducted across the metal/oxide interface in several areas, Figure 4.8 and Figure 4.9.

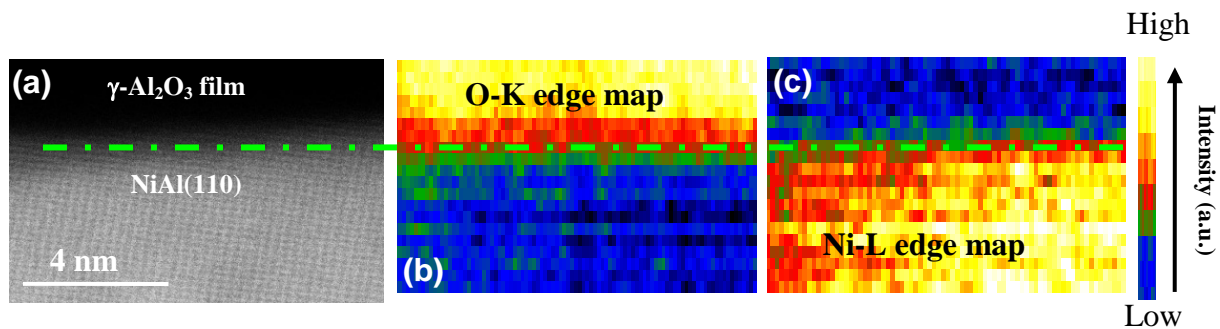


Figure 4.7 HAADF image (a) of 850°C 1hr sample NiAl/ γ -Al₂O₃ interface and corresponding O-K edge (b), Ni-L edge (c) EELS mapping, no nickel is detected inside the oxide film.

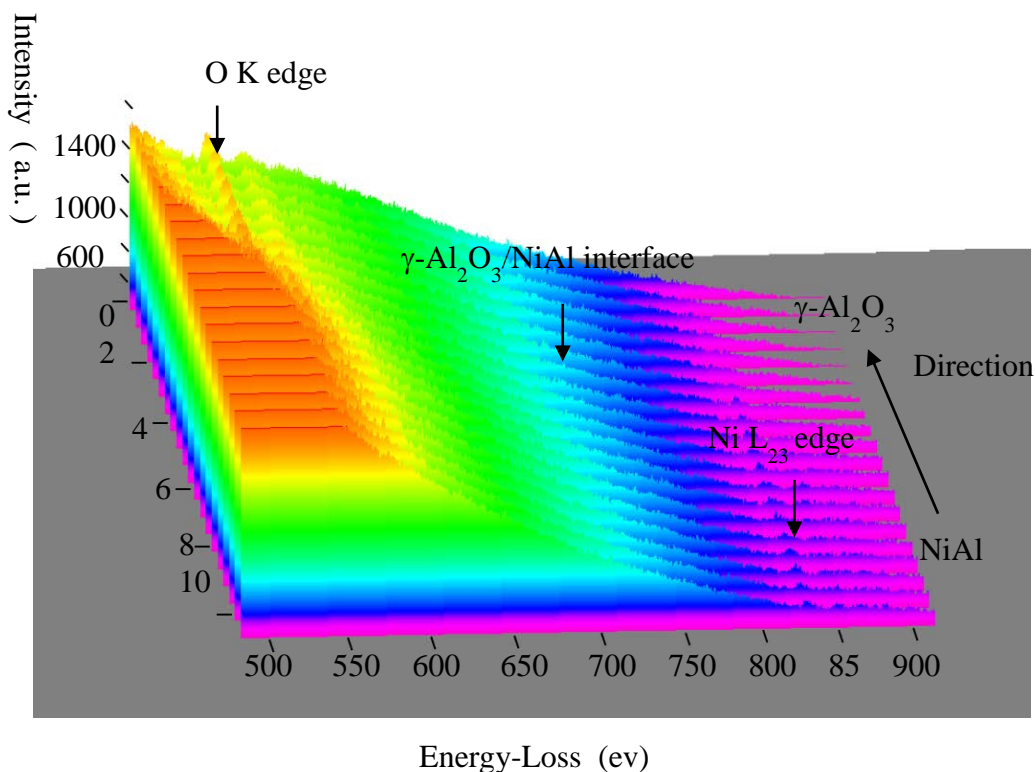


Figure 4.8 EELS line scan spectrum across $\gamma\text{-Al}_2\text{O}_3/\text{NiAl}$ interface indicated the probable interface (1\AA probe size) and the absence of Ni inside of the oxide film.

In the EELS line scan spectra, the Ni L_{23} spectrum started to decrease on approaching the NiAl/ $\gamma\text{-Al}_2\text{O}_3$ interface and finally disappeared at NiAl/ $\gamma\text{-Al}_2\text{O}_3$ interface. Correspondingly, the O K edge peak appeared at the NiAl/ $\gamma\text{-Al}_2\text{O}_3$ interface, which indicated a sharp (in a vicinity of $\sim 2\text{\AA}$) metal/oxide interface. By comparing the Ni L spectrum from the interface and the bulk NiAl, no detectable peak shift was observed. Similar results were also observed from O K spectra of from bulk Al_2O_3 oxide and the metal/oxide interface, with a given spectrum position and shape matching close with each other. The O K edge and Ni L_{23} edge EELS results did not reveal any change at the interface. To maintain similar electronic states across the metal/oxide

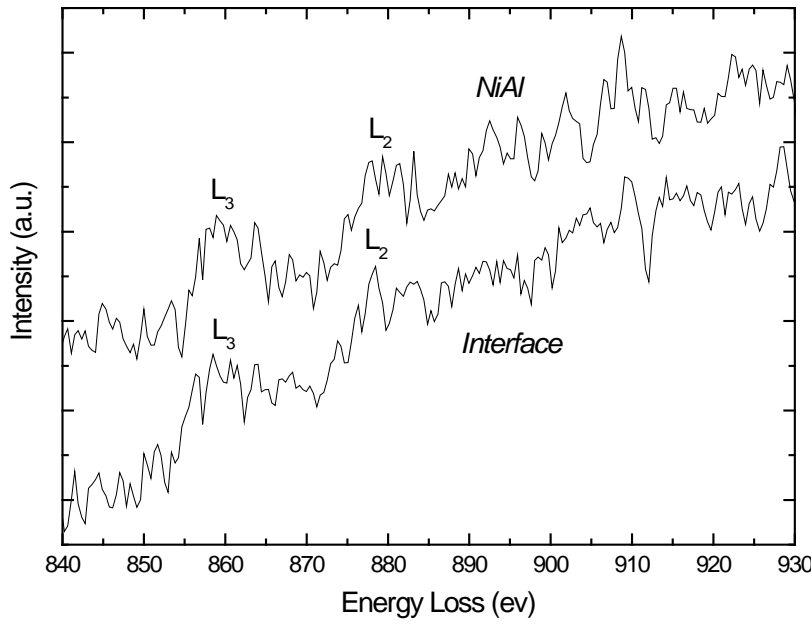


Figure 4.9 EELS Ni L_{23} edge spectrum from interface and bulk NiAl

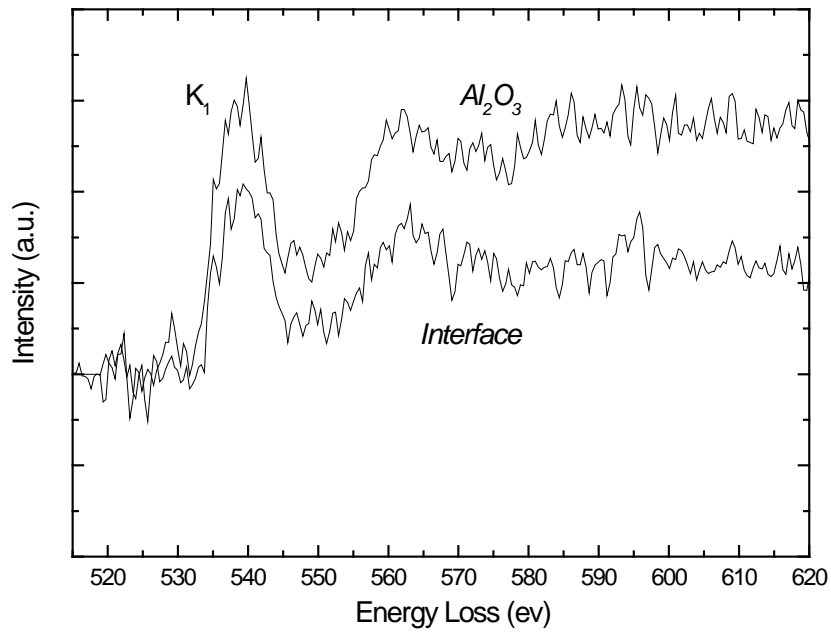


Figure 4.10 EELS O K_1 edge from γ - Al_2O_3 film and interface.

interface, the bonding across NiAl/ γ -Al₂O₃ interface could be the cation Ni-Al bonding to form the γ -Al₂O₃ oxide film. However, further detailed experiments are needed to confirm that these results reflect the interfacial bonding and not an artifact of sampling more “bulk” than interface. Both EELS mapping and spectra confirm the γ -Al₂O₃ formation with the absence of NiAl₂O₄ and NiO appearances.

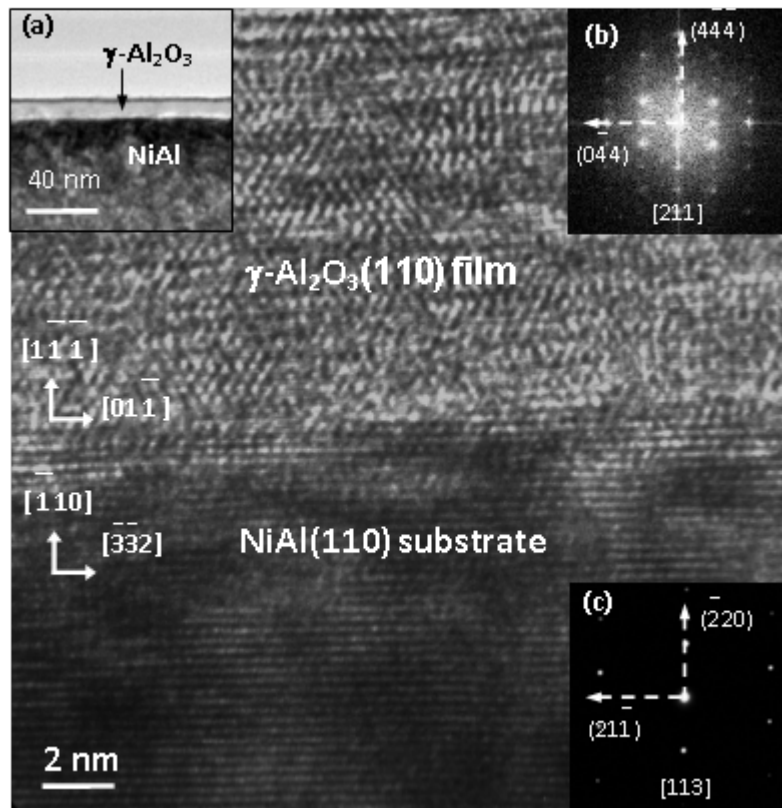


Figure 4.11 Cross-sectional HRTEM image of 650°C 2hr oxidized NiAl/ γ -Al₂O₃ interface, (a). 18nm continuous oxide on NiAl substrate. (b). γ -Al₂O₃ HRTEM FFT pattern. (c). NiAl Select area diffraction along interface.

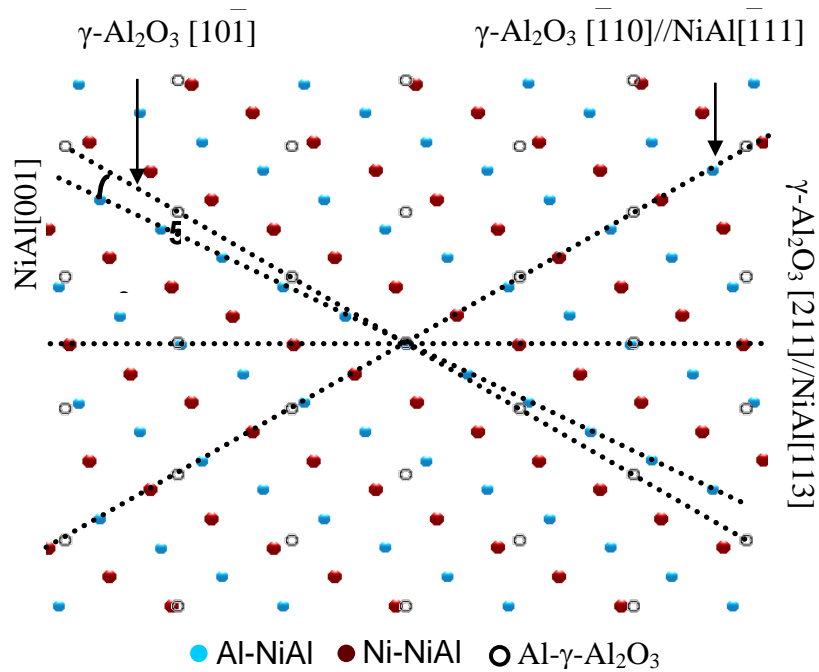


Figure 4.12 Top view schematic rigid atom matching of 650°C 2 hrs oxidized $\gamma\text{-Al}_2\text{O}_3(111)$ overlay on NiAl(110) with $\gamma\text{-Al}_2\text{O}_3[211]||\text{NiAl}[113]$ axis matching. $\gamma\text{-Al}_2\text{O}_3(111)[110]||\text{NiAl}(110)[111]$ with $\gamma\text{-Al}_2\text{O}_3[101]$ 5.26° away from NiAl[001] can be achieved which is the KS O.R.

We also examined the $\gamma\text{-Al}_2\text{O}_3$ formation at $T=650^\circ\text{C}$, 750°C and 950°C by XTEM, and noted the changes of the metal/oxide relative orientation relations as a function of thickness and temperatures as well as the $\gamma\text{-Al}_2\text{O}_3$ crystal structure changes at different conditions. After oxidation at the lowest oxidation temperature of 650°C for 2 hrs in air, an 18 nm $\gamma\text{-Al}_2\text{O}_3$ film formed (Figure 4.11). The SAD and FFT of the HRTEM image showed $\text{NiAl}(110)[113]||\gamma\text{-Al}_2\text{O}_3(111)[211]$ orientation relation. Accordingly, a top view schematic diagram of the

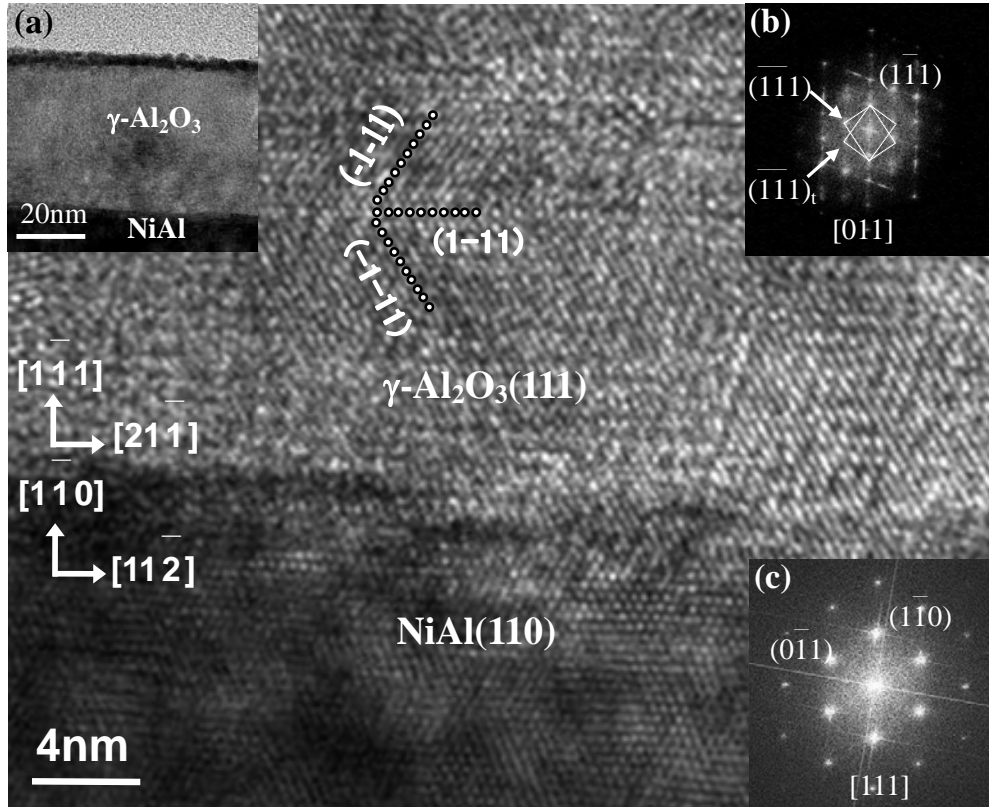


Figure 4.13 Cross-sectional HRTEM image of 750°C 2hr oxidized $\gamma\text{-Al}_2\text{O}_3/\text{NiAl}$ interface, (a). TEM image of continuous thin oxide film formed on NiAl substrate; (b). $\gamma\text{-Al}_2\text{O}_3$ FFT with twin pattern along (111) plane. (c). NiAl FFT pattern.

observed $\gamma\text{-Al}_2\text{O}_3$ formation on NiAl at 650°C oxidation was generated to understand the orientation relation at the interface, as shown in Figure 4.12. At the intermediate temperature of 750 °C and 2hrs oxidation, a 40nm $\gamma\text{-Al}_2\text{O}_3$ film formed and the orientation relation is the Kurdjumov–Sachs (KS) O.R. of $\text{NiAl}(\bar{1}10)[111]||\gamma\text{-Al}_2\text{O}_3(\bar{1}11)[011]$ growth epitaxy, as shown in Figure 4.13. The HRTEM images of the oxide film revealed $\gamma\text{-Al}_2\text{O}_3\langle 111 \rangle$ type twin boundaries. NB-EDP from the thin $\gamma\text{-Al}_2\text{O}_3$ film region was taken along the $\gamma\text{-Al}_2\text{O}_3[011]$ zone axis and compared with a simulated twin diffraction pattern, Figure 4.14 (a and c). The

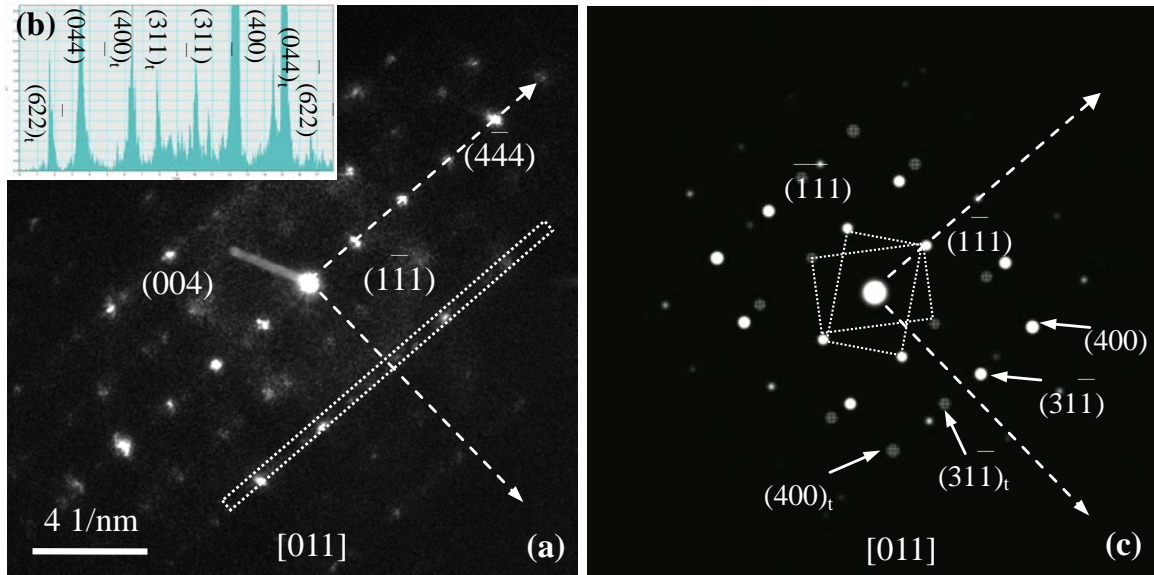


Figure 4.14 (a). NB-EDP from 750°C 2hr oxidized γ -Al₂O₃ film confirmed γ -Al₂O₃ with (111) twin defects, (b). Intensity profile of NB-EDP from the lower dotted area shows the twin diffraction with respect to (111) mirror plane. (c). Schematic γ -Al₂O₃ (111) twin diffraction pattern at [011] zone axis.

intensity profile taken along γ -Al₂O₃<111> revealed a series of twined planes with respect to the (111) plane, which is the γ -Al₂O₃ growth direction. Figure 4.15 shows pairs of bright-field (BF) and dark field (DF) cross-sectional TEM images and the corresponding diffraction patterns (insets in BF image) of the NiAl/ γ -Al₂O₃ film at the highest temperature examined, 950°C and 1hr oxidation. Sharp and incomplete rings appeared on the SAD which implied the formation of textured grains. The grains in polycrystalline thin film usually shows a preferred orientation [86,111]. In our study, lamellar textured grains could be found in the film (111)

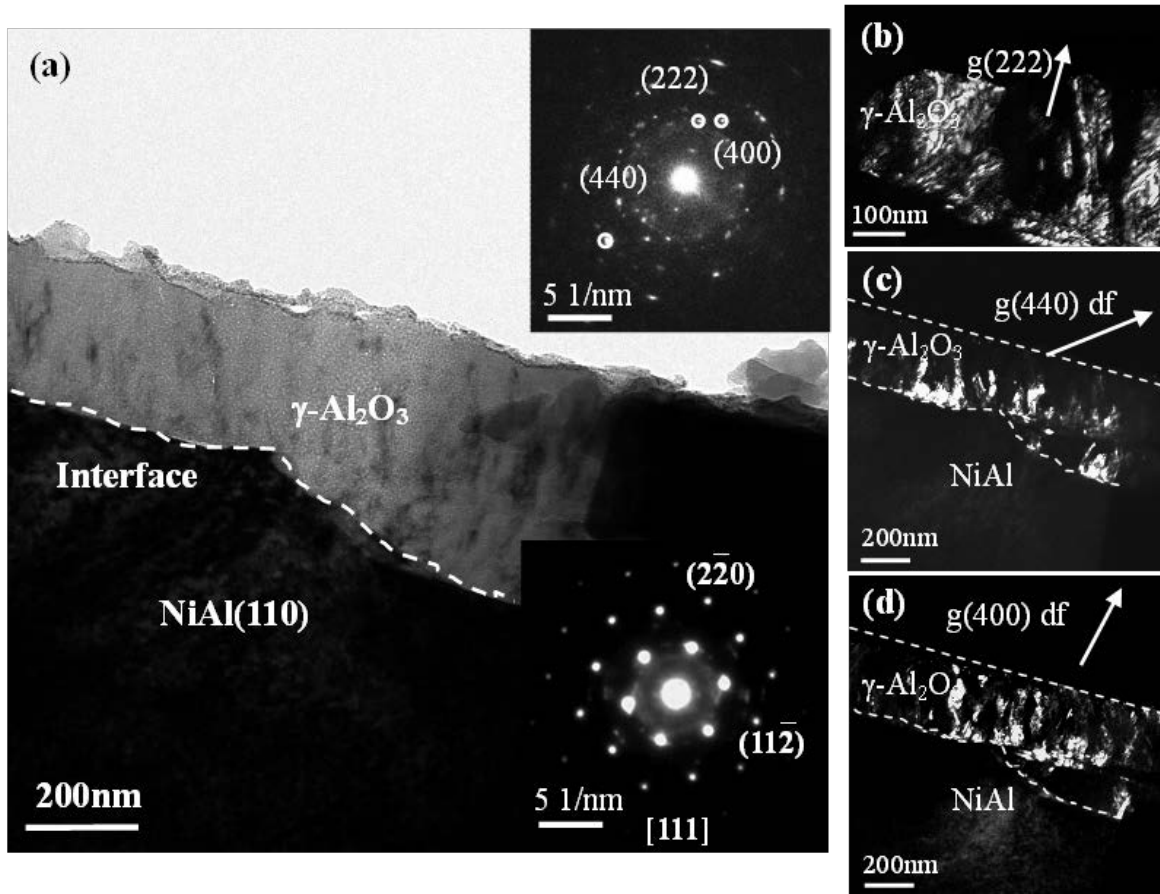


Figure 4.15 Cross-sectional TEM images γ - Al_2O_3 film structure from 950°C 1hr oxidation. (a).BF image of $\sim 300\text{nm}$ γ - Al_2O_3 film on NiAl(110), with SAD from γ - Al_2O_3 film (upper corner) and NiAl substrate (lower corner) inset. (b). γ - Al_2O_3 DF image of (222) diffraction spot showed textured polycrystalline with preferred in-plane (111) orientation. (c) and (d). Corresponding DF images using γ - Al_2O_3 (440) and (400) diffraction spots indicated nano sized oxides formation.

direction. Strong (111) diffraction spots of the oxide film were noted that a textured (111) plane oxide film developed with nano-polycrystalline structure, as shown from DF images. This also agrees with the XRD results of 950°C oxidation where only γ - Al_2O_3 (111) peaks were found. DF imaging using the γ - Al_2O_3 (111) diffraction spot indicated dominant (111) textured grains

(Figure 4.15b). In addition, nano-sized oxides were observed inside the film and along the meta/oxide interface, which were imaged using (440) and (400) diffraction spots to form DF images, Figure 4.15 (c and d).

4.1.3 Interlayer phase separation

After NiAl oxidation at 750°C for 1hr, a phase separation was observed along NiAl|| γ -Al₂O₃ interface. Cross-sectional TEM images (Figure 4.16a) indicated a 20nm thick intermediate phase induced contrast at the NiAl/ γ -Al₂O₃ interface region. As seen in the Ni-K and Al-K energy dispersive spectroscopy (EDS) mapping from Figure 4.16 (b and c), three regimes are identified in phase contrast from the bright field TEM image: a NiAl substrate, a Ni rich intermediate region and a pure Al₂O₃ layer.

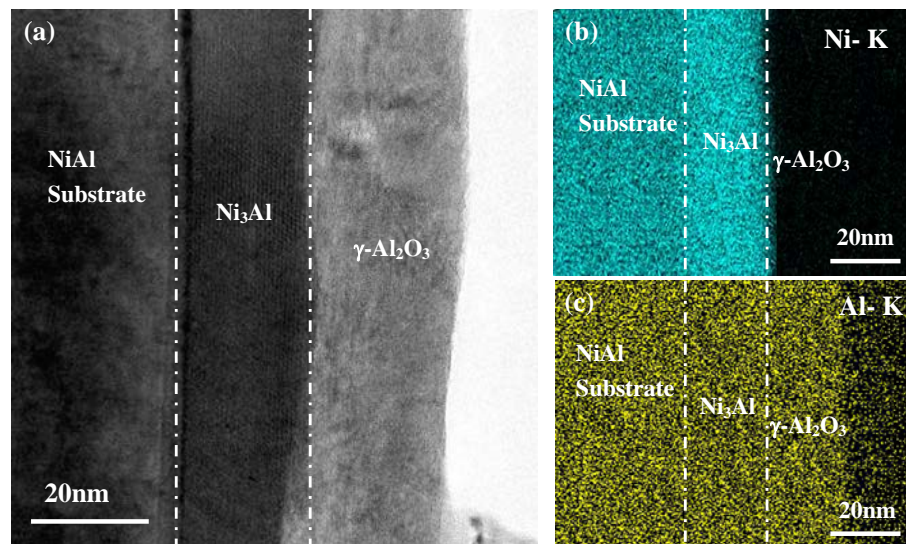


Figure 4.16 Cross-sectional TEM image of 750°C/1hr oxidized NiAl/ γ -Al₂O₃ interface showed Ni₃Al precipitation with corresponding Ni-K edge (b) and Al-K edge (c) EDS mapping.

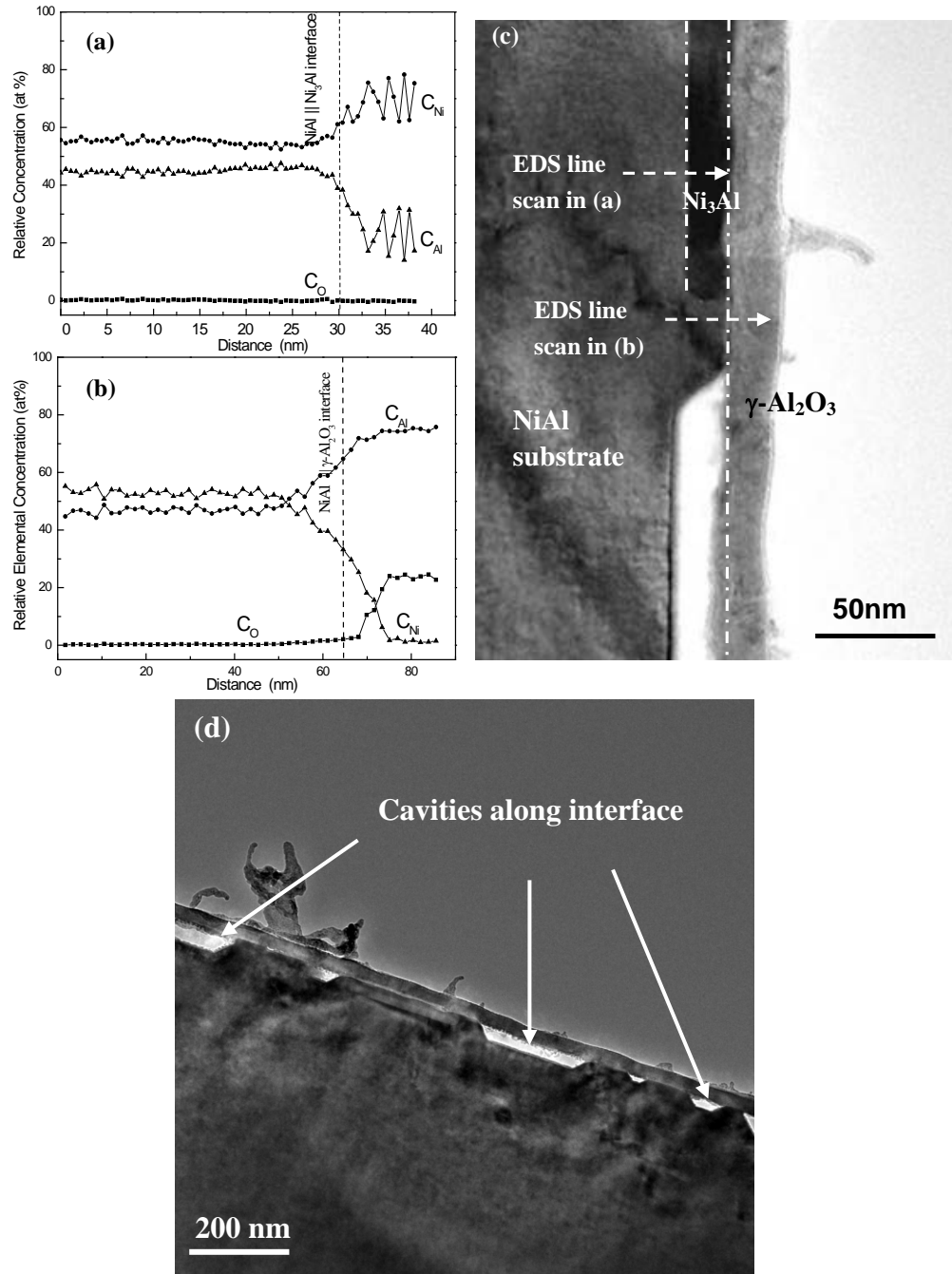


Figure 4.17 Relative concentration profiles of Ni, Al and O elements across NiAl/ γ -Al₂O₃ interface of 750°C 1hr oxidized NiAl. (a). EDS line scan across Ni₃Al separation region, (b). EDS line scan across non-phase separation region, (c). Cross-sectional TEM BF image of 750°C 1hr oxidized NiAl(110), (d). Large cavities formation was observed along the NiAl/ γ -Al₂O₃ interface.

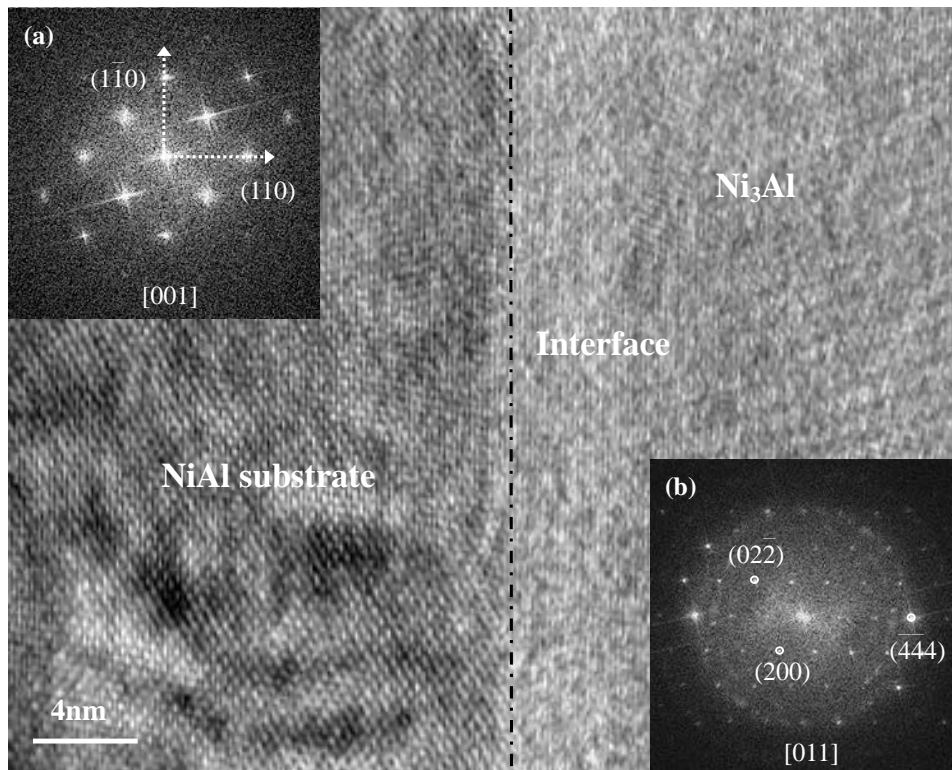


Figure 4.18 HRTEM interface image of NiAl and Ni₃Al precipitate at 750°C 1hr oxidation indicated NiAl(110)[001]|| Ni₃Al($\bar{1}\bar{1}\bar{1}$) [011] epitaxy: (a). FFT pattern of NiAl substrate. (b). FFT pattern of Ni₃Al phase.

Semi-quantitative EDS line scans of Ni and Al elements crossed over the NiAl/Ni rich region and NiAl/ γ -Al₂O₃ interfaces (Figure 4.17 a and b) showed high Ni concentration, low Al concentration and no O content in the intermediate region. The absence of Ni in the Al₂O₃ film further affirmed that the oxide is γ -Al₂O₃ and not NiAl₂O₄. Also, a large area of voids was observed under BF imaging, as shown in Figure 4.17d. The formation of voids was believed to be associated with the γ' phase appearance which reduced the Al supply for the oxide scale growth. HRTEM images taken around Ni rich region (Figure 4.18) with corresponding FFT

patterns identified the precipitate phase to be γ' -Ni₃Al which possesses face centered cubic structure with Pm3m space group. The growth epitaxy relationship between the NiAl and γ' phase could be expressed as NiAl(110)||Ni₃Al(111) and NiAl[001]||Ni₃Al[011].

4.2 DISCUSSION OF γ -ALUMINA FORMATION

4.2.1 γ -Al₂O₃ microstructure and orientation at various oxidation conditions

γ -Al₂O₃ has a spinel structure which is face-centered cubic (FCC) with a lattice constant of 7.908Å, in comparison to NiAl which is the B2 structure with $a_o = 2.882\text{Å}$. To obtain single crystal γ -Al₂O₃ thin-film formation, Frank-van der Merwe layer-by-layer growth is favorable with low interfacial energy [31]. Thus a small lattice mismatch should be found of the NiAl/ γ -Al₂O₃ interface. Because of the large unit cell of γ -Al₂O₃, it is possible for low index NiAl planes to match with higher index γ -Al₂O₃ plane. From 850°C 1hr TEM results, Figure 4.5, NiAl (200) planes are parallel to γ -Al₂O₃ (440) planes along the interface. The corresponding lattice mismatch between the d spacing of NiAl (200) and γ -Al₂O₃ (440) are 3.7%, which is consistent with the measured electron diffraction patterns of γ -Al₂O₃ ($\bar{4}\bar{4}0$) and NiAl($\bar{2}00$) (Figure 4.5b). The primary in-plane O.R. were determined to be NiAl(011)[110]|| γ -Al₂O₃(111)[211] and NiAl(011)[100]|| γ -Al₂O₃(111)[110] which is the classical Nishiyama-Wasserman (NW) simple row matching with least interfacial energy.

At low temperature 650°C 2 hrs oxidation, NiAl($\bar{1}10$) [113]|| γ -Al₂O₃($\bar{1}11$) [211] with consistent (111) γ -Al₂O₃ layer growth was observed. The FCC γ -Al₂O₃ on BCC NiAl orientation epitaxy can be demonstrated as follows. With the top surface of FCC(111)||BCC(110) and FCC<211>||BCC<311>, six combinations of FCC<211> || BCC<311> could be obtained with the interplanar relation of FCC<211> perpendicular to FCC(111) and BCC<311> perpendicular to BCC(110), respectively. FCC [$\bar{2}11$] ||BCC [$\bar{1}13$] is displayed to simulate the orientation relation observed at 650°C 2 hr oxidation in the top view of NiAl[110]|| γ -Al₂O₃[111], Figure

4.12. Because of the interplanar relationship in cubic system, FCC $(\bar{1}10)$ and FCC $(10\bar{1})$ are $\pm 30^\circ$ away from FCC $[\bar{2}11]$. Meanwhile, BCC $[\bar{1}11]$, is 30° from BCC $[\bar{1}13]$. Accordingly, FCC $[\bar{1}10] \parallel$ BCC $[\bar{1}11]$ is obtained. Based on the interplanar angles in cubic crystal are that $\langle 100 \rangle$ is 54.7° relative to $\langle 111 \rangle$ and $\langle 110 \rangle$ is 60° to $\langle 110 \rangle$, then angle between BCC $[100]$ and FCC $[\bar{1}10]$ can be calculated as $60 - 54.74 = 5.26^\circ$. Consequently, $\gamma\text{-Al}_2\text{O}_3(111)[\bar{1}10] \parallel \text{NiAl}(110)[\bar{1}11]$ with $\gamma\text{-Al}_2\text{O}_3[\bar{1}0\bar{1}]$ 5.26° away from NiAl $[001]$ orientation relationship is achieved which establishes the classical Kurdjumov–Sachs (KS) O.R. at $\gamma\text{-Al}_2\text{O}_3(111)[\bar{2}11] \parallel \text{NiAl}(\bar{1}10)[113]$ epitaxy.

According to Young's equation, layer by layer growth will only occur when the sum of the surface free energy of oxide film $\sigma_{\gamma\text{-Al}_2\text{O}_3(111)}$ and the interfacial free energy of $\sigma_{\gamma\text{-Al}_2\text{O}_3(111)/\text{NiAl}(110)}$ is smaller than NiAl surface free energy $\sigma_{\text{NiAl}(110)}$, i.e.

$$\Delta\sigma = \sigma_{\gamma\text{-Al}_2\text{O}_3(111)} + \sigma_{\gamma\text{-Al}_2\text{O}_3(111)/\text{NiAl}(110)} - \sigma_{\text{NiAl}(110)} \leq 0 \quad (4.1)$$

Density function theory calculation has been done to obtain $\sigma_{\gamma\text{-Al}_2\text{O}_3(111)} = 1 \text{ J/m}^2$ and $\sigma_{\text{NiAl}(110)} = 1.8 \text{ J/m}^2$ [40,112]. Both NW and KS O.R. relaxed maximum atoms of overlayer sitting in minimum of substrate corrugations and minimized the NiAl(110)/ $\gamma\text{-Al}_2\text{O}_3(111)$ interfacial energy σ , thus $\sigma_{\text{NiAl}(110)/\gamma\text{-Al}_2\text{O}_3(111)} < 0.8 \text{ J/m}^2$ is attained to satisfy the layer growth condition and form $\gamma\text{-Al}_2\text{O}_3(111)$ single crystal.

At 950°C 1hr oxidation, both XRD and TEM results showed textured $\gamma\text{-Al}_2\text{O}_3(111)$ polycrystalline formation. The appearance of nanocrystalline microstructure shown in Figure 4.15 confirmed that, at high temperature oxidation, nucleation sites occurred around the NiAl/ γ -

Al_2O_3 interface as well as inside of the oxide film, thereby creating more short-circuit diffusion path for ion and defects migration. Although the (111) plane is the preferred growth orientation, more nucleation sites assisted the oxide growth for various orientations and, hence, became polycrystalline. The oxidation rates were enhanced by the high defect concentrations around the grain boundaries which led to a 290nm thick defective film at 950°C compared to 80nm single crystal film at 850°C for the same treatment period (Table 4.1). By distinguishing the approximate outline of (111) EDP excited grains (Figure 4.15b), a typical platelet grain morphology was found in the oxide scale which led to the plate-like surface morphology as observe by SEM (Figure 4.2). This initial platelet structure will finally develop to the whiskers-like morphology as researchers reported in the extended oxidation of NiAl [94]. The $\gamma\text{-Al}_2\text{O}_3$ thin film growth epitaxy and microstructure as a function of thickness is tabulated in Table 4.1.

4.2.2 Interfacial strain induced evolution of $\gamma\text{-Al}_2\text{O}_3$ growth epitaxy

Concerning the temperature effect (650~850°C) on the oxide thickness, for BCC(110)||FCC(111), epitaxial relationships were usually found to be the predicted NW O.R. or KS O.R. which could be distinguished by the in-plane orientations. In the demonstrated experiment, at low temperatures with the thinner films, NiAl/ $\gamma\text{-Al}_2\text{O}_3$ maintained KS O.R. which later transformed into NW O.R. when the film was grown thicker at higher temperatures. At the intermediate thickness, $\gamma\text{-Al}_2\text{O}_3(111)$ formed with widespread twin defects. During the film growth, there are basically two types of stresses that arise: elastic mismatch stresses due to lattice misfit between the film and support and thermal residual stresses due to differences in the coefficient of thermal expansion (CTE) mismatch between the various layers. The thermal residual stresses induced strain energy is usually employed to evaluate the adhesion or wear

resistance of the film, which is only dependent on the CTE differences between the film and the substrate. Whereas the elastic mismatch induced strain energy will govern the crystallographic orientation between the film and substrate. The reason is that the elastic mismatch energy is arisen from the interfacial lattice misfit and thus can be lowered by changing of the atomic epitaxy in certain orientation to obtain the minimize-energy configuration. In a rigid-lattice approximation, the relative orientations between the film and substrate induced strain energy was systematically studied by the Bauer and van der Merwe model and can be applied to interpret the evolution of γ -Al₂O₃ structure and orientation during growth at various conditions [113]. The oxide layer growth orientation can be determined by both the interfacial geometry parameter, r , and interaction parameter l , where l expresses the relative strength of intralayer to layer-substrate interactions. In the case of interfacial lattice matching, $r=b/a$, where b and a are the nearest-neighbor distances of γ -Al₂O₃ and NiAl. See equation 4.2,

$$b = 7.9\sqrt{2} / 4 = 0.28nm, a = 2.88\sqrt{3} / 2 = 0.25nm, r=b/a=1.12 \quad (4.2)$$

The interaction strain change from thin layer to thick film can be expressed by the rigid modulus assumption [114], where the n -fold layer system is approximately \sqrt{n} times the monolayer l , i.e.

$$l=x^{1/2}l_0 \quad (4.3)$$

where l_0 is the interaction parameter of 1nm thick layer, x is film thickness.

The γ -Al₂O₃ interaction parameter as a function of film thickness can be calculated as indicated in Table 4.1. In both strong and weak layer-substrate interaction, the predicted orientation relationship with minimum energy could be expressed qualitatively as a function of l and r shown in Figure 4.19. Considering $r = 1.12$ and alteration of l during growth, in initial thin layer growth stage when l was trivial, the lattice parameter governed the energetically favorable KS orientation growth. With increasing oxidation temperature, oxide growth kinetics was

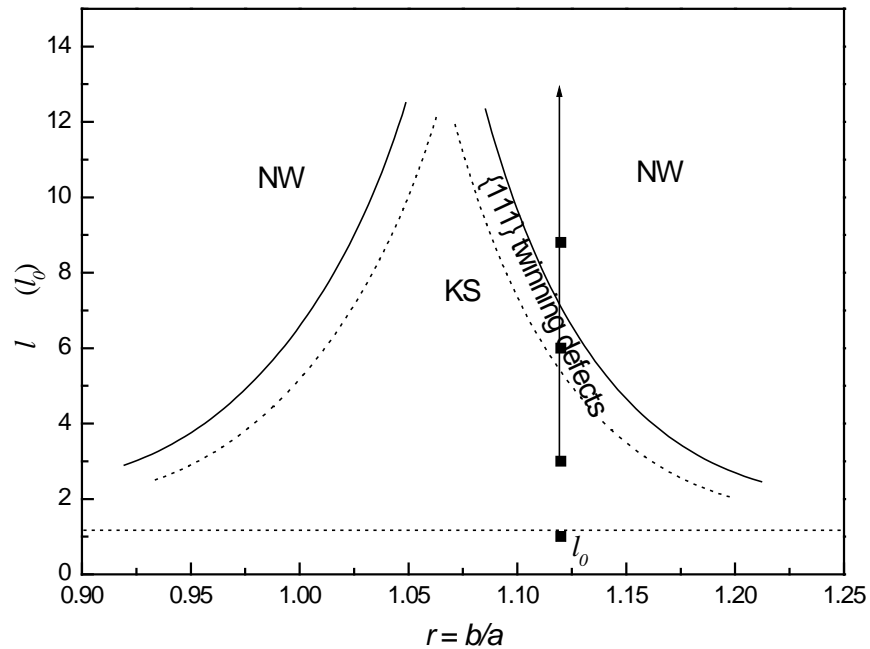


Figure 4.19 Epitaxy stability diagram of $\gamma\text{-Al}_2\text{O}_3$ growth as a function of r and l , KS transforms into NW O.R. with l increasing, a $\gamma\text{-Al}_2\text{O}_3$ {111} twinning defects regime is expected along the KS/NW boundary.

promoted and led to an intermediate thickness region with higher l , due to the accumulated growth stress during oxide formation, the $\gamma\text{-Al}_2\text{O}_3$ {111} deformation twins arose to compromise the system strain energy before the switchover from KS O.R. to NW O.R happened. As the $\gamma\text{-Al}_2\text{O}_3$ layer cross over to thicker regime, strain-induced transformation from the KS O.R. to the NW O.R. may take place and that NW epitaxy is energetically favorable to form and persist in further oxide growth [113,115].

4.2.3 Driving force for phase separation at 750°C 1hr oxidation

In γ -Al₂O₃ formation, the outward migration of Al forms a continuous oxide layer on the alloy surface. Since Ni does not enter into oxide formation it is inevitable that it will concentrate at the scale–metal interface and, correspondingly, the Al will be depleted. A gradient of the Al concentration and outward diffusion of Al would consequently result in an opposite gradient of Ni concentration and an inward flux of Ni takes place. The fast growth of metastable γ -Al₂O₃ oxide led to Ni and Al concentration gradients arising during oxidation (Figure 4.17 a and b) which eventually resulted in cavity formation and phase separation (Figure 4.17c).

The planar and flat NiAl/ γ -Al₂O₃ interface suggests the growth rate is controlled by ionic diffusion through the oxide. When the scale growth is controlled by diffusion in NiAl, the oxide/substrate interface will become unstable and wavy because of the inward protuberance of the oxide, which will shorten the diffusion distance across the NiAl. In case the migration of ions and electrons across the oxide is a rate-controlling process, the growth kinetics of the oxide film will follow the parabolic rate law[116],

$$x^2 = k' \cdot t \quad (4.4)$$

where k' is the parabolic rate constant of thickness as a function of temperature, x is the scale thickness and t is the oxidation time. The oxide thickness growth rate will be expressed as shown below,

$$\frac{dx}{dt} = \frac{k'}{2x} \quad (4.5)$$

From the Ni-Al binary phase diagram, Ni₃Al precipitate formation will happen at a Ni concentration ~ 72 at% around 750°C. The Ni₃Al phase separation along the metal/oxide interface will be determined by both the consumption of Al atoms to form a γ -Al₂O₃ layer and

the Al atoms supply from the substrate, i.e., the oxide growth rate, dx/dt , and diffusion coefficient, $\tilde{D}_{(Al)}$, in NiAl. To avoid abrupt concentration deviation caused by Ni₃Al phase formation, diffusion in the alloy must be rapid enough to supply the solute at least at the rate it has being consumed by oxide growth. A detailed quantitative model of the phase formation thermodynamics and kinetics was presented in Appendix II.

At low temperature 650°C with small k' , the slow oxide growth resulted in negligible Al concentration deviation at the interface. By increasing the temperature to 750°C or higher, the oxide growth is enhanced with larger k' . At the initial stage of 750°C oxidation where x is small, the oxide growth rate $k'/2x$ is relatively rapid. The Al is consumed at a fast rate and the concentration gradients are most distinct which has been shown by calculations and measurements taken at a short exposure time [117,118]. This will lead to a distinct concentration deviation and may be the reason for Ni₃Al separation along the interfacial region. As the oxidation time increases, the thickness x becomes larger resulting in the slower growth kinetics of γ -Al₂O₃, i.e., less consumption of Al from the substrate. While the growth kinetics is decreasing, the relative supply of Al from the substrate will catch up to avoid large concentration fluctuation and phase separation. This could explain the absence of phase separation at 750°C 2hrs oxidation. Also, the high diffusivity of Al elements at high temperature oxidation will also prevent the concentration deviation. The Ni₃Al precipitate lattice tends to be correlated to the NiAl matrix lattice with NiAl(110)[001]||Ni₃Al($\bar{1}\bar{1}\bar{1}$)[011] which also maintains a NW O.R. in this BCC/FCC system.

4.3 CONCLUSIONS

By using analytical HRTEM methods, layer by layer growth of γ -Al₂O₃ on NiAl(110) surface yields thin γ -Al₂O₃(111) single crystal films by the oxidation method in dry ambient air. The smoothest and high quality single crystal γ -Al₂O₃ film formed during oxidation at T = 850°C for 1hr.

The changes of the epitaxial relationship between γ -Al₂O₃ and the NiAl substrate was caused by the lattice mismatch induced strain energy during γ -Al₂O₃ growth. KS O.R. to NW O.R. transition of the γ -Al₂O₃/NiAl growth epitaxy could be explained by the interaction parameter with oxide thickness change. At the intermediate thickness, the γ -Al₂O₃ {111} deformation twins were formed to compromise the growth strain energy before the NiAl/ γ -Al₂O₃ epitaxy transition from KS O.R. to NW O.R.

γ' -Ni₃Al phase precipitates at γ -Al₂O₃/NiAl interface were observed at 750°C 1hr oxidation triggered by fast growth kinetics of oxide caused the concentration deviation.

Transition from single crystal to textured polycrystalline γ -Al₂O₃ formation was observed at 950°C oxidation due to fast nucleation rate and enhanced growth kinetics.

5.0 INTERFACIAL STUDIES OF THE INTERACTIONS BETWEEN PLATINUM NANOPARTICLES AND γ -ALUMINA SUPPORT

In this chapter, the structural relation between the Pt/ γ -Al₂O₃ by using cross-sectional transmission electron microscopy (TEM) method is presented. The Wulff-Kaischew theorem is applied to gain insights into the γ -Al₂O₃ support effects on the Pt catalyst's shape and structure.

5.1 CREATION AND CHARACTERIZATION OF MODEL Platinum/ γ -ALUMINA SYSTEM

The creation of single crystal γ -Al₂O₃ thin films is crucial for this study and its formation is described in chapter 4. By oxidation of NiAl(110) at 850 °C in air, the γ -Al₂O₃(111) thin films were prepared. Pt was evaporated onto the γ -Al₂O₃ surface by UHV electron beam evaporation at 500 °C with a deposition rate of 1 Å/sec. This processing condition created 2-5 nm Pt NPs, with a mean diameter of 3.5 nm, Figure 5.1.

Cross-sectional TEM samples were prepared by cutting a 50 nm thin Pt/ γ -Al₂O₃ section using a FEI DB235 dual-beam focused ion beam (DB-FIB) and further thinned with low energy Ar⁺ ion beam at low angles using a Fischione Model 1040 NanomillTM to remove the surface

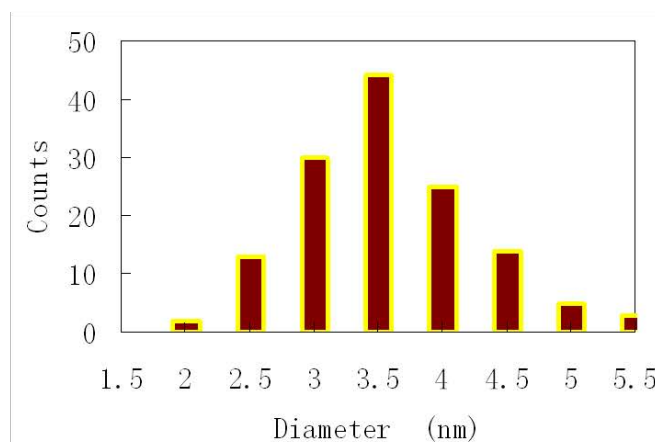
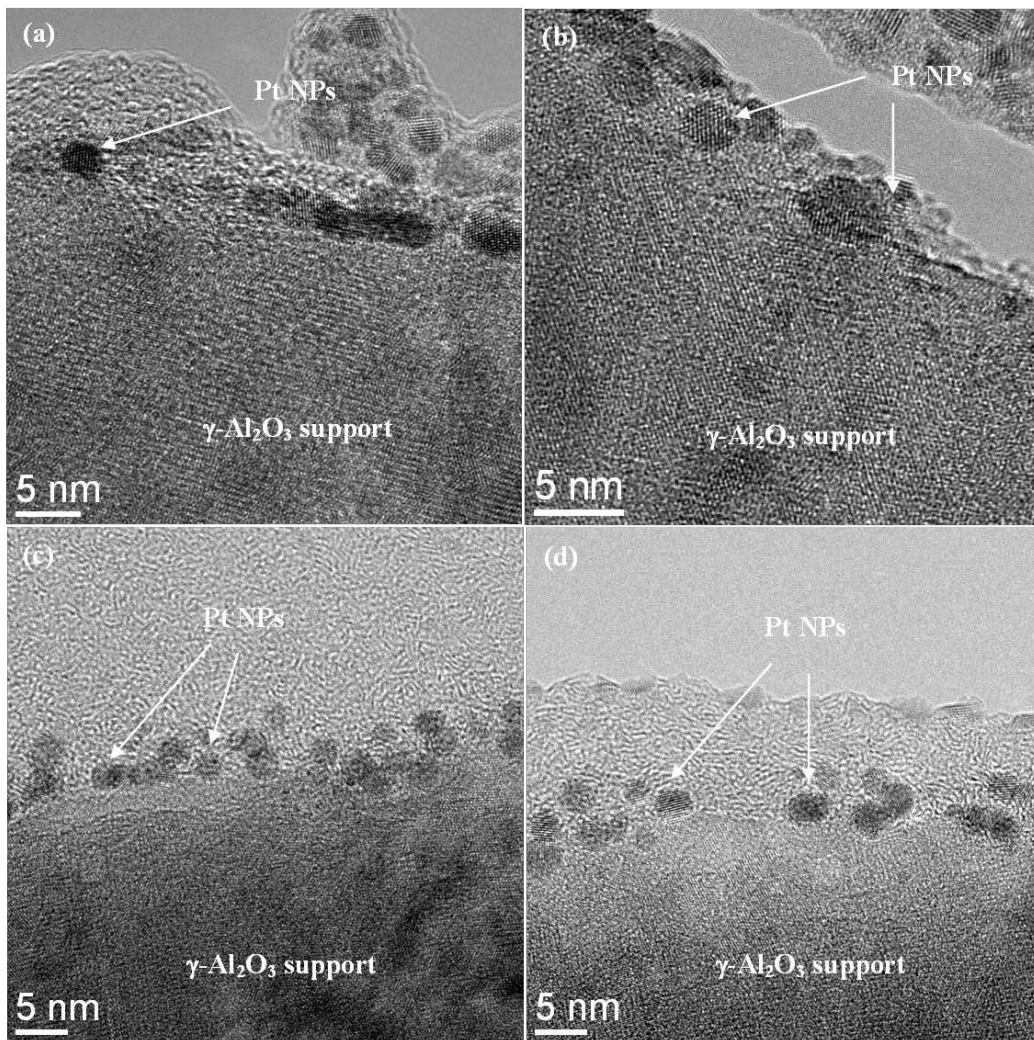


Figure 5.1 Typical TEM imaging of Pt NPs seating on the γ -Al₂O₃ support are shown in (a)~(d).

The corresponding histogram of Pt NPs size distribution from HAADF and HRTEM measurements shows a 2~5nm distribution of Pt particles.

damaged layer introduced by the DB-FIB. Electron microscopy (HRTEM) characterization were carried out within a JEM 2100FEG, Cs-corrected JEOL JEM 2200FS S/TEM, Cc-corrected Titan 80-300 and Cs corrected Hitachi HD-2300 FESEM/STEM. High-angle annular dark field (HAADF) image and HRTEM image (Figure 5.2 a and b) shows the contact between the Pt particles and the γ -Al₂O₃ support. Instead of the very small contact area, one would expect for a significant fraction of particle covering on the support with direct contact interface for HRTEM characterization. The cross-sectional TEM indicated the Pt NPs obtained an intimate contact to the support which implied a relative flat interface.

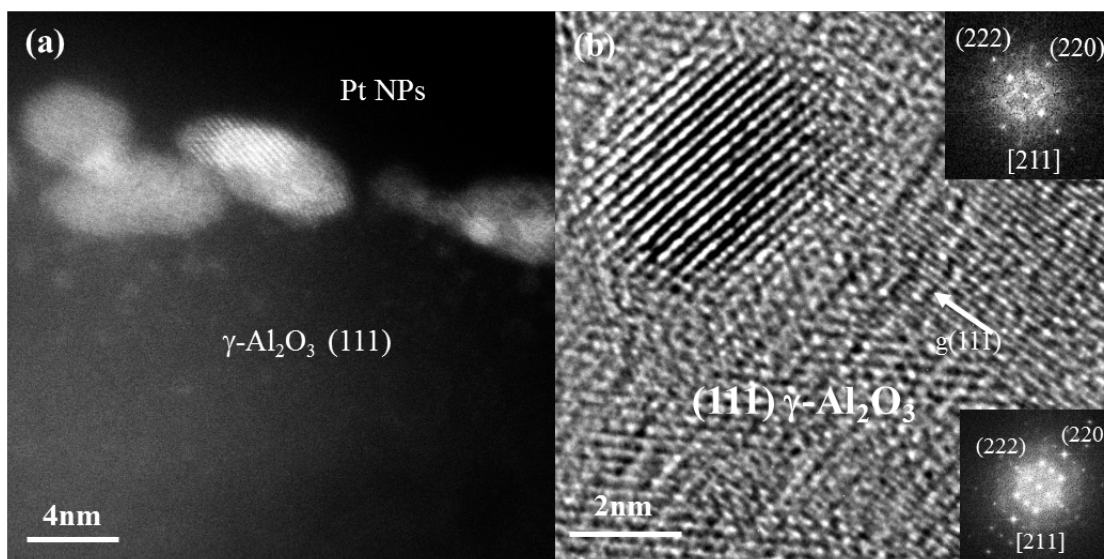


Figure 5.2 HAADF image (a) and HRTEM image (b) shows the Pt NPs is intimately contact with the γ -Al₂O₃(111) support with Pt(111)|| γ -Al₂O₃(111), interface matching is Pt(220)|| γ -Al₂O₃(440).

The relative epitaxial relationship is Pt(111)[211]|| γ -Al₂O₃(111)[211] with Pt(110)|| γ -Al₂O₃(110) (Figure 5.2 b). In the Pt/ γ -Al₂O₃ model system, two types of Pt NPs were

observed during TEM study: faceted Pt particles on the γ -Al₂O₃ surface and more rounded Pt particles with asymmetric shape. For the application of the WK theorem which applies to thermodynamically stable particles, only the symmetrical or faceted Pt particles were investigated in the present study.

5.2 PLATINUM NANOPARTICLES STRUCTURAL RELATION TO γ -ALUMINA SUPPORT

The structure of platinum is a face-centered cubic (FCC) (space group $Fm\bar{3}m$) with a lattice parameter of 3.923\AA . HRTEM revealed that some of the Pt nanoparticles were faceted as shown in Figure 5.3~5.7.

The HRTEM image (Figure 5.3 and Figure 5.5) at the Pt/ γ - Al_2O_3 interface and the corresponding Fast Fourier transforms (FFT) (Figure 5.3a inset) shows the faceted shape of a Pt particle projected normal to the electron beam direction. The HRTEM image at the Pt/ γ - Al_2O_3

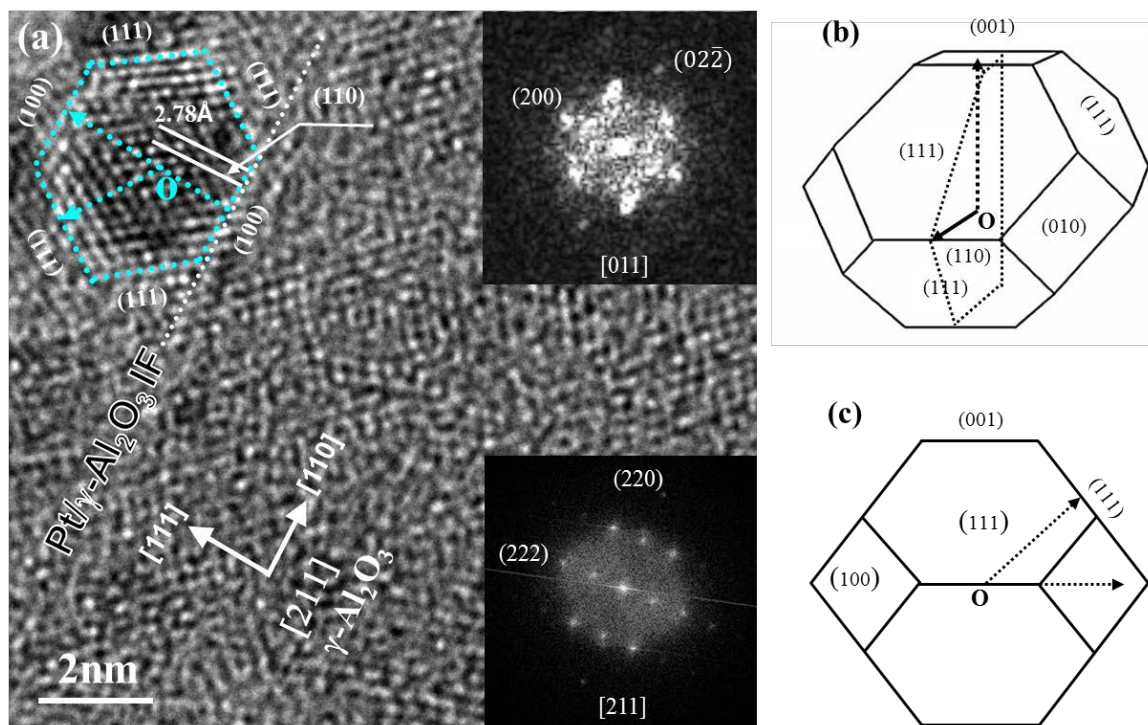


Figure 5.3 (a). Pt NP with orientation relation of $\text{Pt}(100)[011]||\gamma\text{-Al}_2\text{O}_3(111)[211]$, and interfacial epitaxy: $\text{Pt}(220) || \gamma\text{-Al}_2\text{O}_3(440)$, (b). 3 dimensional truncated octahedron of Pt, the beam direction is indicated as the solid arrow, (c). Side view of the Pt NP.

interface and the corresponding Fast Fourier transforms (FFT) indicates an epitaxial relation between Pt NPs and $\gamma\text{-Al}_2\text{O}_3(111)$ where $\text{Pt}(100)\parallel\gamma\text{-Al}_2\text{O}_3(111)$ or $\text{Pt}(111)\parallel\gamma\text{-Al}_2\text{O}_3(111)$ with $\text{Pt}[011]\parallel\gamma\text{-Al}_2\text{O}_3[211]$. Because of the large unit cell of $\gamma\text{-Al}_2\text{O}_3$, the interface lattice misfit is the low index $\text{Pt}(220)$ planes to the higher index plane $\gamma\text{-Al}_2\text{O}_3(440)$. Thus, a classical lattice-matching epitaxy (LME) growth was obtained along the $\text{Pt}/\gamma\text{-Al}_2\text{O}_3$ interface with the epitaxial mismatch m to be 1.08%, where $m = (b-a)/a$. The a and b are the interface plane spacing of the support and particles, respectively; $a = 0.1395$ nm and $b = 0.138$ nm to give m to be 1.08%. Similar epitaxy between the Pt NPs and support was also found for the $\text{Pt}(111)\parallel\gamma\text{-Al}_2\text{O}_3(111)$ shown in Figure 5.1b, a similar interface matching of $\text{Pt}(220) \parallel \gamma\text{-Al}_2\text{O}_3(440)$ was observed.

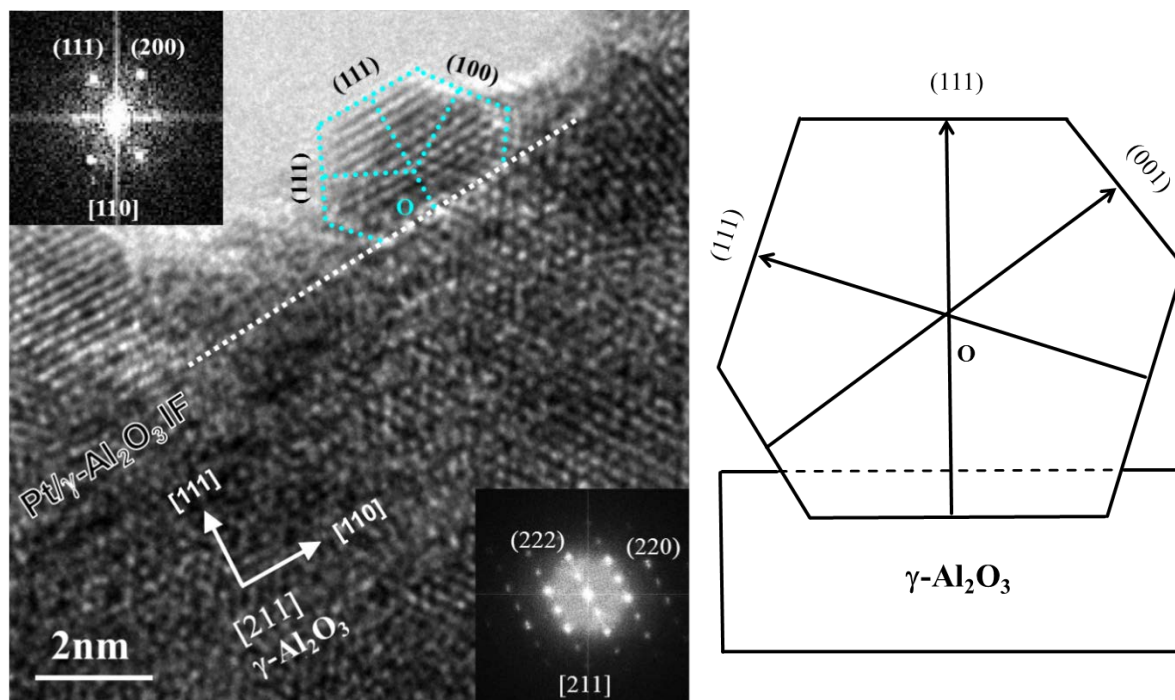


Figure 5.4 ES Pt NP with high index (062) exposing surface: $\text{Pt}(111)[110] \parallel \gamma\text{-Al}_2\text{O}_3(111)[211]$.

The HRTEM image at the Pt/ γ -Al₂O₃ interface and the corresponding FFT were utilized to describe the profile of the particles. In addition, the side view of Pt facets could help to interpret the three-dimensional shape of the particle. By using Wulff construction, former studies have demonstrated that equilibrium shape (ES) of Pt single crystal possess a truncated octahedron or a truncated cuboctahedron with dominant {100} and {111} low-index facets [119,120]. Therefore, to better understand the morphologies of the observed faceted Pt

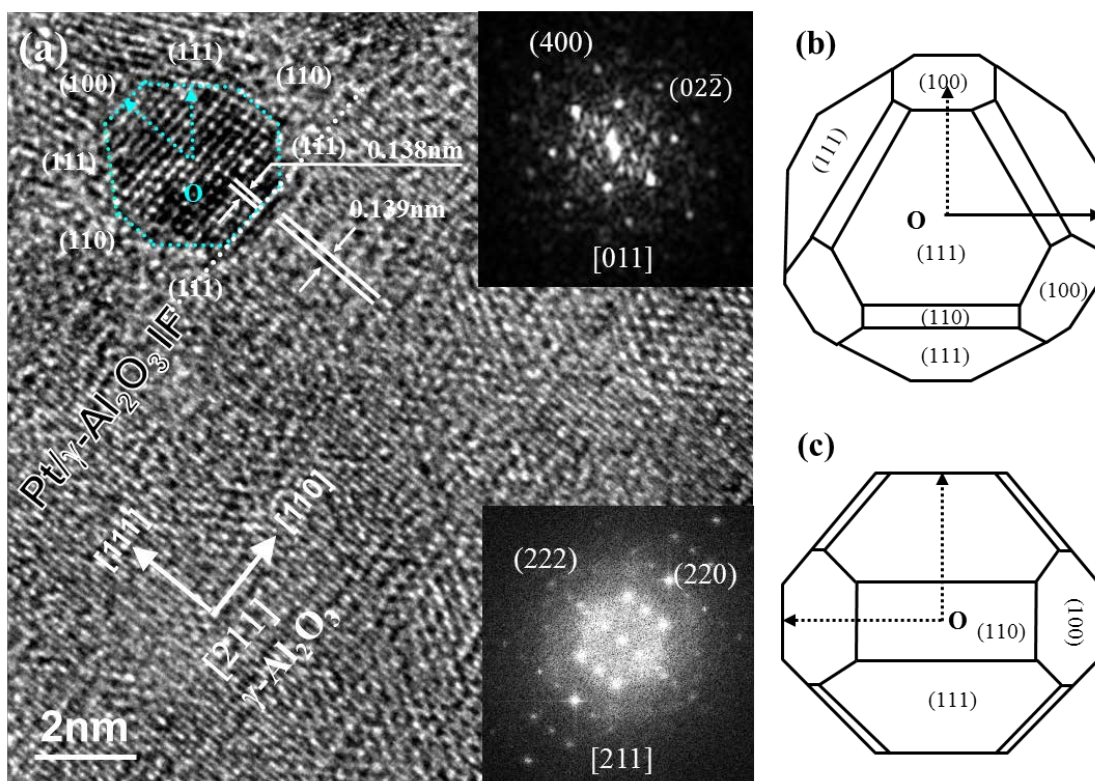


Figure 5.5 (a). HRTEM images of Pt NP with (110) facets and corresponding FFT (upper right), with epitaxy Pt(100) || γ -Al₂O₃(111) and Pt[011]|| γ -Al₂O₃[211], and interfacial planes Pt(220) || γ -Al₂O₃(440) , (b). schematic of the Pt truncated octahedron with (110) facets; the beam direction is indicated as the solid arrow and (c) corresponding schematic of side view.

nanoparticles and the relations to the HRTEM image obtained, a three-dimensional schematic of the predicted thermodynamically favorable shape with its corresponding profile were constructed to compare with the present nanoparticle shape, as shown in Figure 5.3~Figure 5.5. It could be seen that the equilibrium shape of Pt NPs is mainly composed of the low surface energy facets with {111} and {100} planes, Figure 5.3 and Figure 5.4. The schematic diagrams with corresponding profiles illustrate the observed faceted shape of Pt particle favors a truncated octahedron shape. Meanwhile, a narrow {110} facets were observed in other Pt(100) NPs on γ -Al₂O₃(111) surface with the epitaxial relation: Pt(100)|| γ -Al₂O₃(111) and Pt[011]|| γ -Al₂O₃[211]. The surface reconstruction Pt particles exhibited {110} facets (Figure 5.5) with a truncated cuboctahedral shape. In addition, a high index (062) facet on the top particle surface of the Pt NP was also observed in one nanoparticle (Figure 5.6a). The epitaxial relation was Pt(062)|| γ -Al₂O₃(111) with Pt[013]|| γ -Al₂O₃[211], and the interface plane is Pt(100)|| γ -Al₂O₃(110). A schematic diagram of the Pt/ γ -Al₂O₃ was generated to compare with the observed Pt NP shape and orientation, as shown in Figure 5.6b.

Through the HRTEM observations, most of the observed faceted Pt NPs on γ -Al₂O₃(111) were found to be Pt(100)|| γ -Al₂O₃(111) and Pt(111)|| γ -Al₂O₃(111), with Pt(110)|| γ -Al₂O₃(110) across the interface. Also, high index plane of Pt(062)|| γ -Al₂O₃(111) epitaxy was observed with Pt(100)|| γ -Al₂O₃(110) along the Pt/ γ -Al₂O₃ interface.

Wulff construction is often used to obtain the free standing equilibrium shape (ES) of single crystal nanoparticles; Pt NP is a truncated octahedron with dominant {100} and {111} low-index facets [119,120]. According to previous Wulff constructed shape of FCC metals[119], a stable ES consists almost entirely of flat {100} and {111} facets connected with each other by a narrow {110} sharp edges, as shown in Figure 5.7. Thus, the faceted Pt NPs orientation

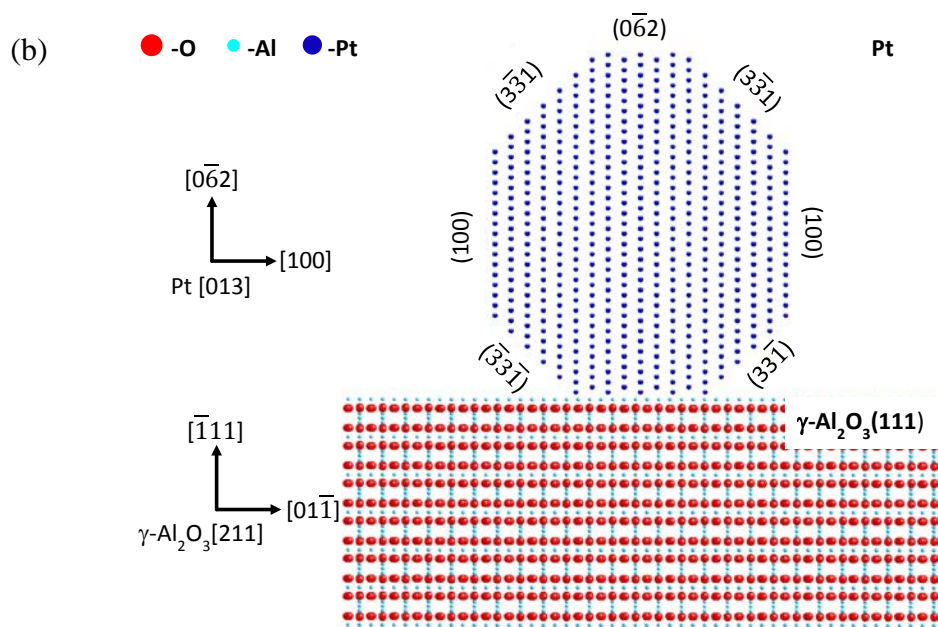
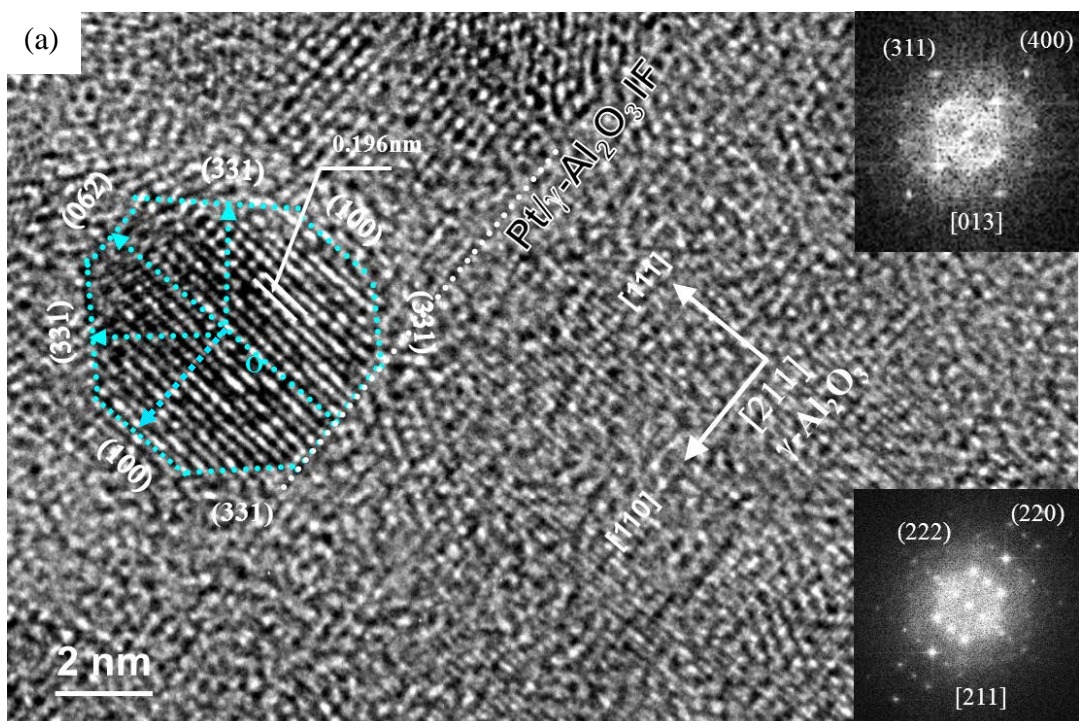


Figure 5.6 (a). Pt NP with high index (062) facet: Pt(062)[013] || γ -Al₂O₃ (111) [211], interfacial planes are Pt(100)|| γ -Al₂O₃(110), (b), schematic diagram of the Pt NP on γ -Al₂O₃.

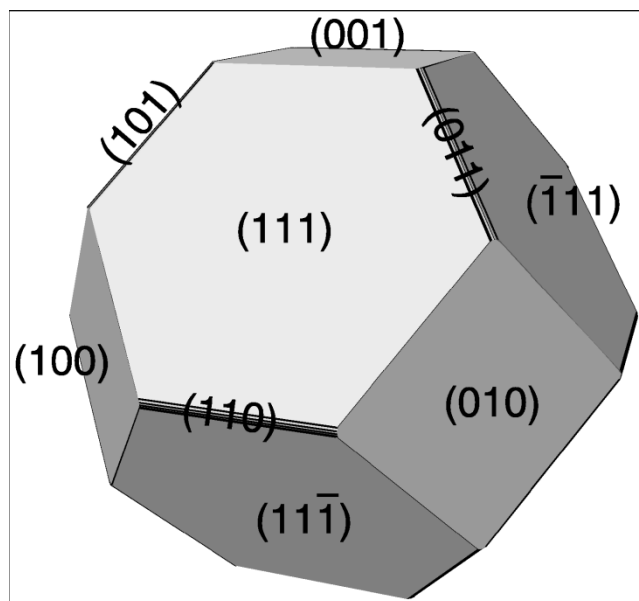


Figure 5.7 The equilibrium shape of an FCC single crystal at zero temperature obtained via the Wulff construction from the computed surface energies [119].

of Pt(100)|| γ -Al₂O₃(110) and Pt(111)|| γ -Al₂O₃(111) seems reasonable. However, evaluation of the interface between the NPs and support needs to be considered determine the ES Pt catalysts on the γ -Al₂O₃ support. By clearly identifying the shape and structural relation of Pt/ γ -Al₂O₃, the Wulff-Kaischew theorem [28,71,73,76,121] may be applied (see APPENDIX I).

In contrast to the Wulff construction, the Wulff-Kaischew construction [28,71,73,76,121], includes the interface energy where the total Gibbs free energy of the nanoparticle is composed of the chemical formation energy, the surface energy and interfacial energy, and the elastic energy stored by system. Hence knowledge of the three dimensional shape of a supported nanoparticle that is in equilibrium with the support and environment could provide essential interfacial information such as the adhesion energy via the Wulff-Kaischew construction.

5.3 EQUILIBRIUM SHAPE CONSTRUCTION OF PLATINUM NANOPARTICLES

Platinum has an fcc structure and theoretical studies of the free standing fcc metals predicted the equilibrium crystallite has a truncated octahedral shape based on the Wulff theorem, where the surface consists of {111} and {100} facets [119,120]. To better understand the morphologies of the observed faceted Pt nanoparticles and the relations to the HRTEM image obtained, a three-dimensional schematic with its corresponding profile were constructed (Figure 5.3 b and c) which illustrate the observed shape of the faceted Pt particle is also a truncated octahedron.

To understand the equilibrium shape of the nanoparticle, previous investigators used the Wulff construction [71–73] to describe the observed NPs shape and surface facets as well as determining the interfacial adhesion energies [74,75]. However, the Wulff theorem does not consider the support effects on the equilibrium shape of NPs. But, the support effects are taken into account by the Wulff-Kaischew theorem [28,71,73,76,77,121]. The total Gibbs free energy, ΔF , is composed of three terms, the chemical formation energy, surface and interface energy, and the elastic energy stored by the system, as shown below,

$$\Delta F = -\Delta\mu V + \sum_{i \neq AB} \gamma_i S_i + S_{AB}(\gamma_{AB} - \gamma_B) + \varepsilon_0 m^2 V R, \quad (5.1)$$

where $\Delta\mu$ is the supersaturation per unit volume, V is volume, γ_i is the surface energy of particle and S_i is the corresponding surface area, γ_{AB} is the interfacial energy and S_{AB} is the interface contacting area, γ_B is the surface energy of the substrate, ε_0 is the elastic coefficients of the particle and R is the relaxation energy factor. The adhesion energy, β , can then be brought into equation (1) by Dupre's equation,

$$\gamma_{AB} = \gamma_A + \gamma_B - \beta, \quad (5.2)$$

where β directly reflects the bonding properties of the metal NPs to the support oxide, γ_A is the top facet energy of the nanoparticle. In the Wulff-Kaischew theorem, the elastic energy is disregarded for the condition of trivial lattice misfit. Therefore, the equilibrium condition is obtained by taking the first order derivative of equation (5.1) to be zero. The equilibrium shape is given by equation (3) (see Appendix I),

$$\lambda = \frac{(\gamma_A - \beta)}{h_{AB}} = \frac{(\gamma_{AB} - \gamma_B)}{h_{AB}} = \frac{\gamma_i}{h_i} \quad \text{Wulff- Kaischew theorem} \quad (5.3)$$

where h_i and h_{AB} are the normal distances from the Wulff point, O, to the surfaces i and to the interface AB (Figure 5.8), λ is a constant.

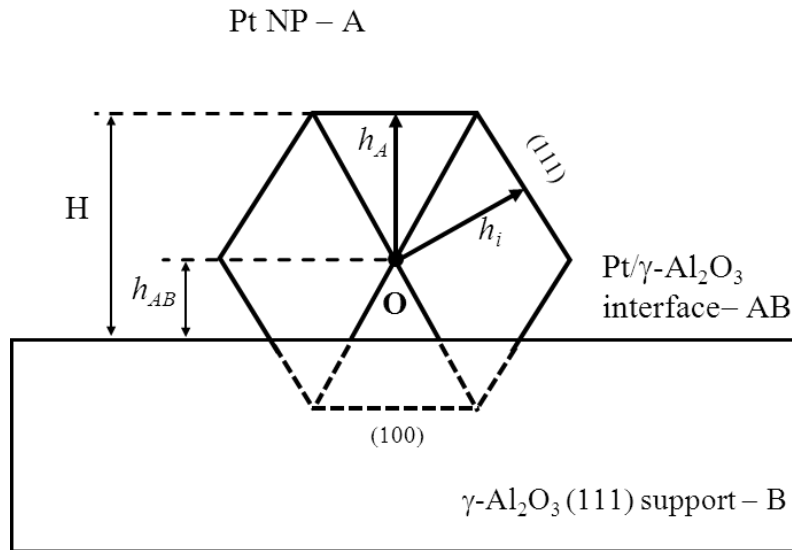


Figure 5.8 Schematic diagram of the observed Pt particle with equilibrium shape seating on γ -Al₂O₃(111) support. h_i and h_{AB} are the normal distances from Wulff point O to the surfaces i and the interface AB. $h_{AB} > 0$ means Wulff point O is above the support.

The prerequisites of applying the Wulff- Kaischew theorem is summarized below,

1. An assumption of elastic energy is negligible along the particle-support interface. This can be obtained when the lattice mismatch between particle and support across the interface is close to zero or the particle is fully relaxed on the support. The interface misfit of the Pt(220)|| γ -Al₂O₃(440) interface is $m = 1.08\%$ which we approximate as zero.
2. The three dimensional shape of the supported nanoparticles where the surface facets and interfacial orientation is known. We infer the three-dimensional shape (as shown in the schematic diagram Figure 5.3 – 5.5) from the two dimensional projection provided by HRTEM.

Table 5.1 A comparison between experimental adhesion energy data and density-functional calculated results.

	LDA-DFT [17] ($\mu\text{J}/\text{cm}^2$)	Wulff-Kaischew theorem ($\mu\text{J}/\text{cm}^2$)	Wulff theorem [122] ($\mu\text{J}/\text{cm}^2$)
Pd(100)/ γ -Al ₂ O ₃	170	—	280 \pm 20
Pt(100)/ γ -Al ₂ O ₃	83.2	69.1 \pm 5	110.3 \pm 5

If the above requirements are met, then the adhesion energy, β , and interfacial energy, γ_{AB} , can be quantitatively solved. Several parameters need to be measured in the profile view of the Pt particle, i.e., the h_i and h_{AB} , which was accomplished by measuring these parameters directly from the HRTEM images. By discerning the profile and truncation of the Pt particle in cross-sectional HRTEM imaging, the Wulff-Kaischew theorem included the shape modifications

by support to better interpret the adhesion behavior of the Pt nanoparticle on γ - Al_2O_3 support and demonstrated a consistent result with the theoretical calculations while the Wulff construction tends to achieve a higher adhesion energy (see Table 5.1). The above analysis is based on the assumption of negligible elastic energy due to the observed small lattice mismatch epitaxy across the interface.

5.4 PHYSICAL BONDING BETWEEN THE PLATINUM NANOPARTICLES AND γ -ALUMINA SUPPORT

The physical meaning of the adhesion energy, β , is defined as the work needed to separate the interface of ensemble into two free surfaces. Therefore, β directly reflects the physical/chemical bonding at the metal-oxide interface. By using density-functional theory (DFT) at the local density approximation (LDA), the adhesion energy of Pt on γ -Al₂O₃ monolayer was studied by Bogicevic and Jennison [122], the obtained calculations could be directly compared to our observation as described in Table 5.2 and Figure 5.9.

Table 5.2 LDA calculated adsorption energies for Pt particles dispersed on monolayer γ -Al₂O₃ with preferred sites (Al, O) were compared with experimental results [74,122]

	Pt-Al ($\mu\text{J}/\text{cm}^2$)	Pt-O ($\mu\text{J}/\text{cm}^2$)	Experimental Wulff-Kaischew construction ($\mu\text{J}/\text{cm}^2$)	
			Unconstructed	Reconstructed
Pt(100)/ γ - Al ₂ O ₃	124.8	83.2	69.1 \pm 2	29.2 \pm 2
Pt(062)/ γ - Al ₂ O ₃	78.6	52.4	48.3 \pm 3	
Pt(111)/ γ - Al ₂ O ₃	144.0	96.0	80.4 \pm 4	

The trends and values of the adhesion energy as a function of Pt orientations on the γ - Al_2O_3 (111) support is in reasonable agreement with the theoretical calculations, indicating the reasonableness of this approach to experimentally determining adhesion energy that could provide a benchmark parameter to theorists.

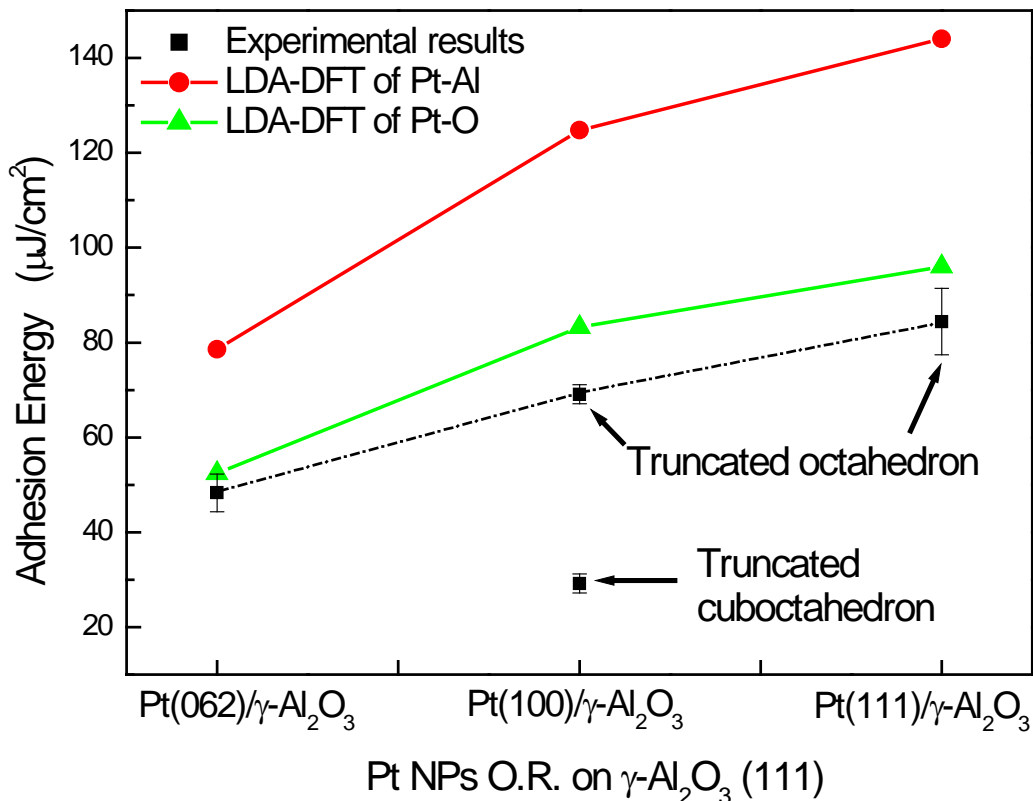


Figure 5.9 Experimental results vs LDA-DFT calculated adsorption energies for Pt NPs on γ - Al_2O_3 with Al, O and sites [74,122].

However, it should be noted that the approach presented above assumed no strain, no adsorbates and zero temperature for comparison to the published theoretical calculations. Adsorbates have dramatic impact on surface facets and nanoparticle morphologies [60,123,124].

Elevated temperature will impact strain [125] within the nanoparticle as well as at the interface [126,127]. Hence, such effects must be considered carefully in the above analysis especially under operational conditions of the catalysts.

5.5 CONCLUSIONS

In summary, the Pt/ γ -Al₂O₃ model catalyst was prepared and characterized by cross-sectional HRTEM. Some of the NPs were noted to be faceted. These faceted Pt NPs on γ -Al₂O₃ are generally a truncated octahedron shape with {100} and {111} facets predominantly. A truncated cuboctahedron shape of Pt NPs with {110} facet reconstruction was also observed. Both faceted Pt NPs had a small lattice mismatch with respect to the oxide support. In addition, high-index plane Pt NPs with {062} and {331} facet were also observed where an epitaxy along the Pt/ γ -Al₂O₃(111) interface was noted.

To estimate the adhesion energy of Pt NPs on γ -Al₂O₃, Wulff-Kaischew theorem was applied. Based on the Wulff-Kaischew formulation, the adhesion energy was reasonably consistent with the published theoretical results. The interfacial adhesion energy of the Pt facet also followed the same trend as theoretically predicted, where Pt{062} < Pt {100} < Pt{111}. These numbers are based on assuming no adsorbates, zero temperature and no strain. These parameters need to be carefully considered in applying this approach to real catalytic conditions; however, the general agreement between this approach and theoretical calculations indicate the validity of this approach in experimentally estimating the interface adhesion energy, that could be used to guide theorists towards predictive and rational heterogeneous catalyst design.

6.0 ELECTRON ENERGY LOSS SPECTROSCOPY STUDY OF PLATINUM NANOPARTICLES ON γ -ALUMINA SUPPORT

The electronic states of the interface between catalyst nanoparticles and their support play an important role in the electronic landscape of the supported nanoparticle that influence the catalytic performance, catalyst migration behavior or agglomeration, and anchoring sites [41,128–135].

Modulation of the ionization edge can be related to the band structure of the solid in which scattering occurs. By using one-electron approximation, the excitation of an inner-shell electron could be assumed to have no effect on the other atomic electrons [136]. Therefore, the single scattering intensity $J_k(E)$ is then proportional to a product of the density of final state $N(E)$ and an atomic transition matrix $M(E)$:

$$J_k(E) \propto |M(E)|^2 N(E) \quad (6.1)$$

where $M(E)$ represents the overall shape of the spectrum which is determined by the atomic physics, and $N(E)$ depends on the crystallographic environment of the excited atom. In the first principle approximation, $M(E)$ can be assume to be a slowly varying function of energy loss E , so the variation in the single-scattering inner-shell intensity $J_k(E)$ should reflect the density of states (DOS) above the Fermi level [137].

Thus, electron energy loss spectroscopy was applied to study the electronic state of Pt nanoparticle dispersed on γ -Al₂O₃ single crystal at/across their interface using cross-sectional scanning transmission electron microscopy.

6.1 ELECTRONIC STRUCTURE OF PLATINUM/ γ -ALUMINA INTERFACE

Using EELS to resolve the unoccupied electronic density of states by site and atomic species will give a better understanding of the electronic structure at the Pt/ γ -Al₂O₃ interface. In addition, these EELS measurements provide localized information about both chemical composition and electronic properties. Aberration correction scanning transmission electron microscope (STEM) combined with electron energy loss spectroscopy (EELS) allows atomic-resolution Z-contrast imaging with simultaneous spectral information.

6.2 EXPERIMENTAL PROCEDURES

EELS spectra were recorded across the interface by scanning the 0.1 nm beam across the Pt NP, through the interface and into the substrate. The creation of thin films of single crystal γ -Al₂O₃ (111) support is oxidizing NiAl(110) at 850°C in dry air where the obtained oxide RMS roughness is around ~10 nm. The TEM sample was thinned down to sub 10 nm. The thickness of the sample could be estimated by the particle distance of Pt NPs as observed in the Pt/C reference system. The prepared cross-sectional transmission electron microscopy specimens were oriented and cut along the NiAl substrate [110] zone axis. Based on the revealed Nishiyama-Wasserman orientation relation, the γ -Al₂O₃ model support was aligned to its [211] zone axis accordingly. Thus, the Pt/ γ -Al₂O₃ interface could be placed parallel to the electron beam for characterization profile from the indicated oxide support shows a γ -Al₂O₃ (440) spacing which confirms the single crystal γ -Al₂O₃ (111) surface plane.

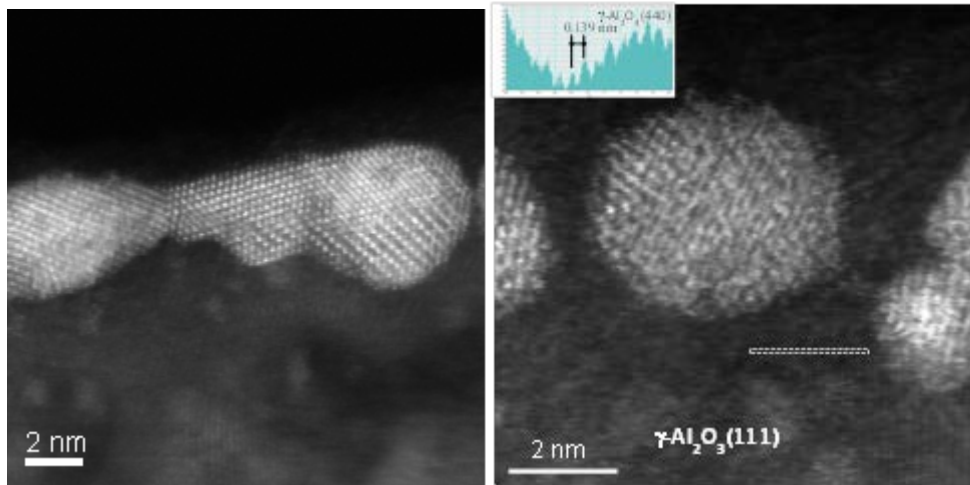


Figure 6.1 HAADF images Pt NPs directly supported on γ -Al₂O₃. Due to γ -Al₂O₃ is a low Z oxide, the contrast contributed by γ -Al₂O₃ is relatively low compared with Pt NPs.

Electron energy loss spectroscopy gives information on the site and symmetry from the projected unoccupied density of states near the Fermi level. Two edges are studied in detail: the O K edge within 510~600 eV and the Al $L_{2,3}$ edge within 70~120 eV. Careful inspection of the spectra over time up to 3 s shows no changes in the EELS spectra at exposure times. This is taken as an indication that no significant beam damage effects occur during the acquisition of the EELS spectra.

6.3 RESULTS AND DISCUSSION

In Figure 6.1, high-angle annular dark field (HAADF) images show contact between the Pt particles and the γ -Al₂O₃ support. The γ -Al₂O₃(111) thin film grown on NiAl (011) alloy follows the classical Nishiyama-Wasserman orientation relation: NiAl[110]|| γ -Al₂O₃[211] and NiAl[100]|| γ -Al₂O₃[110]. Therefore, the substrate NiAl[110] zone axis was used as the reference orientation to tilt the γ -Al₂O₃ thin film into the desired [211] axis.

We collected the oxygen K edge, Al $L_{2,3}$ edge and Pt M₄ edge electron energy-loss spectra. EELS line scan were conducted across the Pt/ γ -Al₂O₃ interface and in the vicinity of the interface by scanning the beam from the Pt particle to the γ -Al₂O₃ support at 40 different locations. Background subtraction was performed with a power law fitting over a 120 eV window at 50 eV prior to the onset of the edge [116]. Figure 6.2 shows a set of EELS spectra of the oxygen K edge line scan across the Pt/ γ -Al₂O₃ interface. The spectra were recorded at 0.3eV energy resolution with 2s exposure per point to minimize radiation damage. The EELS spectra were recorded simultaneously with the HAADF signal. Because the interface is viewed in projection, any interfacial roughness in the direction of the thickness results in a broadening of the interfacial signal. In study of the O K edge EELS spectra, distinguishable features were observed at the Pt/ γ -Al₂O₃ interfaces. A well-pronounced O K edge prepeak before the bulk edge onset was observed at the Pt/ γ -Al₂O₃ interface at different locations, as shown in Figure 6.2, 6.3 and 6.7. Direct comparisons of the O K spectra with prepeak collected at the Pt/ γ -Al₂O₃

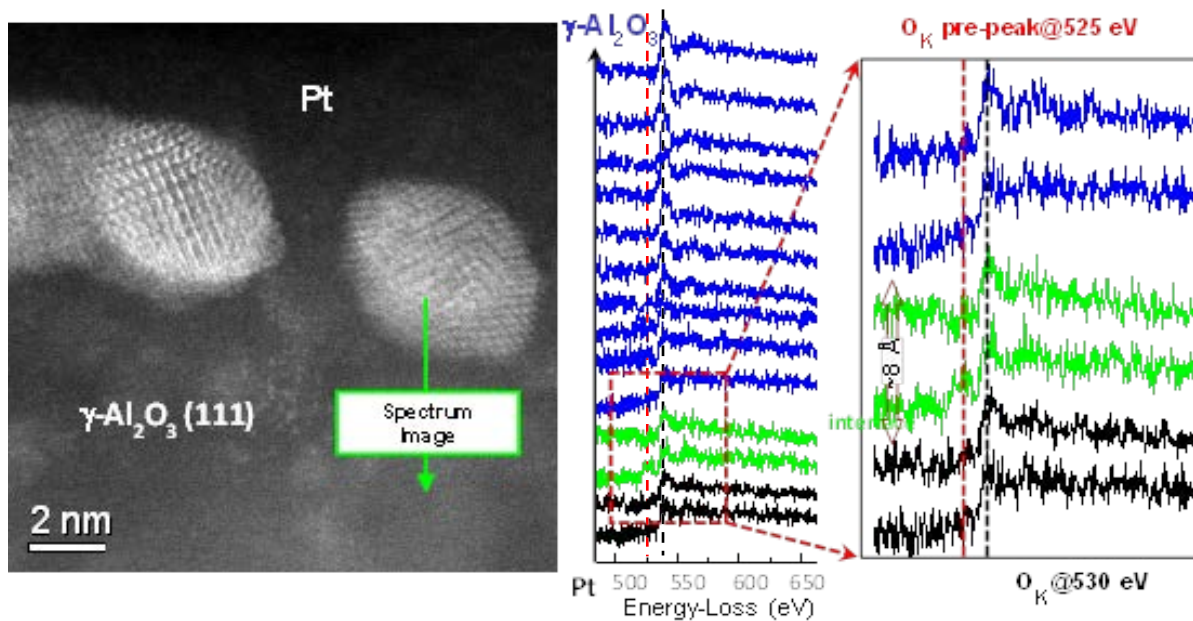


Figure 6.2 The HAADF image of Pt particles with corresponding EELS spectra. The arrow indicates the position where EELS line scan spectrum was taken. O K edge EELS line scan spectra were recorded point by point across the Pt/ γ -Al₂O₃ interface with a step of 4.2Å.

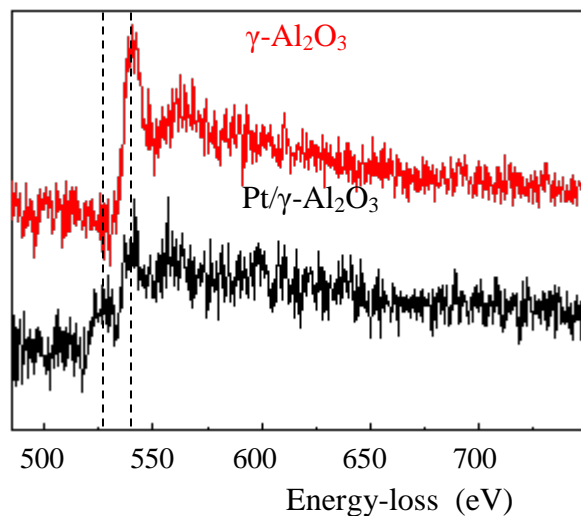


Figure 6.3 O K edge EELS line scan spectra obtained from the Pt/ γ -Al₂O₃ interface and γ -Al₂O₃ support.

interface and without prepeak at the γ -Al₂O₃ support are shown in Figure 6.3. The published standard O K edge EELS spectrum from α -Al₂O₃ was shown in Figure 6.4 for comparison [138].

The O K edge prepeak appearing as the first extended-fine-structure peak before the bulk near edge spectrum was found in 6 out of 40 EELS scans at the interfacial regions. In this case, the change of the O K edge suggests a modulated DOS at the Pt/ γ -Al₂O₃ interface, and the appearance of O K edge prepeak implied a shift of Fermi level.

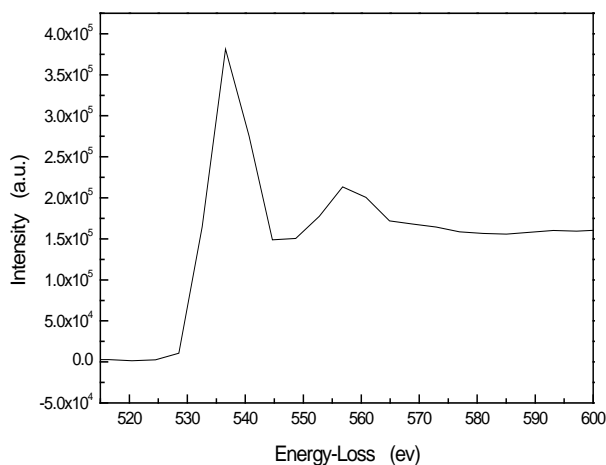


Figure 6.4 Standard O K edge EELS spectrum from α -Al₂O₃ acquired from EELS ATLAS, K edge start 530 eV, peak at 536 eV [138].

Moreover, the observed EELS spectra of O K edge were also compared to data from standard reference materials to better interpret the electronic structure of Pt/ γ -Al₂O₃ interface. In standard α -Al₂O₃ oxygen EELS spectra from EELS ATLAS [138], it typically shows only a single edge and have been thoroughly studied where the O K edge typically has a step-like, abrupt onset at 532 eV and is strong in intensity and rich in features indicative of the chemical

environment, Figure 6.4. The comparison of the O K spectrum from various interfaces shows a similar shape and height which match closely to the Al₂O₃ spectrum (O K edge at 530 eV). The prominent difference between the two regions is the feature preceding the oxygen K edge. The actual shape of EELS should be compared to theoretical calculations or compared with other known compounds via the fingerprinting method [136]. The appearance of the prepeak at the O K peak in the interface was located at 525.5 eV which is different from the standard O K edge spectrum as shown in Figure 6.3 and Figure 6.4. Defects in γ -Al₂O₃ near the interface could lead to altered electronic states at the interfacial region.

As shown in Figure 6.5, the oxygen K edge EELS scans was taken from both the non-symmetrical shape Pt particle (interface 1) and a more symmetrical shape Pt particle (interface 2). For the oxygen K edge spectrum with a prominent prepeak at 525.5 eV collected at interface 1 and the O K edge EELS spectrum obtained from the adjacent Pt particle (interface 2) without the presence of oxygen prepeak may be due to different orientations of the Pt NP on the alumina, since the Pt NPs are randomly orientated on the oxide support. The Al and Pt spectra obtained from both interfaces resemble the Al L_{2,3} and Pt M₄ spectrum from α -Al₂O₃ and metallic Pt [138].

Meanwhile, it was also important to consider that the changes of DOS observed at Pt/ γ -Al₂O₃ interface might also be due to other effects, such as the electron beam radiation damage to the specimen [139]. In former EELS study of MgAl₂O₄ by J. Nan et al. [139], a similar O K edge prepeak had often been observed which was interpreted due to beam radiation damage, rather than an intrinsic feature of the magnesium spinel. Therefore, beam damage experiments were conducted with a longer exposure time (above 30 sec) and a damaged area in the γ -Al₂O₃

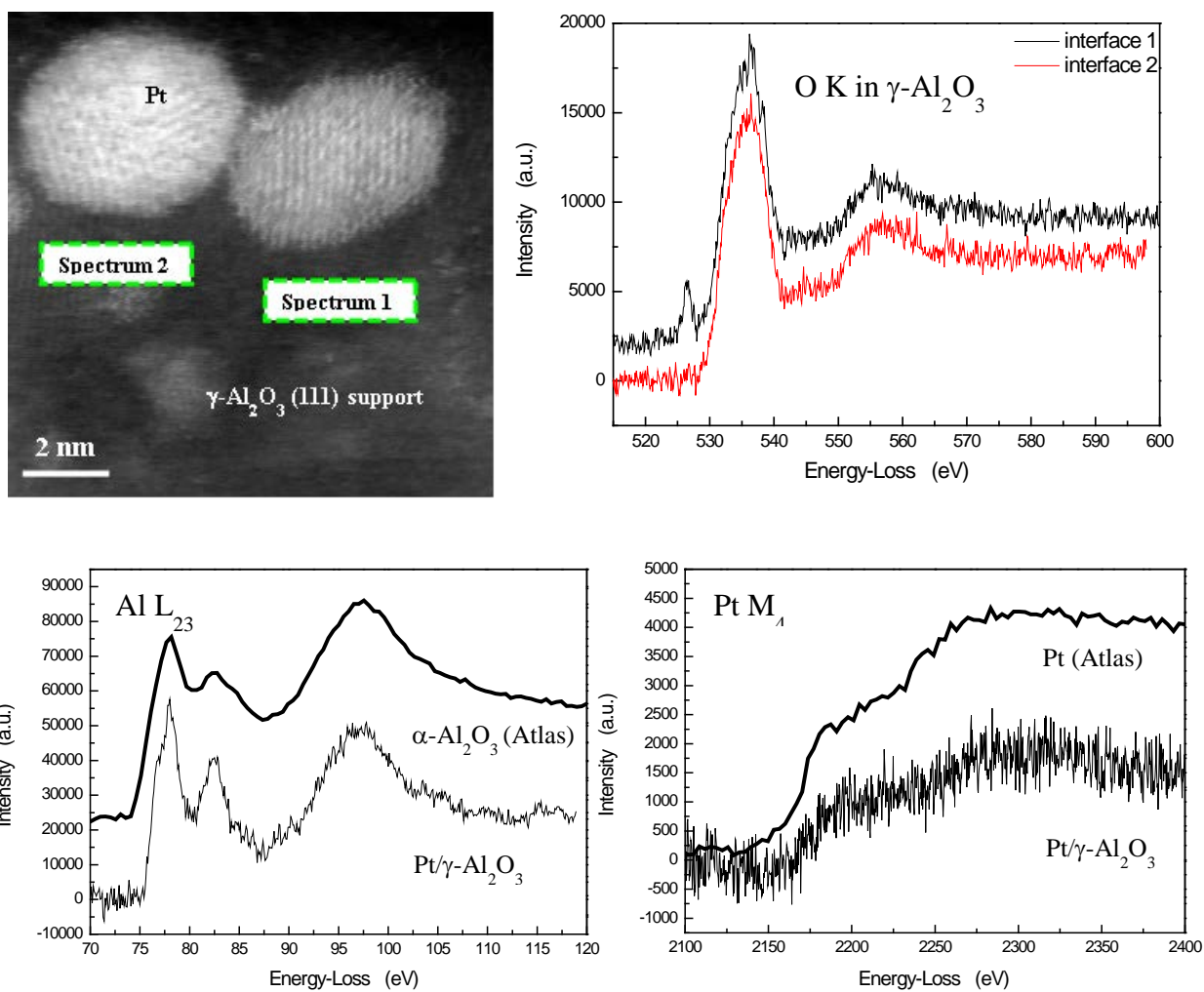


Figure 6.5 The measured EELS spectra from the Pt/ $\gamma\text{-Al}_2\text{O}_3$ interface indicated representative Pt M_4 and Al $L_{2,3}$ peaks. O K prepeak observed at various Pt/ $\gamma\text{-Al}_2\text{O}_3$ interfaces at energy edge 525.5 eV is compared with the typical O K spectrum collected at non-symmetrical (interface1) and more symmetrical (interface 2) Pt particle and $\gamma\text{-Al}_2\text{O}_3$ interfaces. The oxygen K edge peak spectrum as well as the Al $L_{2,3}$ and Pt M_4 edge peak spectrum were collected using a 0.1 eV energy resolution with an exposure time of 3 sec from various interfacial regions.

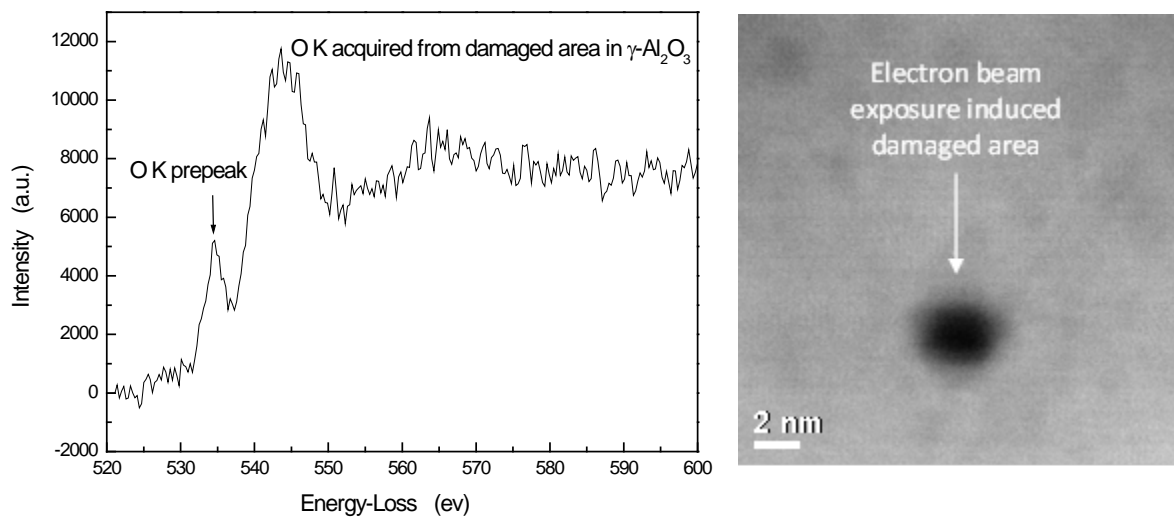


Figure 6.6 EELS of O K edge (Right) acquired from beam damaged area under STEM (Left).

substrate was noted, Figure 6.6. It was seen that a strong O K pre-edge peak appeared at this damaged area. Similar beam radiation induced damaged area were conducted, and it should be noted that the O K prepeak was only observed occasionally at some of the damaged region which indicated a non-uniformity structure of γ -Al₂O₃ support. In comparison of the O K prepeak acquired from beam damaged area and specific interfacial region where prepeak was observed, it was found the relative peak difference are similar (~9.5 eV) between the O K prepeak and the O K peak, which implied that the O K prepeak from the interfacial region of γ -Al₂O₃ support might be also due to beam radiation. Based on this consideration, to reduce beam damage while collecting the EELS spectrum at the Pt/ γ -Al₂O₃ interface, a sub pixel 16x16 scan over a box region a sub pixel 16x16 scan over a box (see HAADF image with the outlined box in Figure 6.7) was applied to minimize beam damage and collect more interfacial signal.

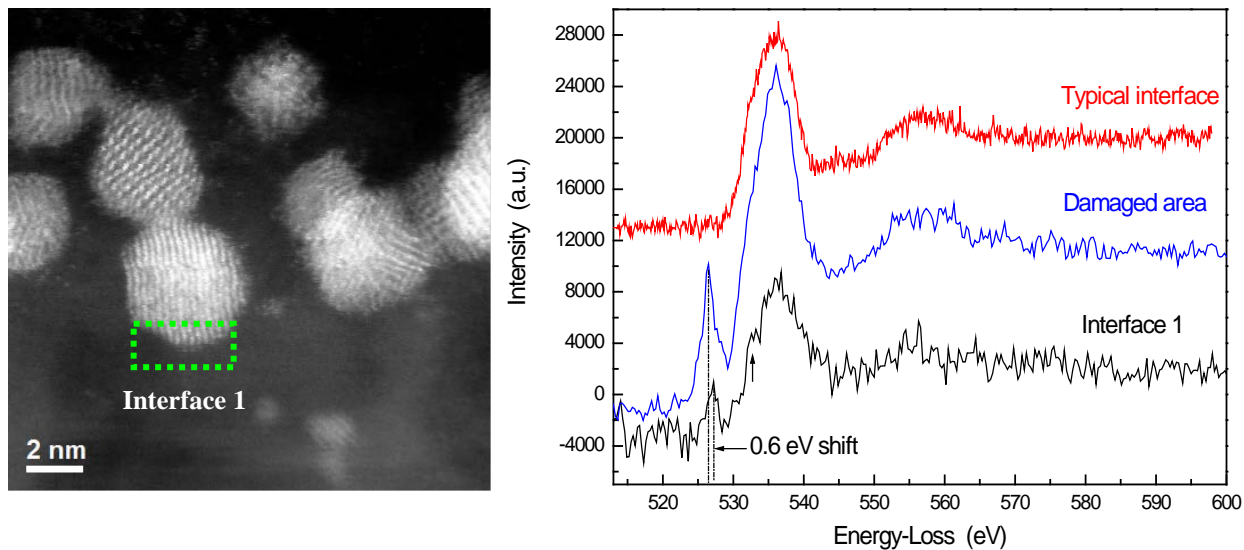


Figure 6.7 Comparison of O K edge EELS acquired from beam damaged area and interfacial regions under STEM.

Comparing the feature of O K edge prepeak obtained from the beam damaged area to the specific (prepeak observed) Pt/ γ -Al₂O₃ interface regions (interface 1), Figure 6.7, it indicated that the beam damaged induced prepeak has a 0.6 eV energy shift to its lower level. For Cold field emission gun STEM, its zero loss peak gives an energy spread of 0.4 eV, and convolution with the 0.3 energy dispersion gives an 0.4 eV energy resolution. Therefore, the 0.6 eV difference of the prepeak between the radiation damaged region of the oxide and the interface is significant; the prepeak is due to the interface rather than due to radiation damage of the oxide. In addition, the O K main peak at the Pt/ γ -Al₂O₃ interface showed a shoulder feature (marked by the arrows) comparing with the beam damaged EELS spectrum, which reflects a change of chemical environment at these interfaces, Figure 6.7. The O K prepeak peak indicates changing in the bonding or DOS of the O atom at specific interfaces, as shown Figure 6.7. The prepeak indicates a shift in the Fermi level, and the changes in the O K edge peak indicates a change in the

(unoccupied) density of states which could be due to changes in chemical bonding. Based on this analysis, the O K prepeak in the interface is due to the changed electronic environment at interface since it is not identical to the prepeak position/feature from the damaged oxide.

It should also be noted that the arrangement of atoms and defects may effect where the Pt NPs are pinned and thus will affect the electronic structure of the interface. For example, J. Kwak et al. have shown that the unsaturated Al^{3+} pentacoordinated sites are the dominant sites for Pt anchoring [1]. Former findings by J. Kwak et al., [41,132] S. Pennycook et al. [38] and N. Nilius et al. [140] proposed different types of $\gamma\text{-Al}_2\text{O}_3$ surface, such as defective sites or coordinately unsaturated sites, that may be preferred anchoring sites. Also, the surface defects of $\gamma\text{-Al}_2\text{O}_3$ have also been proposed to play an important role in pinning the NPs [2-4]. However, further density-functional theory simulations as well as further experiments are necessary to understand physical underpinning of the O K edge prepeak and the nature of the double O K peak.

6.4 CONCLUSIONS

The present study demonstrates the changes of density of states at the Pt/ γ -Al₂O₃ interface. The appearance of O K edge prepeak at metal/oxide interface located at 525.5 eV is different from the standard O K edge spectrum and suggests a shift in the Fermi level and the O K double-peak indicated a change of the density of states. More careful experiments will be necessary to statistically quantify the interfacial EELS as function of the Pt NP shape, size and relative orientation to the oxide. Further theoretical simulation is necessary to elucidate the physical underpinning of the interfacial EELS spectra.

7.0 SUMMARY AND FUTURE WORK

This thesis provides a thorough study on formation, characterization and interpretation of Pt/ γ - Al_2O_3 model catalyst system. Fundamental understanding on model catalyst support γ - Al_2O_3 single crystal formation on NiAl(110) alloy and Pt NPs interactions to the γ - Al_2O_3 support has been obtained:

(1). The creation of single crystal γ - Al_2O_3 thin films is essential for the general model catalyst study and serves a base for our model system. The formation of γ - Al_2O_3 as a support for the Pt/ γ - Al_2O_3 model catalyst was systematically investigated through oxidation of β -NiAl(110) substrate. β -NiAl(110) was oxidized in air for 1 to 2 hours within the temperature range of 650-950°C, and the structure and morphology of the oxide films were characterized by cross-sectional transmission electron microscopy (TEM), AFM and XRD methods. Only a metastable phase of aluminum oxide, γ - Al_2O_3 , thin film was formed. The epitaxial relationship between NiAl and γ - Al_2O_3 as well as the surface roughness depends on the oxidation temperature. Nishiyama–Wassermann (NW) orientation relation (O.R.) between β -NiAl and γ - Al_2O_3 was noted at the oxidation temperature 850°C and the Kurdjumov–Sachs (KS) orientation relation (O.R.) was observed at 650°C. The temperature dependent changes of the epitaxial relationship of γ - Al_2O_3 to the NiAl substrate was caused by the lattice mismatch induced strain energy during the oxide growth. Short time oxidation at $T = 750^\circ\text{C}$ created γ' phase precipitates between the

NiAl substrate and γ -Al₂O₃ film. Oxidation at the higher temperature of 950°C resulted in textured polycrystalline γ -Al₂O₃ films. The desired single crystal epitaxial γ -Al₂O₃ film formed through the oxidation at T = 850°C in air.

(2). A model catalyst system of Pt/ γ -Al₂O₃ was prepared and studied by cross-sectional HREM and STEM investigate the morphology of the Pt/ γ -Al₂O₃ and the interfacial electronic structure. From the HRTEM studies, the faceted truncated octahedron shape Pt NPs on γ -Al₂O₃ was observed and its 3-dimensional shape was inferred. From measurements of the facets' and nanoparticles shape, the Wulff-Kaischew theorem was applied to obtain the adhesion energy of Pt NPs. The adhesion energies were obtained for various facets of the Pt NPs on the support. The experimentally obtained adhesion energy was compared with DFT calculations where a reasonable agreement was noted. This generalized method is expected to provide interfacial energies that can be compared to theoretical models for fundamental understanding of the particle-support relationship.

(3). The EELS study of the Pt/ γ -Al₂O₃ interface indicates changes to the density of states and possible shift of the Fermi level. In particular, an O K prepeak was observed in a few of the interfaces and a double O K peak or O K peak and shoulder was observed in some other interfacial EELS spectra. The Al L_{2,3} edge and the Pt M₄ edge from the interface did not change from the bulk oxide and metal spectra, respectively. The differences in the EELS spectra could be due to different orientations of the Pt NPs on the alumina, since the Pt NPs were randomly oriented. More careful experiments will be necessary to elucidate the relationship between atomic and electronic structure and the interface. Further theoretical simulation is necessary to elucidate the physical underpinnings of the interfacial EELS spectra from the Pt/ γ -Al₂O₃.

The present study exemplifies the exciting potential of studying Pt/ γ -Al₂O₃ model catalyst system for fundamental understanding of this important heterogeneous catalysts system needed for rational design. Furthermore, γ -Al₂O₃ is an oft-used catalyst support system for other technical applications. Hence other model metal/ γ -Al₂O₃ catalyst systems can also be studied. More work is still needed to improve the quality of the formation and characterization of the system. Future work includes:

(1). Better TEM sample preparation method will significantly improve the HRTEM and STEM results to obtain the interfacial atomic and electronic structure of Pt/ γ -Al₂O₃, which may for example reveal how interfacial defects affect the catalyst nanoparticle pinning and catalytic performance.

(2). Improve the γ -Al₂O₃ support surface roughness while maintaining its single crystalline structure to obtain an atomically sharp Pt/ γ -Al₂O₃ interface.

(3). STEM and EELS studies of the Pt/ γ -Al₂O₃ interface coupled with theoretical simulations will clarify the findings of oxygen electronic states changes at the interface region where C_s- corrected TEM/STEM could assist to achieve better atomic resolution and the electronic structure of the Pt/ γ -Al₂O₃ interface. In addition, theoretical simulations will resolve the the physical underpinning of the Pt-O chemical bonding and the electronic structure of the Pt/ γ -Al₂O₃.

(4). The effect of the catalysts environment, such as heat and gas, on the morphology, interfacial structure and electronic structure will be studied to provide key insights into activity and selectivity.

(5) Other metal catalyst nanoparticles, such as Pd, on γ -Al₂O₃ will also be studied, since γ -Al₂O₃ is a commonly used catalyst support for a wide variety of metal nanoparticle catalysts.

APPENDIX I

WULFF-KAISCHEW THEOREM OF PT NPS SHAPE ON MODEL γ -Al₂O₃ SUPPORT

In general, for sessile drops, the adhesion forces between a liquid and solid cause a liquid drop to spread across the surface. The fundamental parameter in thermodynamics that is used to evaluate the shape of a liquid drop in contact with an inert substrate is shown in Figure AI.1a. The equilibrium value of the contact angle θ is determined by the balance of the energies of the interfaces between the liquid (*l*), solid (*s*) and vapor (*v*) phases and expressed by the Young's (or Young-Dupré) equation:

$$\gamma_{vl} \cos \theta + \gamma_{ls} = \gamma_{sv} \quad (\text{AI.1})$$

W_{adh} is the work of adhesion or adhesion energy, and is given by the Dupré equation:

$$W_{\text{adh}} = (\gamma_{lv} + \gamma_{sv}) - \gamma_{ls}$$

In fact, for the case of solid crystal growth, it has been long recognized that the shape and surface structure is thermodynamically dependent on the specific surface energy of the crystal facets. To determine the equilibrium shape of the crystalline particles for a given volume, Wulff [71] presented the construction of solid crystals to obtain certain preferred crystal planes with a minimum Gibbs free energy (ΔF) of the surface,

$$\Delta F = \oint \gamma(n) dS \quad (\text{AI.2})$$

where the specific surface free energy γ is a function of the orientation of the unit outward normal n at each surface point. With cusped minima in certain directions corresponding to surfaces of particularly simple structure, a crystal body in a two dimensional cross-section will be the outer curve in Figure AI.1b. At each point of this polar plot construct a plane perpendicular to the radius vector at that point. Then the volume which can be reached from the origin without crossing any of the planes is geometrically similar to the ultimate equilibrium shape for the crystal, i.e., the shape minimizes the equation (AI.2) for a fixed volume.

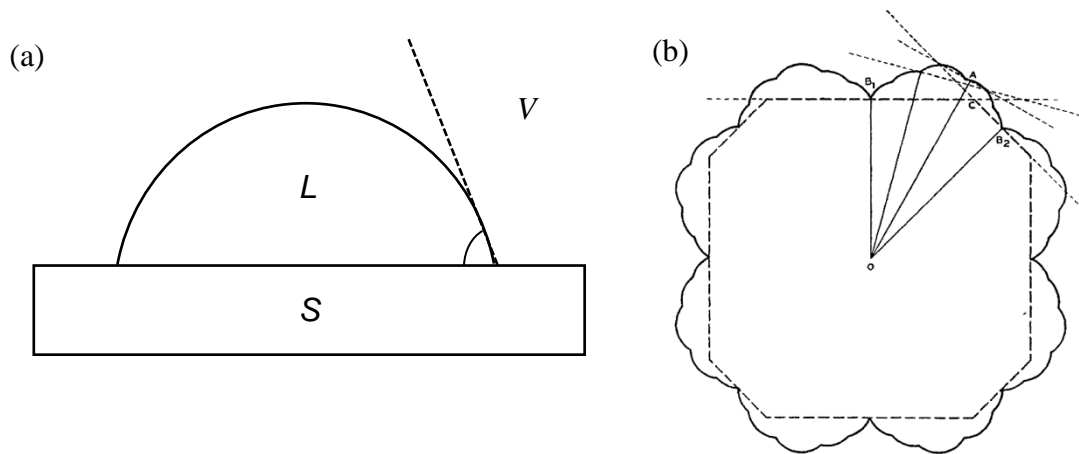


Figure AI.1 (a). Illustration of contact angle of a liquid drop L on a solid substrate S with partially wetting angle θ . (b). Schematic diagram illustrating the Wulff construction yields the equilibrium shape polyhedron of crystal (inner dashed line) which are normal to the radius vectors (outer light dashed line), with corresponding polar plot of surface free energy (solid line) [73].

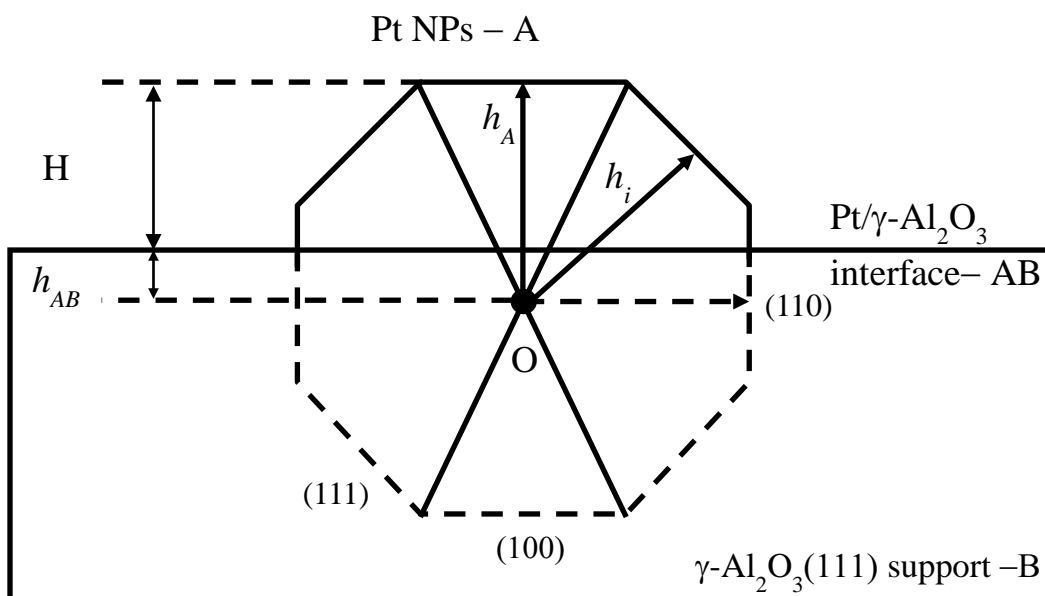


Figure AI.2 Schematic diagram of reconstructed ES Pt NP on $\gamma\text{-Al}_2\text{O}_3$ support. h_i and h_{AB} are the normal distances from the Wulff point O to the facet i , and the interface AB, respectively. $h_{AB} < 0$ implies that the Wulff point is located within the support.

The equilibrium polyhedron shape was demonstrated to be [71,77],

$$\lambda = \frac{\gamma_i}{h_i} \quad (\text{AI.3})$$

where γ_i and h_i are the surface energy and the central distance of the Wulff point O to the index facet surface i , and λ is a constant.

As stated in Wulff theorem, the absence of support and interfacial energy could be the limit of its application to the model catalyst system. By clearly identifying the shape and structural relation of Pt/ $\gamma\text{-Al}_2\text{O}_3$ in cross-sectional view, Wulff-Kaischew theorem [28,71,73,76,121] is proposed to include the interface energy induced particle shape

modification. A schematic diagram shown in Figure AI.2 depicts the side view of Pt NP (A) sits on γ -Al₂O₃ (B) surface. The total Gibbs free energy change of forming Pt/ γ -Al₂O₃ system, ΔF , is composed of three terms, the chemical formation energy (ΔF_1), the surface energy and interfacial energy (ΔF_2), and the elastic energy stored by the system (ΔF_3), as stated below,

$$\Delta F = \Delta F_1 + \Delta F_2 + \Delta F_3 \quad (\text{AI.4})$$

$$(1). \Delta F_1 = -\Delta\mu V$$

ΔF_1 is the chemical work to form the crystal, $\Delta\mu$ is the supersaturation work function per unit volume, i.e. $\Delta\mu = \frac{kT}{v} \ln\left(\frac{P}{P_\infty}\right)$, where v is the volume of the atom A, P_∞ is the saturation pressure

and P is the vapor pressure. V is the volume of molecule in NP. The volume V of a polyhedral can be considered as pyramids of heights h_i with base area S_i , $V = \frac{1}{3} \sum_{i=1}^n h_i S_i$

For the truncated polyhedron the total volume is

$$V = \frac{1}{3} \sum_{i \neq AB} h_i S_i + \frac{1}{3} h_{AB} S_{AB}$$

$$(2). \Delta F_2 = \sum_{i \neq AB} (\gamma_i S_i) + (\gamma_{AB} - \gamma_B) S_{AB}$$

ΔF_2 is the surface and interface energy. For a crystal that has i facets of area S_i , the surface energy is expressed as $\gamma \cdot S_i$. h_i and h_{AB} are the normal distances from Wulff point O to the surfaces i and the interface AB (Figure AI.2),

The adhesion energy β can then be introduced to equation (1) by Dupre's equation,

$$\gamma_{AB} = \gamma_A + \gamma_B - \beta$$

Which reflects the bonding properties of the metal nanoparticles to the support oxide.

$$\text{Thus, } \gamma_{AB} - \gamma_B = \gamma_A - \beta$$

This equation is used in our derivation.

$$(3). \Delta F_3 = \varepsilon_0 m^2 VR$$

ΔF_3 is the elastic energy store by the relaxed system. For a strained crystal the elastic energy before relation is $\varepsilon_0 m^2 V$. Because of the energy released by lattice relaxation, the elastic energy stored by system is $\varepsilon_0 m^2 VR$, where $0 < R < 1$ is a relaxation energy factor that depends in a complex way upon the crystal shape. Nevertheless its limiting behavior must be $R=0$ for a completely relaxed system and $R=1$ for a non-relaxed crystal. For epitaxial equilibrium shape (ES) NPs formation, $m=0$ for $\Delta F_3 = 0$,

In the Wulff-Kaischew theorem, the elastic energy is disregarded at the conditon of trivial lattice misfit, $m \rightarrow 0$, or negligible factor, $R \rightarrow 0$. The equilibrium thus can be obtained by taking the first orider derivative of equation (3) and setting it to be zero. Therefore, the ES is obtained at the minimum system energy, i.e. $d(\Delta F) = 0$.

$$d\Delta F_1 = -\Delta\mu dV = -\frac{\Delta\mu}{3} \left[\sum_{i \neq AB}^n (h_i dS_i) + h_{AB} dS_{AB} \right]$$

$$d\Delta F_2 = \sum_{i \neq AB}^n (\gamma_i dS_i) + (\gamma_{AB} - \gamma_B) dS_{AB}$$

$$\begin{aligned}
d\Delta F &= d\Delta F_1 + d\Delta F_2 \\
&= -\frac{\Delta\mu}{3} \left[\sum_{i \neq AB}^{\infty} (h_i dS_i) + h_{AB} dS_{AB} \right] + \sum_{i \neq AB}^{\infty} (\gamma_i dS_i) + (\gamma_A - \beta) dS_{AB} \\
&= \sum_{i \neq AB}^{\infty} \left(\left(-\frac{\Delta\mu}{3} h_i + \gamma_i \right) dS_i \right) + \left[-\frac{\Delta\mu}{3} h_{AB} + (\gamma_A - \beta) \right] dS_{AB} \\
&= 0
\end{aligned}$$

Equilibrium shape was obtained when all the partial derivatives are zero simultaneously,

$$-\frac{\Delta\mu}{3} h_i + \gamma_i = 0 \quad \rightarrow \quad \frac{\Delta\mu}{3} = \frac{\gamma_i}{h_i} = \lambda \text{ (constant)} \quad \text{Similar to Wulff theorem}$$

$$-\frac{\Delta\mu}{3} h_{AB} + (\gamma_A - \beta) = 0 \quad \rightarrow \quad \frac{\Delta\mu}{3} = \frac{(\gamma_A - \beta)}{h_{AB}} = \lambda \text{ (constant)} \quad \text{Kaischew theorem}$$

$$\frac{(\gamma_A - \beta)}{h_{AB}} = \frac{\gamma_i}{h_i} \quad \text{Wulff – Kaischew theorem} \quad (\text{AI.5})$$

$$\gamma_{AB} = \gamma_A + \gamma_B - \beta \quad \text{Dupre's equation} \quad (\text{AI.6})$$

If $\gamma_A < \beta$, $h_{AB} < 0$, i.e. the particle is dewetting on support, the Wulff point O is below the interface AB with less surface area exposed which is presented in Figure AI.2. For increasing adhesion energy, β , the Pt NP equilibrium shape becomes more truncated. The adhesion energy β (equation AI.5) and interfacial energy γ_{AB} (equation AI.6) could be quantitatively solved for based on the Wulff-Kaischew theorem [28,29]. Evaluation of the adhesion energy and interfacial energy of equilibrium shape Pt NPs on γ -Al₂O₃ is feasible using literature values for surface energies and interfacial energy of Pt and γ -Al₂O₃[39,40,112,119,120,141,142] ..

APPENDIX II

A DIFFUSION ANALYSIS OF TRANSIENT SUBSURFACE PHASE FORMATION DURING β -NiAl OXIDATION

AII.1 Introduction

The intermetallic alloy β -NiAl is an excellent alumina-scale former with good thermo-mechanical properties; thus it has been extensively used in a wide range of engineering applications [54,143,144]. Among the various metastable polymorphs of alumina scale that can form on NiAl, γ -Al₂O₃ is one of the most important, which has been extensively used in heterogeneous catalysis as supports/adsorbents for noble metals, protective coatings, soft abrasives and microelectronic devices [10,45,52,59]. Numerous oxidation studies of NiAl-based systems under various conditions have been conducted from the atomic through to the micron scale to fundamentally understand the surface oxidation process as well as the alloy/oxide interfacial relations [43,94,145,146]. The performance and stability of a thermally grown oxide scale are highly dependent on the diffusion between the oxide layer and its substrate, together with any other accompanying chemical and physical processes. During selective-oxide formation on a binary alloy, a depletion region of the component being oxidized can form at the alloy subsurface, potentially leading to the formation of an intermediate phase [145,147,148]. Our

previous study of NiAl oxidation to grow γ -Al₂O₃ (111) at 750 °C found the subsurface formation of the intermetallic compound γ' -Ni₃Al [145]. In this work, a quantitative diffusional analysis is presented to better understand the subsurface γ' formation process in the NiAl system during oxidation.

AII.2 Observations of subsurface phase formation during NiAl oxidation

Equiatomic single-crystal NiAl (110) (obtained from General Electric and fabricated by the Bridgman technique with typical C and O contents of ~6 ppm wt. each) was oxidized at 650°C to 850°C for up to 2 h in dry air to form a single-crystal γ -Al₂O₃ (111) thin film. It was previously reported by our group that γ' -Ni₃Al forms in the vicinity of the NiAl/ γ -Al₂O₃ interface

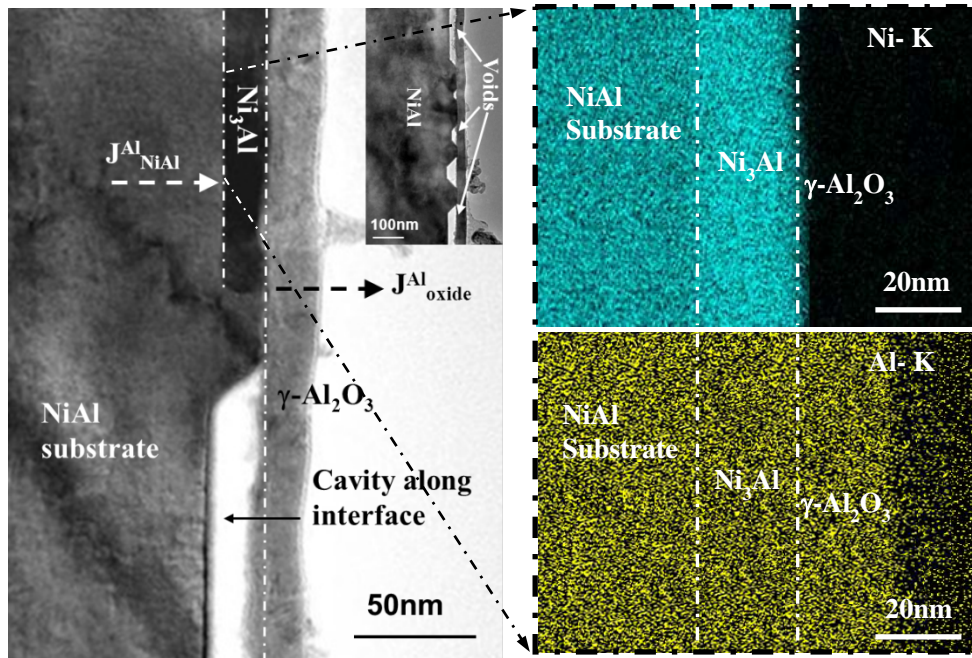


Figure AII.1 Cross-sectional TEM image of 750°C 1 h oxidized NiAl(110): (a). Ni₃Al phase formation with a large cavity portion at the interface, (b) Ni-K edge EDS mapping, (c) Al-K edge EDS mapping [9].

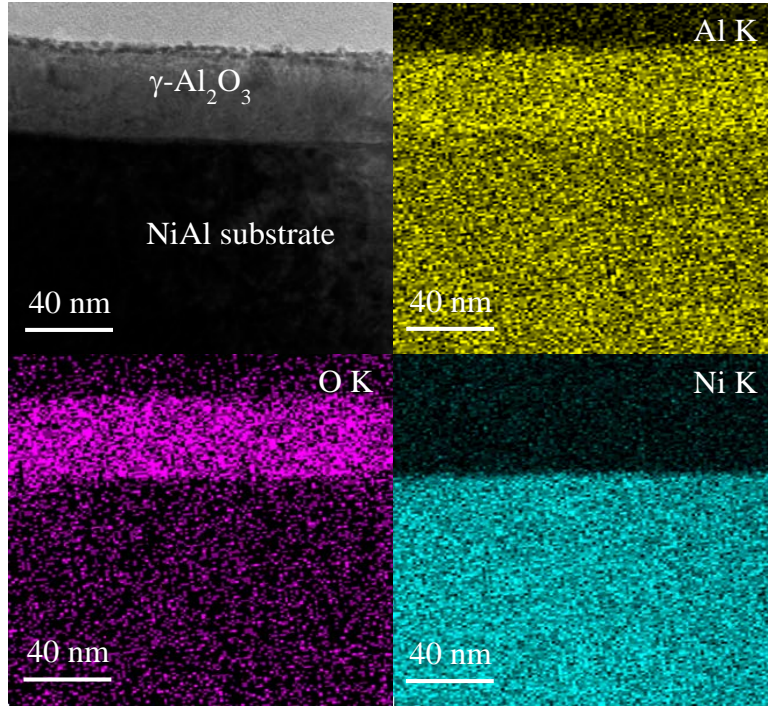


Figure AII.2 Cross-sectional TEM image of 750°C 2 h oxidized NiAl/ γ -Al₂O₃ interface with corresponding EDS elemental mapping confirmed no phase formation.

at 750°C oxidation for 1 h, as shown in Figure AII.1 [145]. Moreover, the formation of γ' coincided with significant void formation. To further study the γ' formation process, cross-sectional TEM samples were prepared using a Seiko Instruments SMI3050SE dual-beam focused ion beam on specimens oxidized at 750°C for 2 h. As shown in Figure AII.2, the resulting bright-field TEM image indicated a uniform and continuous 40 nm oxide film had formed, with no indication of subsurface γ' or significant void formation. The exclusive formation of a continuous Al₂O₃ scale was further confirmed by dispersive spectroscopy (EDS) mapping, as shown by the Ni-K edge, O-K edge and Al-K edge energy maps in Figure AII.2. At a higher oxidation temperature of 850°C or a lower temperature of 650°C, no subsurface γ' formation was found during NiAl (110) oxidation [145].

AII.3 Analysis

As presented in the previous section, when a binary intermetallic alloy forms an exclusive oxide scale, subsurface phase formation may occur depending on the extent of selective depletion. The γ' formed in the subsurface diffusion zone of NiAl can be rationalized based on consideration of the Ni-Al phase diagram. On the other hand, the accompanying interdiffusion between the adjacent compound phases could also result in the disappearance of any just-formed intermediate

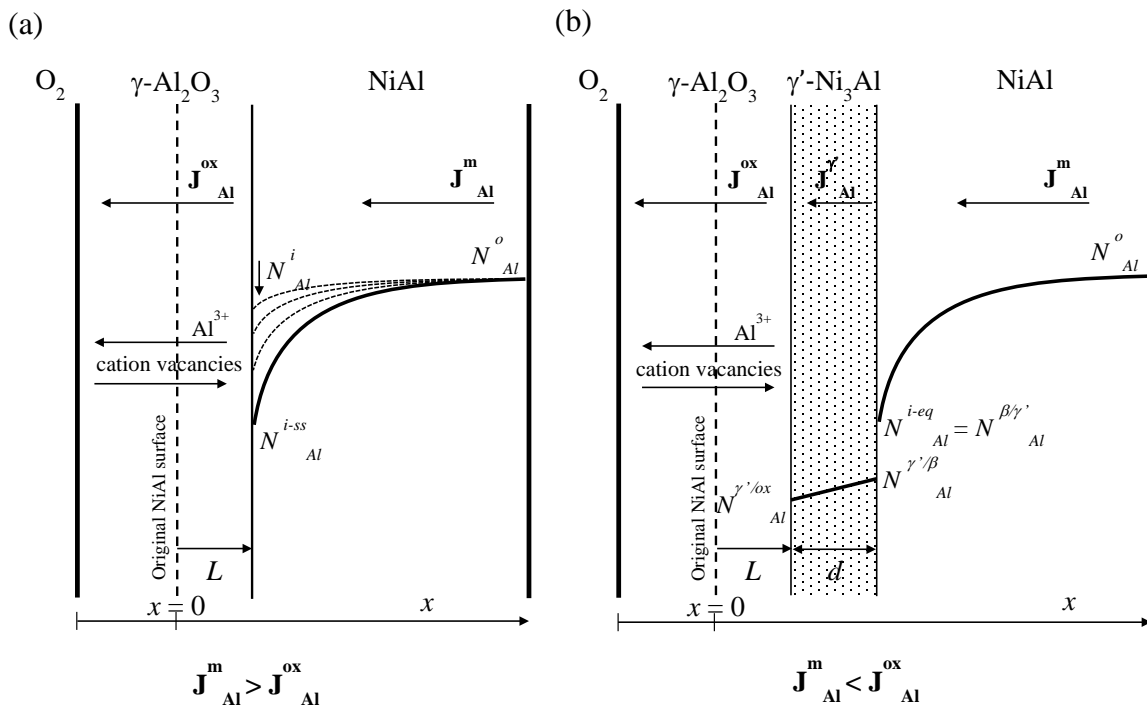


Figure AII.3 Diffusion profile and boundary conditions of NiAl alloy oxidation to form a continuous $\gamma\text{-Al}_2\text{O}_3$ oxide layer: (a) no intermediate phase separation at the metal/oxide interface, (b) Ni_3Al phase formation at the interface. See text for a definition of term shown in the schematics.

phase. Two possible scenarios for NiAl oxidation are shown in Figure AII.3. During oxidation to form Al_2O_3 scale, if the diffusion of Al in the NiAl is not sufficiently rapid to replenish what is being consumed by oxidation, then the limit of β -NiAl stability may be reached such that γ' formation is thermodynamically favorable, Figure AII.3(b). However, if the supply of Al diffusing to the formed γ' eventually exceeds the rate at which Al is being consumed from this layer, then its presence would be expected to diminish or even disappear. In essence, the suppression, formation and even maintenance of the subsurface γ' phase are determined by the combined action of thermodynamic and kinetic considerations. To that end, the competition relation between the Al consumption flux and Al supply flux at the alloy/oxide interface is considered quantitatively in the present study.

To quantitatively interpret the phase formation under various conditions, a diffusion analysis is critical in order to predict the elemental contents at the interface. The quantity and rate of active element consumption are time dependent and directly related to the oxidation kinetics. Furthermore, for conventional thermal oxide growth controlled by ionic diffusion, the parabolic rate law is commonly observed. Therefore, given the nature of parabolic kinetics, the rate of oxidation decreases with increasing time of reaction, which is best represented by the instantaneous rate of oxidation. In addition, during the initial stage of low-temperature oxidation, when the oxide film grows in a thin-film regime with a thickness less than the high field approximation, x_f , a corresponding strong electric field exists across the film due to the fast transport of electrons through electronic tunneling. The growth kinetics in this thin-film regime typically obeys the inverse-logarithmic rate law established by Mott and Cabrera [149–152]. In the present study, the growth kinetics of γ - Al_2O_3 thin-film formation will also be taken into account for the case of low-temperature (i.e., 650 °C) oxidation.

AII.3.1 Al consumption flux during oxidation

AII.3.1.1 Oxide growth obeys parabolic kinetics

In general, for a binary AB alloy exposed to an oxygen containing atmosphere and forming a single-oxide layer B_aO_b , it is often found that oxide growth behavior (steady-state conditions) follows the parabolic rate law according to [147,153],

$$\left(\frac{\Delta m}{A}\right)^2 = k_p t \quad (1)$$

where $\Delta m/A$ is the weight gain of the sample per unit surface area, t is the time and k_p is the parabolic rate constant. In this case, the alloy/oxide interface recession, L , during oxidation (Figure AII.3) is given by,

$$L^2 = k_c t \quad (2)$$

where k_c is the corrosion constant of the alloy, which is related to k_p by the equation $k_c = k_p \left(\frac{aV_m}{bM_o}\right)^2$. Here, V_m is the molar volume of the alloy at the subsurface of alloy/oxide interface, and M_o is the molecular weight of oxygen. In accordance with eq. (1), the instantaneous rate of oxidation, $d(\Delta m/A)/dt$, is given by,

$$\frac{d\left(\frac{\Delta m}{A}\right)}{dt} = \frac{1}{2} \sqrt{\frac{k_p}{t}} \quad (3)$$

Thus, the instantaneous consumption flux of the active solute B leaving the alloy at the alloy/oxide interface, J_B^{ox} , is given by

$$J_B^{ox} = \frac{1}{2} \frac{a}{bM_o} \sqrt{\frac{k_p}{t}} = \frac{1}{2V_M} \sqrt{\frac{k_c}{t}} \quad (4)$$

During the initial period of oxidation, the concentration of B at the alloy/oxide interface, N_B^i , decreases from the bulk value, N_B^o , to some steady-state value, N_B^i , as indicated in Figure AII.3 (a). In accordance with parabolic kinetics, the instantaneous rate of oxidation will change as a

function of both time and N_B^i . To better describe the instantaneous oxidation behavior, an instantaneous parabolic rate constant, q_c , can be introduced to the transient parabolic regime instead of k_c [154,155],

$$q_c = \frac{dL^2}{dt} = 2L \frac{dL}{dt} \quad (5)$$

As shown by Gesmundo et al. [154] and Deal et al. [156], q_c can be approximately defined as $q_c = \frac{2 k_c L b}{k_c + 2 L b}$, where b denotes the initial rate of surface reaction per V_m . The value of b determines the transition time from the transient parabolic to the final equilibrium parabolic kinetics. A typical value of b is $10^{-6} \text{ cm s}^{-1}$ [154,155]. At $t \gg 0$, the steady-state parabolic growth is approached with $q_c = k_c$. In this treatment, the overall consumption rate of B due to selective oxidation is given by,

$$J_B^{ox} = \frac{1}{2V_M} \sqrt{\frac{q_c}{t}} \quad (6)$$

Grabke et al. [85,157] studied NiAl oxidation at various temperatures in which the oxide growth obeyed the parabolic rate law. Even so, it has also been shown that the oxidation behavior of NiAl(110) during the initial stage of oxidation at 650 °C can follow the inverse-logarithmic rate law [158].

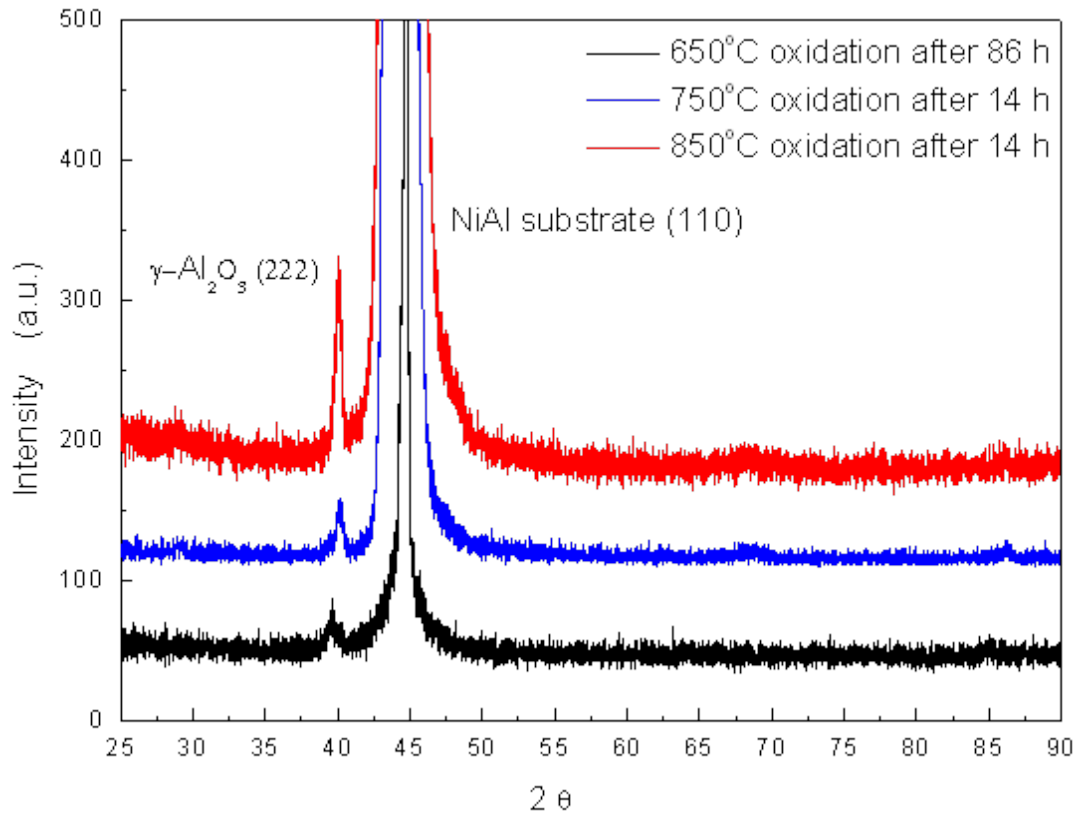


Figure AII.4 XRD scans of various temperature oxide thin films grown on NiAl(110)

It is well established that the oxidation behavior is quite dependent on the temperature and surface orientation of the crystal [85,157,159]. At low enough temperature, the oxidation behavior can also be highly dependent on time as the scale grows from the thin to the thick regime [152,160]. The growth behavior of γ -Al₂O₃ at 650 °C was systematically studied in our previous work [158]. In this current study, the growth kinetics of γ -Al₂O₃ were carefully

Table AII.1 Classical rate constants for the growth kinetics of $\gamma\text{-Al}_2\text{O}_3$ on $\beta\text{-NiAl}$ (110) at given temperatures

Temperature	Growth kinetics	Constants	Values
650 °C	Inverse-logarithmic in the initial stage	A (nm^{-1})	0.302
		B (nm^{-1})	0.0229
650 °C	Parabolic in the thick regime	k_p ($\text{g}^2/\text{cm}^4 \cdot \text{sec}$)	1.61×10^{-16}
750 °C			4.64×10^{-15}
850 °C			8.31×10^{-14}

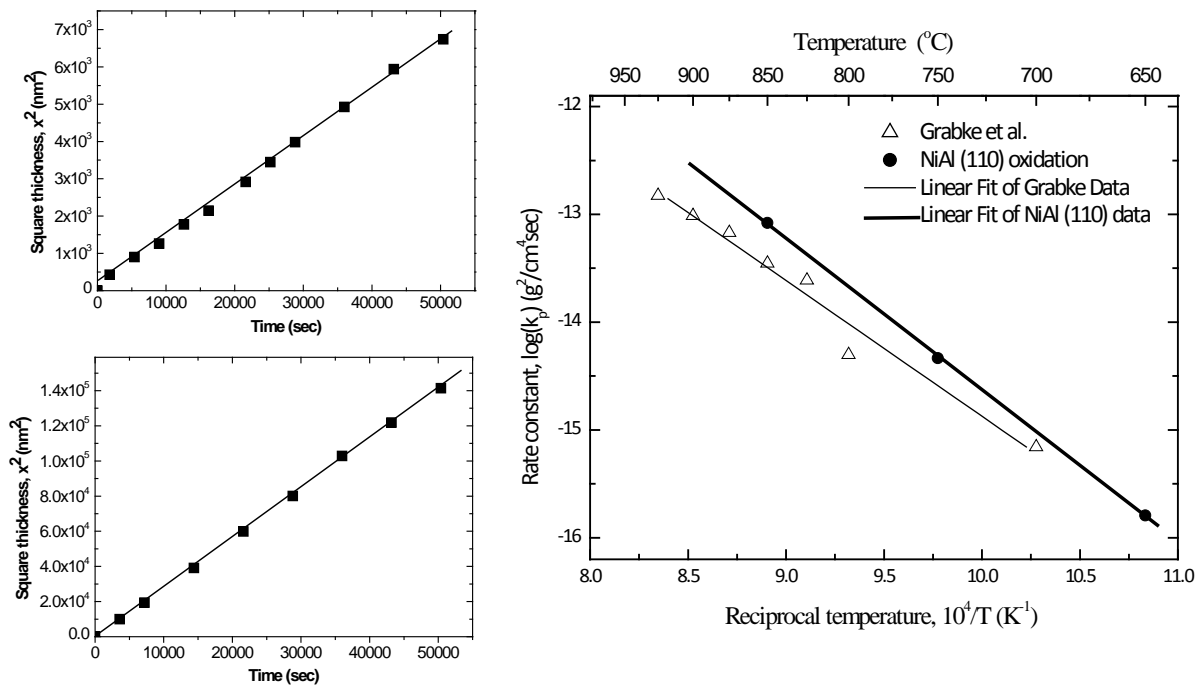


Figure AII.5 Thermogravimetric analyses of NiAl (110) early stage oxidation at 750 (a), and 850 °C (b) shows an ideal parabolic growth, the Arrhenius diagrams of $\log k_p$ vs $1/T$ for oxidation of NiAl (110) was compared with former NiAl oxidation results (c).

measured by isothermal oxidation of NiAl (110) specimens at 750 and 850 °C in air via thermogravimetric analyses. The crystallographic textures of the resulting oxide film after oxidation were characterized by X-ray diffraction using the conventional Bragg–Brentano (θ / 2θ) scan, Figure AII.4. The sharp and small peaks detected at 39.5 ° from all scans corresponded to γ -Al₂O₃ (222) reflections, which indicate a γ -Al₂O₃ (111) oriented film dominated epitaxial growth. The oxidation time selected for each temperature was 14 h at 750 and 850 °C to avoid the transformation of γ -Al₂O₃ to any other transient oxides or α -Al₂O₃ [85,157]. At both temperatures, the oxidation kinetics were found to follow the parabolic rate law with linear correlation coefficients greater than 0.98, Figure AII.5. The measured k_p values are listed in Table AII.1. The Arrhenius diagram for γ -Al₂O₃ growth kinetics on NiAl (110) is compared to that determined by Grabke et al. [157] for NiAl oxidation, Figure AII.5 (c). It can be seen that the parabolic rate constants determined in the present study are almost the same order of magnitude as those measured by Grabke et al., but the latter data show a lower sensitivity to temperature change. Specifically, the activation energy for the γ -Al₂O₃ formation on NiAl (110), $\Delta E = 268.96$ kJ/mol, is higher compared to the polycrystalline substrate, $\Delta E = 237.1$ KJ/mol. The reason for this difference is beyond the scope of this paper.

AII.3.1.2 Oxide growth obeys inverse-logarithmic kinetics

For the initial period of oxide growth, when the film thickness is thinner than the limit of the high field approximation, x_f , a self-generated electric field will be formed which leads to a more rapid ionic transport across the oxide scale [152,160]. In our studies, the diffusion analysis will only consider the thin-film regime (below 50 nm) through oxidation. During this stage, it will be reasonably assumed that the oxide growth will be in accordance with the inverse-logarithmic rate

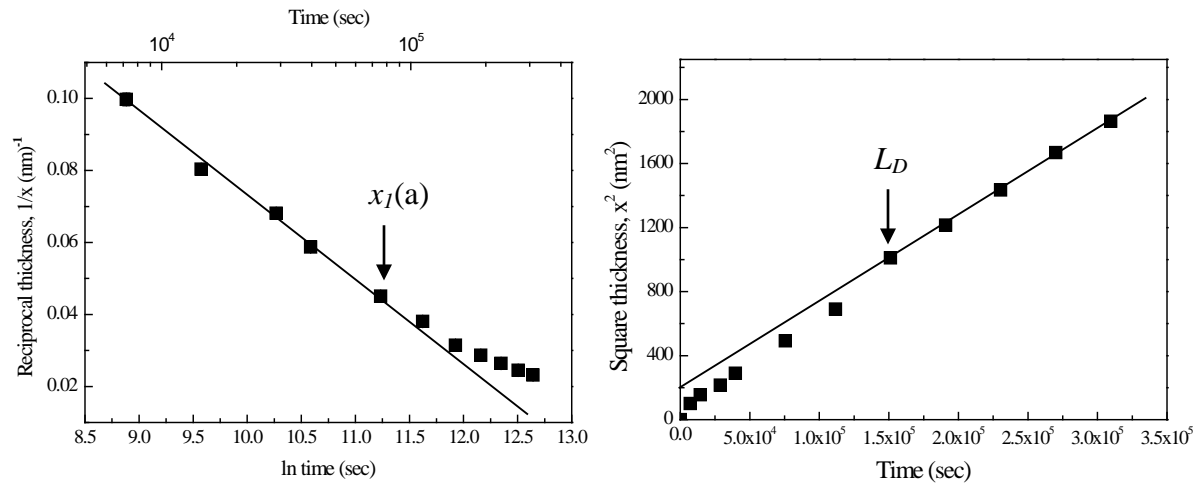


Figure AII.6 Growth kinetics of $\gamma\text{-Al}_2\text{O}_3$ on NiAl(110) alloy at 650°C obey an inverse-logarithmic ($1/x$ vs. $\ln t$) behavior at the initial stage when $x < x_I$ (a), and transit into the parabolic (x^2 vs. t) regime at thicker regime when $x > L_D$ [25].

law. When the film grows thicker than the Debye-Hückel length (L_D), ionic diffusion will become the limiting step for the oxide growth and parabolic kinetics will ensue. A detailed understanding of the growth behavior of the oxidation kinetics at this thin regime is important for better understanding the Al consumption behavior.

Our previous study on NiAl (110) oxidation at a low temperature, 650°C , to form the thin oxide film showed that the $\gamma\text{-Al}_2\text{O}_3$ growth obeys the inverse-logarithmic rate law at the initial stage, Figure AII.6 [158],

$$x = \frac{1}{A - B \ln t} \quad (7)$$

the coefficients of A and B are listed in Table 1, and x is the oxide-film thickness. Therefore, the instantaneous consumption of the selectively oxidized component, J_B^{ox} , in the thin-film regime at 650°C is given by,

$$J_B^{ox} = \frac{a}{V_{ox}} \frac{dx}{dt} = \frac{a}{V_{ox}} \frac{B}{t(A-B \ln t)^2} \quad (8)$$

where V_{ox} is the molar volume of the oxide. Correspondingly, the extent of alloy/oxide interface recession, L_{inv} is,

$$L_{inv} = \frac{a V_m}{V_{ox}} \frac{1}{(A-B \ln t)} \quad (9)$$

All the relevant constants to describe the growth kinetics of γ -Al₂O₃ on β -NiAl are summarized in Table 1.

AII.3.2 Metal supply from the substrate

During oxide formation, the outward migration of B to form a continuous oxide B_aO_b layer on the alloy surface will lead to a depletion of B in the alloy/oxide subsurface, and corresponding enrichment of A. In the case of a moving alloy/oxide interface during oxidation, as presented in Figure AII.3, and assuming that the diffusion coefficients of the two alloy components are independent of alloy composition, the concentration profile of B, $N_B(x,t)$, in the alloy can be found by solving Fick's second law,

$$\frac{\partial N_B}{\partial t} = D \frac{\partial^2 N_B}{\partial x^2} \quad (10)$$

The boundary conditions associated with the present study are defined as,

$$N_B = N_B^i = N_B^o, \text{ at any } x, t = 0;$$

$$N_B = N_B^i, \text{ at } x=L, t > 0;$$

$$N_B = N_B^o, \text{ at } x \gg L, t > 0,$$

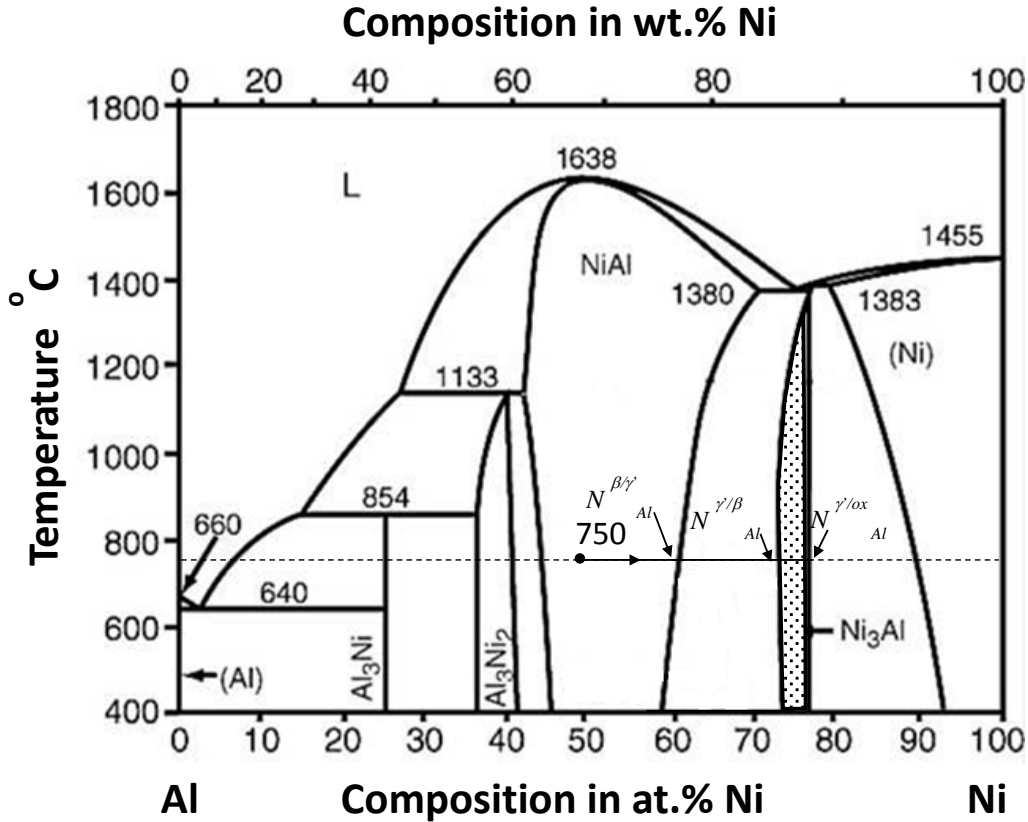


Figure AII.7 Ni-Al binary phase diagram.

where N_B^o and N_B^i are the atom fractions of B in the bulk alloy and at the alloy/oxide interface, respectively. A limiting value for the latter boundary condition can be obtained from the Ni-Al phase diagram, Figure AII.7. In the case of parabolic oxide growth kinetics, the concentration profile of B in the alloy is generally solved to be [153,154,161–163],

$$N_B(x, t) = N_B^i + (N_B^o - N_B^i) \frac{\operatorname{erf}\left(\frac{xR}{2\sqrt{D_B t}}\right) - \operatorname{erf}(u)}{1 - \operatorname{erf}(u)} \quad (11)$$

where D_B is the diffusion coefficient of B in the alloy, R is the square-root of the ratio of the transient parabolic constant, q_c , to the steady-state parabolic constant, k_c , $R = (q_c/k_c)^{\frac{1}{2}}$, and u is the kinetics parameter,

$$u = \frac{1}{2} \frac{L}{\sqrt{D_B t}} R = \frac{1}{2} \sqrt{\frac{q_c}{D_B}} \quad (12)$$

Using Fick's first law, the instantaneous flux of B in the alloy, J_B^m , arriving at the alloy/oxide interface (at $x=L$) can be expressed as,

$$J_B^m = \frac{D_B}{V_m} \frac{dN_B}{dx} = (N_B^o - N_B^i) R \frac{\sqrt{D_B}}{V_m} \frac{\exp(\frac{-x^2}{4D_B t})}{\sqrt{\pi t} [1-\text{erf}(u)]} \quad (13)$$

For the case of inverse-logarithmic oxidation kinetics, the instantaneous oxidation behavior need not consider the transient q_c . This can be done by setting $R = 1$ in eq. (12), so that,

$$u_{inv} = \frac{1}{2} \frac{L_{inv}}{\sqrt{D_B t}} R = \frac{1}{2} \frac{a V_m}{V_{ox}} \frac{1}{(A-B \ln t) \sqrt{D_B t}} \quad (14)$$

A further supply of B is taken into account due to the inward displacement (L) of the alloy-scale interface [163]. The supply rate of B, J_B^i , for such a flux is expressed as,

$$J_B^i = - \frac{N_B^i}{V_m} \frac{dL}{dt} \quad (15)$$

Thus, when the oxide formation kinetics follows parabolic rate law, $J_B^i = \frac{N_B^i}{2V_m} \sqrt{\frac{q_c}{t}}$; whereas,

for the oxidation kinetics follows inverse-logarithmic rate law, $J_{B-inv}^i = \frac{aN_B^i}{V_{ox}} \frac{B}{t(A-B \ln t)^2}$.

AII.3.3 Comparison of Al fluxes at the alloy/oxide interface

Based on the above analysis, the Al supply fluxes, J_{Al}^m and J_{Al}^i , and the Al consumption flux, J_{Al}^{ox} , can be solved according to equations (6, 8, 13, 15), where the diffusion coefficient of Al in NiAl can be sourced from the studies of Wei et al. [117,164,165]. At steady-state, an instantaneous mass balance exists, such that,

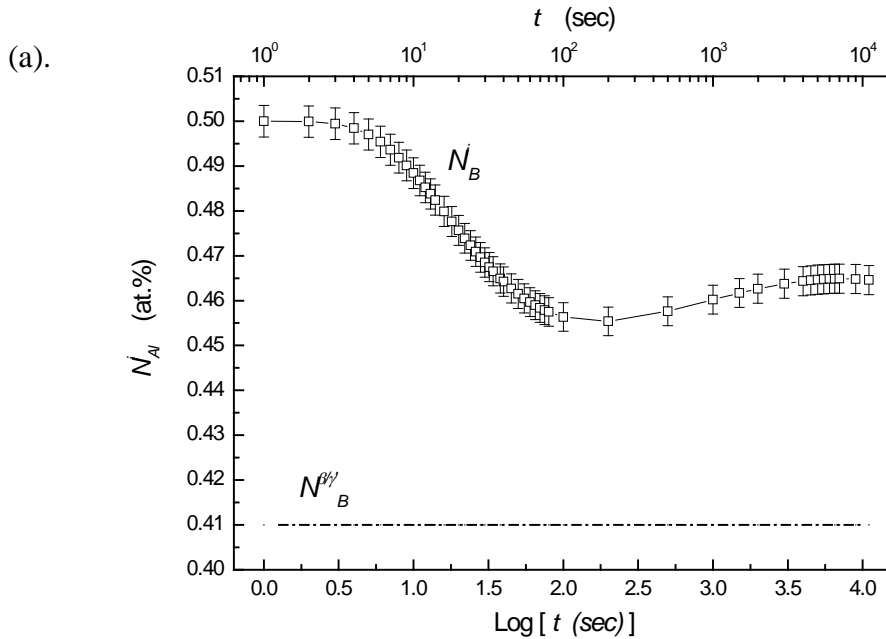
$$J_{Al}^i + J_{Al}^m = J_{Al}^{ox} \quad (16)$$

For the two types of oxide growth kinetics considered, we obtain for the above relation,

$$\text{Inverse-logarithmic: } \frac{aN_{Al}^i}{V_{ox}} \frac{B}{t(A-B\ln t)^2} + (N_{Al}^o - N_{Al}^i) \frac{\sqrt{D_{Al}}}{V_m} \frac{\exp(-u_{inv}^2)}{\sqrt{\pi t} [1 - \text{erf}(u_{inv})]} = \frac{a}{V_{ox}} \frac{B}{t(A-B\ln t)^2} \quad (17)$$

$$\text{Parabolic kinetics: } \frac{N_{Al}^i}{2V_m} \sqrt{\frac{q_c}{t}} + (N_{Al}^o - N_{Al}^i) R \frac{\sqrt{D_{Al}}}{V_m} \frac{\exp(-u^2)}{\sqrt{\pi t} [1 - \text{erf}(u)]} = \frac{1}{2V_M} \sqrt{\frac{q_c}{t}} \quad (18)$$

Therefore, the instantaneous concentration of Al at the alloy/metal interface, N_{Al}^i , can be solved for different growth kinetics as a function of time at different temperatures, as shown in Figure AII.8. At the lower temperature 650 °C oxidation, oxide growth behavior follows inverse-logarithmic kinetics and N_{Al}^i is obtained from eq. (17), Figure AII.8 (a). Whereas, at the higher temperatures of 750 and 850 °C, parabolic kinetics are obeyed and N_{Al}^i is solved from eq. (18), Figure AII.8 (b) and (c). The error bars represent the uncertainty involved in obtaining the data from experiments. Thermodynamically, the new phase formation in the alloy at the alloy/oxide interface will be dictated by N_{Al}^i and whether the Al phase boundary in Figure AII.7 is crossed.



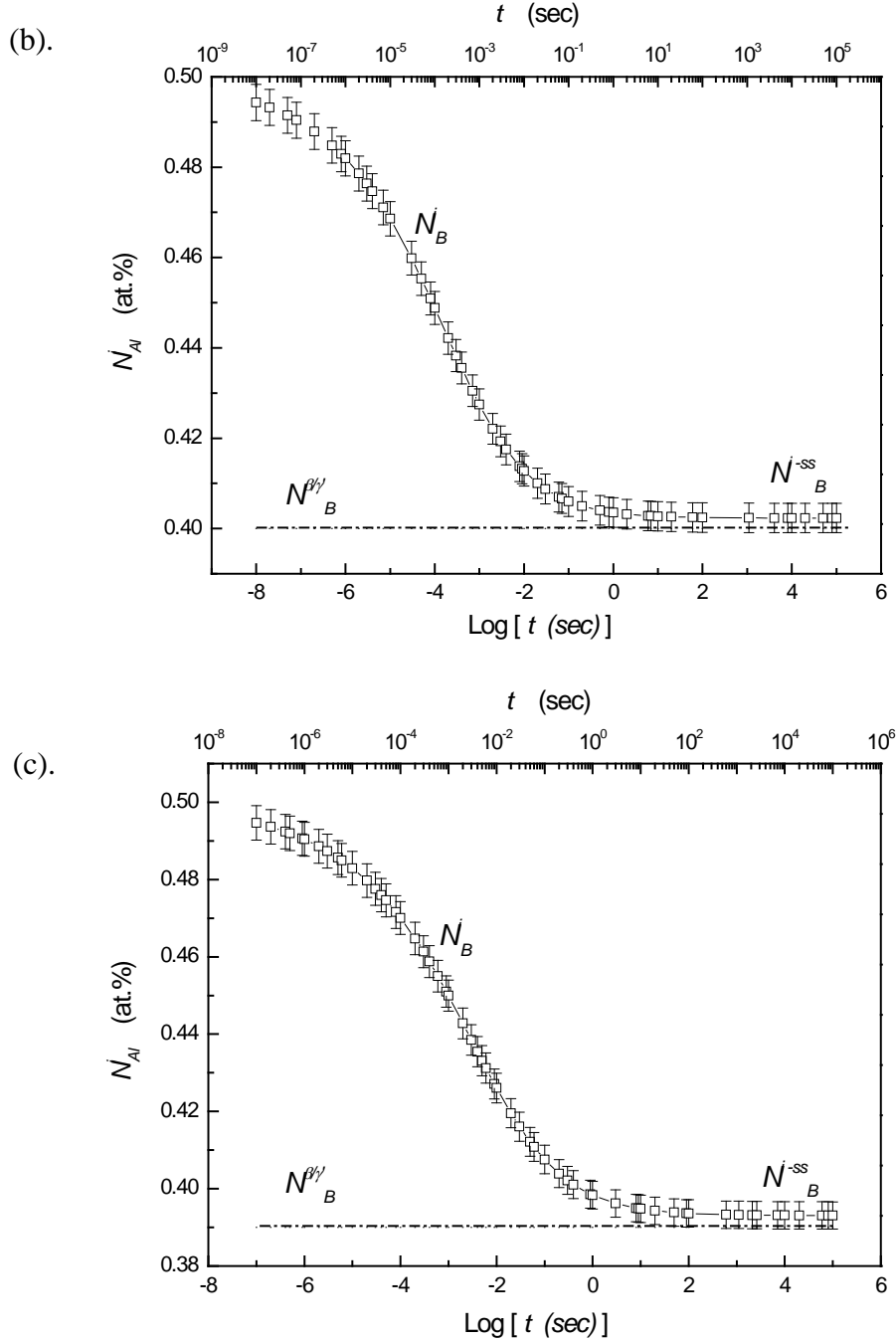


Figure AII.8 Interfacial composition of Al (N_{Al}^i) profile compared with the equilibrium composition of γ' phase formation ($N_{Al}^{\beta/\gamma'}$) at corresponding temperatures. (a). At 650 °C, N_{Al}^i was solved by inverse-logarithmic kinetics according to equation (17); (b) and (c), at 750 and 850°C, N_{Al}^i was obtained from parabolic kinetics according to equation (18).

As shown in Figure AII.8 (a), at 650°C, N_{Al}^i is larger than the Al solvus for equilibrium with γ' , $N_{Al}^{\beta/\gamma'}$. This means that the diffusion of Al in the substrate is fast enough to meet the demands of Al consumption without N_{Al}^i decreasing to $N_{Al}^{\beta/\gamma'}$. Thus, the interfacial concentration deviation of Al will not be sufficient to induce γ' phase formation. Such a result is in agreement with what was found experimentally.

However, with the temperature increasing to 750 °C or 850 °C, N_{Al}^i rapidly diminishes with extended oxidation time, and the minimum of N_{Al}^i is close to that corresponding γ' formation, Figure AII.8 (b) and (c), such that $N_{Al}^i \approx N_{Al}^{\beta/\gamma'}$. Therefore, an abrupt drop in the Al concentration may happen locally at the alloy/oxide interface during oxidation, which would lead to a thermodynamically favorable condition for γ' -Ni₃Al phase formation. This is in accordance with the observations of γ' phase formation at 750 °C for 1 h, Fig. 1. To this point, however, the disappearance of the subsurface γ' with continued oxidation at 750 °C to 2 h or at 850 °C has not been quantitatively interpreted.

The above discussion highlights a thermodynamically sufficient condition for the subsurface γ' formation at oxidation temperatures at and above 750°C. However, a kinetically sufficient condition for phase formation is also necessary in order to maintain the favorable phase in this dynamic oxidation process. In the following section, the stability of an existing subsurface γ' layer will be assessed.

AII.3.4 Kinetic consideration: assumption of γ' -Ni₃Al phase formation

To examine whether a subsurface γ' -Ni₃Al could sustain itself at 750 or 850°C, it will be assumed that this phase formed during early-stage oxidation at both temperatures. In such a scenario, the γ' serves as the medium to supply Al for continued oxide formation.

The Al flux in the γ' , $J_{Al}^{\gamma'}$, can be obtained by setting the boundary conditions to be the limiting composition of the Ni₃Al intermetallic phase at a given temperature. From the Ni-Al binary phase diagram, Figure AII.7, the Ni₃Al phase will have a Ni concentration of ~ 74 at% at a temperature around 750°C. The concentration gradient of Al in the γ' subsurface layer is simplified to be linear, as shown in Figure AII.3(b).

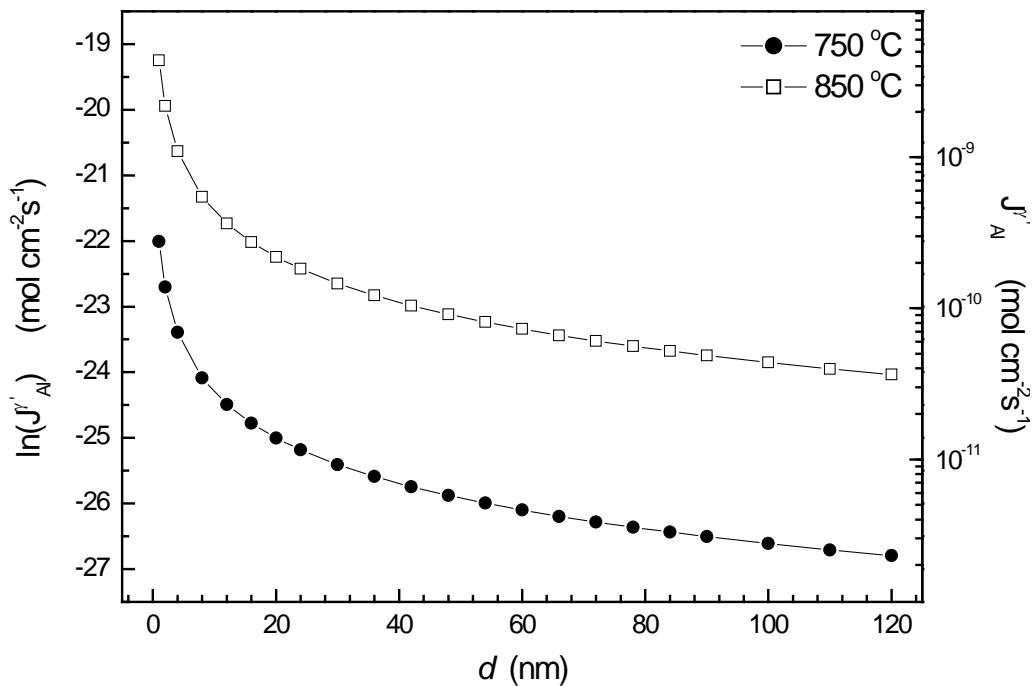


Figure AII.9 The Al flux arrives at the Ni₃Al/ γ -Al₂O₃ interface through the Ni₃Al phase is shown as a function of subsurface γ' layer thickness at 750 and 850°C.

The instantaneous supply flux of Al in the γ' phase, $J_{Al}^{\gamma'-m}$, arriving at the γ' -Ni₃Al/oxide interface can be obtained by Fick's first law,

$$J_{Al}^{\gamma'-m} = \frac{D_{Al}^{\gamma'}}{V_{\gamma'}} \frac{dN_{Al}}{dx} = \frac{D_{Al}^{\gamma'}}{V_{\gamma'}} \frac{(N_{Al}^{\gamma'/\beta} - N_{Al}^{\gamma'/ox})}{d} \quad (19)$$

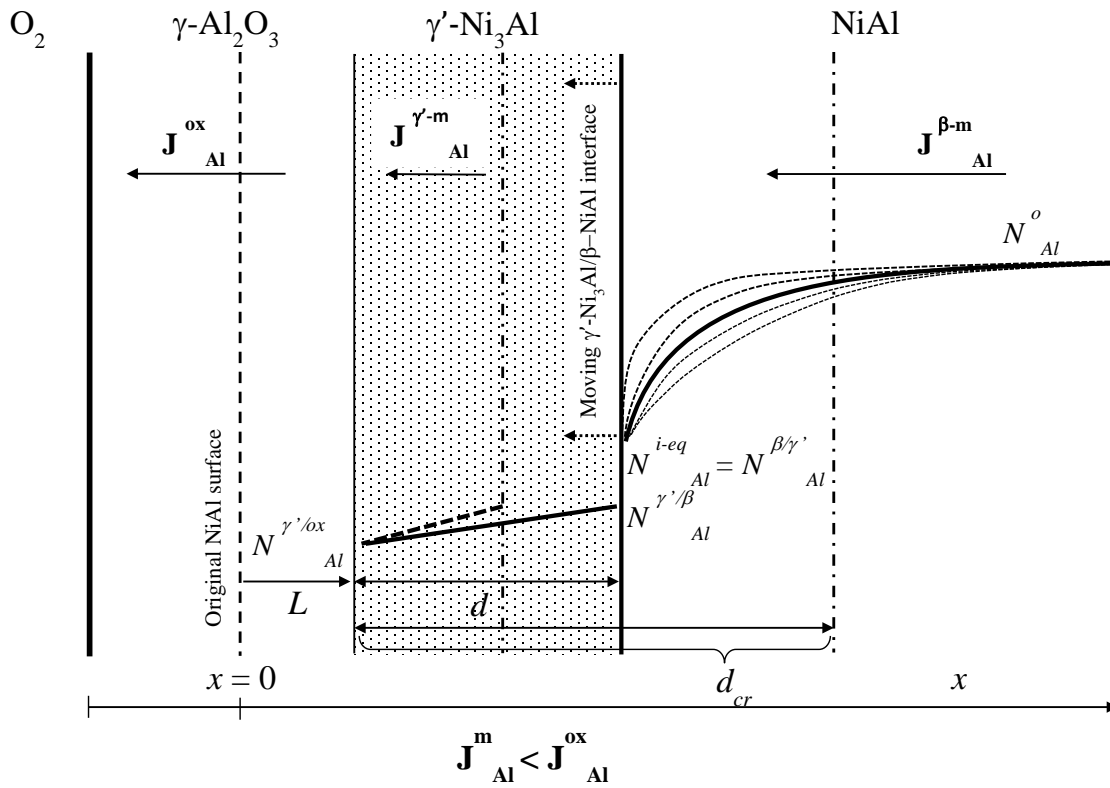


Figure AII.10 Schematics of Ni₃Al phase formation and recession process at the oxide subsurface. See text for a definition of term shown in the schematics. See text for a definition of term shown in the schematics.

where $V_{\gamma'}$ is the molar volume of the γ' , $D_{Al}^{\gamma'}$ is the diffusion coefficient of Al in Ni₃Al [148,166],

$N_{Al}^{\gamma'/\beta}$ and $N_{Al}^{\gamma'/ox}$ are the atom fractions of Al at the Ni₃Al phase boundaries at a given

temperature, and d is the thickness of the γ' subsurface layer, Figure AII.3(b). From eq. (19), it

can be seen that the Al supply flux due to the concentration gradient inside the γ' subsurface

layer, $J_{Al}^{\gamma'-m}$, is inversely proportional to the γ' thickness, d , as shown in Figure AII.9.

Based on the calculated results shown in Figure AII.8 (b), the γ' observed at 750°C after 1 h oxidation is already within the steady-state (apply k_c instead of q_c) parabolic growth regime.

Therefore, eq. (15) was applied to obtain the inward displacement-induced Al flux at the alloy/oxide interface,

$$J_{Al}^{\gamma'-i} = \frac{N_{Al}^{\gamma'/ox}}{2V_{\gamma'}} \sqrt{\frac{k_c}{t}} \quad (20)$$

In addition, the instantaneous consumption of Al during oxidation, J_{Al}^{ox} , is again obtained from eq. (4),

$$J_{Al}^{ox} = \frac{1}{2V_{\gamma'}} \sqrt{\frac{k_c}{t}} \quad (21)$$

In general consideration, the γ' formation and recession process can be determined by the movement of γ'/β interface, v . When v is negative, it connotes that the γ'/β interface moves

towards the oxide and γ' is recessing, as shown in the phase-formation schematic in Figure

AII.10. Therefore, the Al flux balance at the γ'/β interface can be expressed as,

$$v(N_{Al}^{\beta/\gamma'} - N_{Al}^{\gamma'/\beta}) = J_{Al}^{\gamma'-m} - J_{Al}^{\beta-m} \quad (22)$$

where $J_{Al}^{\beta-m}$ is the instantaneous Al supply flux in the β substrate. To achieve a dynamically stable condition, $J_{Al}^{\beta-m}$ will adjust itself in accordance with $J_{Al}^{\gamma'-m}$ to sustain the Al consumption inside of the γ' layer. From eq. (19), $J_{Al}^{\gamma'-m}$ is a function of γ' layer thickness, d . Therefore, the competition relation,

$$J_{Al}^{\gamma'-m} \quad \text{vs} \quad J_{Al}^{\beta-m} \quad (23)$$

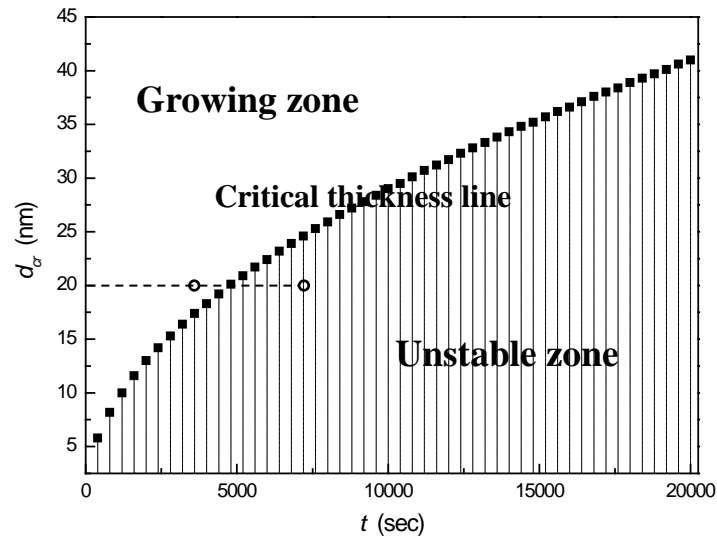
at any given time, will be determined by d and the concentration profile of Al adjacent to the γ'/β interface. At a condition of $J_{Al}^{\gamma'-m} > J_{Al}^{\beta-m}$, $v > 0$ and d will therefore increase with increasing reaction time. However, to quantitatively solve the relation shown by eq. (23), the non-steady state dynamic situation of Al fluxes must be understood. This is not achievable, but a simplified approach can be applied, as will be presented in the following.

The overall Al supply flux from the β substrate and through the γ' layer to sustain the oxide growth can be represented by,

$$J_{Al}^{\gamma'-m} + J_{Al}^{\gamma'-i} + v(N_{Al}^{\beta/\gamma'} - N_{Al}^{\gamma'/\beta}) = J_{Al}^{ox} \quad (24)$$

where the Al consumption flux, J_{Al}^{ox} , is sustained by the Al flux driven by concentration gradient inside of γ' layer, $J_{Al}^{\gamma'-m}$, the Al supply due to the inward displacement of the γ'/oxide interface,

(a).



(b).

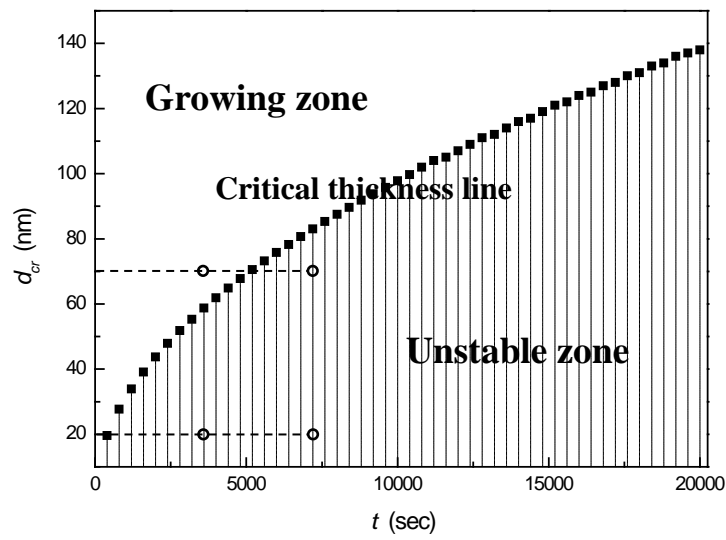


Figure AII.11 Kinetic stability diagram of γ' phase formation as a function of d_{cr} and time indicates the stable/unstable zone of γ' at oxidation temperature of 750 and 850°C.

$J_{Al}^{\gamma'-i}$, and the Al supply due to the inward displacement of the γ'/β interface, $v(N_{Al}^{\beta/\gamma'} - N_{Al}^{\gamma'/\beta})$.

Combining with eq. (22), we obtain the following equation for the whole diffusion process,

$$(J_{Al}^{\gamma'-m} - J_{Al}^{\beta-m}) = J_{Al}^{ox} - (J_{Al}^{\gamma'-m} + J_{Al}^{\gamma'-i}) \quad (25)$$

In order to resolve the relation of eq. (23), a stationary γ'/β interface during oxidation, i.e., $v=0$,

is stipulated. Therefore, from eq. (22), we get $J_{Al}^{\gamma'-m} = J_{Al}^{\beta-m}$. As a result, a balanced fluxes

condition must exist at $v=0$, so that eq. (25) simplifies to,

$$J_{Al}^{ox} = (J_{Al}^{\gamma'-m} + J_{Al}^{\gamma'-i}) \quad (26)$$

This implies a critical thickness of γ' subsurface layer, d_{cr} . The overall situation of the γ' subsurface layer stability is quantitatively summarized in a kinetic stability diagram, Figure AII.11.

At $d < d_{cr}$, $J_{Al}^{ox} < (J_{Al}^{\gamma'-m} + J_{Al}^{\gamma'-i})$ and $v < 0$, so that γ' layer diminishes during oxidation

(Figure AII.10); at $d > d_{cr}$, $J_{Al}^{ox} > (J_{Al}^{\gamma'-m} + J_{Al}^{\gamma'-i})$ and $v > 0$, so that the γ' is kinetically

stabilized and continues to broaden with oxidation time.

As can be seen in the kinetic stability diagram in Figure AII.11(a), the d_{cr} is relatively small (~5 nm) at 750 °C. Thus, the nucleated γ' layer would be stabilized and would broaden due to an Al deficient condition at the $\gamma'/oxide$ boundary (at $d \geq d_{cr}$ condition), which is kinetically stable. With extended time, if the γ' layer grows across the d_{cr} line, it will become kinetically unstable. This is concurrent with J_{Al}^{ox} gradually getting smaller due to a decrease in the instantaneous oxidation kinetics induced by parabolic kinetics. Eventually, the γ' layer disappears. The 750 °C stability diagram clearly displays the kinetically favorable condition of a

20 nm γ' layer formation ($d > d_{cr}$) which becomes kinetically unstable and disappears in the extended oxidation ($d < d_{cr}$). This case shown in Figure AII.11(a) occurs at the oxidation time of around 1.2 h. At this point, there is a build-up of Al inside γ' layer, causing the γ' layer to decay at the γ' -Ni₃Al/ β -NiAl interface and to diminish in overall thickness, which is similar to the process indicated in Figure AII.10. Such a trend was formed experimentally after 2 h oxidation at 750 °C, Figure AII.2. In the same manner, by examining the critical thickness of the γ' layer in the 850°C kinetic stability diagram, Figure AII.11(b), d_{cr} was found to be much larger when compared to 750 °C oxidation (above 20 nm) from the very initial stage, i.e., a thin Ni₃Al layer at the interface would not be kinetically stable. Considering that $\left(J_{Al}^{\gamma'}^{-m} + J_{Al}^{\gamma'}^{-i} \right)$ is inversely proportional to d , Figure AII.9, only a sufficiently large thickness of γ' formation layer can be stabilized to maintain an Al deficient condition, as discussed earlier. Presumably, a γ' layer with $d \geq 70$ nm is likely to be stabilized by achieving the $J_{Al}^{ox} \geq \left(J_{Al}^{\gamma'}^{-m} + J_{Al}^{\gamma'}^{-i} \right)$ at the initial oxidation stage, Figure AII.11(b). However, from Figure AII.8 (c), the steady-state N_{Al}^i deviates slightly from $N_{Al}^{\beta/\gamma'}$. Therefore, a sufficiently thick γ' layer may not be formed to achieve the kinetically favorable condition of γ' layer stabilization.

AII.4 Summary

During β -NiAl (110) oxidation, subsurface γ' -Ni₃Al phase formation can be observed at the alloy/oxide interface, depending on the exposure conditions. A diffusion analysis was applied to understand and interpret the phase formation phenomenon during oxidation.

1. At the low temperature of 650 °C oxidation, the diffusion flux of Al in the substrate is sufficiently fast to supply the Al consumption and to negate the γ' formation. At oxidation temperatures of 750 °C and 850 °C, the interfacial concentration of Al approaches the limiting β -NiAl composition corresponding to equilibrium with γ' -Ni₃Al. Thus, thermodynamic conditions for the phase formation are sufficient.
2. Kinetic analyses indicate that the γ' formation and disappearance process is dependent on the oxidation time and the γ' layer thickness. In order to maintain the kinetically sufficient condition of γ' formation, a thickness criterion is established to determine γ' phase stability quantitatively at corresponding temperature. In order to interpret and predict the growth behavior of γ' formation, a kinetic stability diagram was formulated as a function of γ' layer thickness and time:

At $d > d_{cr}$, γ' phase will be stabilized and broadening towards the substrate during oxidation;

at $d < d_{cr}$, γ' phase will be destabilized and diminish towards the oxide, which eventually disappears during oxidation.

BIBLIOGRAPHY

- [1] Narayanan R, El-Sayed M a. Nano letters 2004;4:1343-1348.
- [2] Mostafa S, Behafarid F, Croy JR, Ono LK, Li L, Yang JC, Frenkel AI, Cuenya BR. Journal of the american chemical society 2010;132:15714-9.
- [3] Nesselberger M, Ashton S, Meier JC, Katsounaros I, Mayrhofer KJJ, Arenz M. Journal of the american chemical society 2011.
- [4] Lei Y, Mehmood F, Lee S, Greeley J, Lee B, Seifert S, Winans RE, Elam JW, Meyer RJ, Redfern PC, Teschner D, Schlögl R, Pellin MJ, Curtiss L a, Vajda S. Science (new york, n.y.) 2010;328:224-8.
- [5] Simonsen SB, Chorkendorff I, Dahl S, Skoglundh M, Sehested J, Helveg S. Journal of the american chemical society 2010;132:7968-75.
- [6] Komanicky V, Iddir H, Chang K-C, Menzel A, Karapetrov G, Hennessy D, Zapol P, You H. Journal of the american chemical society 2009;131:5732-3.
- [7] Schmidt E, Vargas A, Mallat T, Baiker A. Journal of the american chemical society 2009;131:12358-67.
- [8] Mayrhofer KJJ, Blizanac BB, Arenz M, Stamenkovic VR, Ross PN, Markovic NM. The journal of physical chemistry. b 2005;109:14433-40.
- [9] Norskov JK, Rossmeisl J, Logadottir A, Lindqvist L, Kitchin JR, Bligaard T, Jónsson H. The journal of physical chemistry b 2004;108:17886-17892.
- [10] G. Ertl, H. Knozinger, F. Schüth JW. Handbook of Heterogeneous Catalysis, vol. 3. Weinheim, Germany: VCH-Wiley, 2008.
- [11] Matthey D, Wang JG, Wendt S, Matthiesen J, Schaub R, Laegsgaard E, Hammer B, Besenbacher F. Science (new york, n.y.) 2007;315:1692-6.
- [12] Mostafa S, Croy JR, Heinrich H, Cuenya BR. Applied catalysis a: general 2009;366:353-362.

- [13] Kondrat S a., Davies TE, Zu Z, Boldrin P, Bartley JK, Carley AF, Taylor SH, Rosseinsky MJ, Hutchings GJ. *Journal of catalysis* 2011;281:279-289.
- [14] Zanella R. *Journal of catalysis* 2004;222:357-367.
- [15] Arai H, Machida M. *Catalysis today* 1991;10:81-94.
- [16] Kang JH, Menard LD, Nuzzo RG, Frenkel AI. *Journal of the american chemical society* 2006;128:12068-9.
- [17] Lee I, Delbecq F, Morales R, Albiter M a, Zaera F. *Nature materials* 2009;8:132-8.
- [18] Freund H-J, Pacchioni G. *Chemical society reviews* 2008;37:2224-42.
- [19] Nolte P, Stierle A, Jin-Phillipp NY, Kasper N, Schulli TU, Dosch H. *Science (new york, n.y.)* 2008;321:1654-8.
- [20] Magg N, Giorgi JB, Hammoudeh A, Schroeder T, Bäumer M, Freund H-J. *The journal of physical chemistry b* 2003;107:9003-9010.
- [21] Arenz M, Mayrhofer KJJ, Stamenkovic V, Blizanac BB, Tomoyuki T, Ross PN, Markovic NM. *Journal of the american chemical society* 2005;127:6819-29.
- [22] Roldan Cuenya B, Croy JR, Mostafa S, Behafarid F, Li L, Zhang Z, Yang JC, Wang Q, Frenkel AI. *Journal of the american chemical society* 2010;132:8747-56.
- [23] Housmans THM, Koper MTM. *The journal of physical chemistry b* 2003;107:8557-8567.
- [24] Lebedeva NP, Koper MTM, Feliu JM, van Santen R a. *The journal of physical chemistry b* 2002;106:12938-12947.
- [25] Park S, Xie Y, Weaver MJ. *Langmuir* 2002;18:5792-5798.
- [26] Periana R a. *Science* 1998;280:560-564.
- [27] Campbell CT, Parker SC, Starr DE. *Science (new york, n.y.)* 2002;298:811-4.
- [28] Müller P, P. Müller, Kern R. *Surface science* 2000;457:229-253.
- [29] Goldfarb I, Cohen-Taguri G, Grossman S, Levinshtein M. *Physical review b* 2005;72:1-6.
- [30] G. Ertl, H. Knozinger, F. Schüth JW, Gerhard Ertl, Helmut Knözinger, Ferdi Schüth JW. *Handbook of Heterogeneous Catalysis, vol. 3.* Weinheim, Germany: Wiley-VCH, 2008.
- [31] Freund H-J. *Angewandte chemie international edition in english* 1997;36:452-475.

- [32] Alan B. McEwen, Wilhelm F. Maier, Ronald H. Fleming SMB. *Nature* 1987;329:531.
- [33] Huang WJ, Sun R, Tao J, Menard LD, Nuzzo RG, Zuo JM. *Nature materials* 2008;7:308-13.
- [34] Friedrich H, de Jongh PE, Verkleij AJ, de Jong KP. *Chemical reviews* 2009;109:1613-29.
- [35] Li L, Zhang Z, Croy JR, Mostafa S, Cuenya BR, Frenkel AI, Yang JC. *Microsc. microanal.* 2010;16:1192-1193.
- [36] Koningsberger, D.C.; Sayers DE. *Solid state ionics* 1985;16:23-28.
- [37] Sohlberg K, Rashkeev S, Borisevich AY, Pennycook SJ, Pantelides ST. *Chemphyschem : a european journal of chemical physics and physical chemistry* 2004;5:1893-7.
- [38] Nellist PD, Pennycook SJ. *Science* 1996;274:413-415.
- [39] Vila F, Rehr J, Kas J, Nuzzo R, Frenkel a. *Physical review b* 2008;78.
- [40] Pinto H, Nieminen R, Elliott S. *Physical review b* 2004;70:1-11.
- [41] Kwak JH, Hu J, Mei D, Yi C-W, Kim DH, Peden CHF, Allard LF, Szanyi J. *Science (new york, n.y.)* 2009;325:1670-3.
- [42] Carrillo J-MY, Raphael E, Dobrynin AV. *Langmuir : the acs journal of surfaces and colloids* 2010;26:12973-12979.
- [43] Kresse G, Schmid M, Napetschnig E, Shishkin M, Köhler L, Varga P. *Science (new york, n.y.)* 2005;308:1440-2.
- [44] HENRY C. *Surface science reports* 1998;31:231-325.
- [45] Wu SY, Hong M, Kortan AR, Kwo J, Mannaerts JP, Lee WC, Huang YL. *Applied physics letters* 2005;87:91903-91908.
- [46] Bataille AM, Moussy JB, Paumier F, Gota S, Guittet MJ, Gautier-Soyer M, Warin P, Bayle-Guillemaud P, Seneor P, Bouzehouane K, Petroff F. *Applied physics letters* 2005;86:12503-12509.
- [47] Hans-Joachim Freund DWG. *Handbook of heterogeneous catalysis* 2008;3:1309-1338.
- [48] Trueba M, Trasatti SP. *European journal of inorganic chemistry* 2005;2005:3393-3403.
- [49] Nepijko SA, Klimenkov M, Adelt M, Kuhlenbeck H, Schlogl R, Freund HJ. *Langmuir* 1999;15:5309-5313.

- [50] Ealet B, Elyakhloufi M, Gillet E, Ricci M. Thin solid films 1994;250:92-100.
- [51] Ha D, Shin D, Koh G-hyeob, Lee J, Lee S, Ahn Y-seok. Ieee transactions on electron devices 2000;47:1499-1506.
- [52] Caldararu M. Applied surface science 2001;181:255-264.
- [53] Akai D, Hirabayashi K, Yokawa M, Sawada K, Taniguchi Y, Murashige S, Nakayama N, Yamada T, Murakami K, Ishida M. Sensors and actuators a: physical 2006;130-131:111-115.
- [54] Pature NP, Gell M, Jordan EH. Science (new york, n.y.) 2002;296:280-4.
- [55] Gusev EP, Copel M, Cartier E, Baumvol IJR, Krug C, Gribelyuk M a. Applied physics letters 2000;76:176.
- [56] Levin I, Brandon D. Journal of the american ceramic society 1998;81:1995-2012.
- [57] Rohrer GS. Structure and Bonding in Crystalline Materials. Cambridge, UK: Cambridge University Press, 2004.
- [58] K. Shirasuka, H. Yanagida and GY. Yogyo kyokai-shi 1976;84:610-13.
- [59] Freund H. Catalysis today 2006;117:6-14.
- [60] Hansen PL, Wagner JB, Helveg S, Rostrup-Nielsen JR, Clausen BS, Topsøe H, Topsoe H. Science 2002;295:2053-2055.
- [61] Tao FF, Salmeron M. Science (new york, n.y.) 2011;331:171-4.
- [62] Rhee CK, Kim B-J, Ham C, Kim Y-J, Song K, Kwon K. Langmuir : the acs journal of surfaces and colloids 2009;25:7140-7.
- [63] Roldan Cuenya B, Frenkel a., Mostafa S, Behafarid F, Croy J, Ono L, Wang Q. Physical review b 2010;82:1-8.
- [64] Bowker M. Acs nano 2007;1:253-7.
- [65] Bell AT. Science (new york, n.y.) 2003;299:1688-91.
- [66] Campbell CT, Peden CHF. Science (new york, n.y.) 2005;309:713-4.
- [67] Campbell CT. Science (new york, n.y.) 2004;306:234-5.
- [68] Silly F, Castell MR. Physical review letters 2005;94:46103.

- [69] Freund H. *Catalysis today* 2005;100:3-9.
- [70] Farmer JA, Campbell CT. *Science* 2010;329:933-936.
- [71] Wulff GZ. *Z kristallogr.* 1901;34:449.
- [72] Herring C, Nichols M. *Reviews of modern physics* 1949;21:185-270.
- [73] Herring C. *Physical review* 1951;82:87-93.
- [74] Hansen K, Worren T, Stempel S, Lægsgaard E, Bäumer M, Freund H-J, Besenbacher F, Stensgaard I. *Physical review letters* 1999;83:4120-4123.
- [75] Qin Z-H, Lewandowski M, Sun Y-N, Shaikhutdinov S, Freund H-J. *Journal of physical chemistry c* 2008;112:10209-10213.
- [76] R. Kern. In. *Crystal Growth in Science and Technology*. New York: Plenum Press, 1989.
- [77] Henry C. *Progress in surface science* 2005;80:92-116.
- [78] Waters RF, Peri JB, John GS, Seelig HS. *Industrial & engineering chemistry* 1960;52:415-416.
- [79] Schaper H, Doesburg EBM, De Korte PHM, Van Reijen LL. *Solid state ionics* 1985;16:261-265.
- [80] Ren T-Z, Yuan Z-Y, Su B-L. *Langmuir : the acs journal of surfaces and colloids* 2004;20:1531-4.
- [81] Jung Y. *Journal of crystal growth* 1999;196:88-96.
- [82] Wakahara A. *Journal of crystal growth* 2002;236:21-25.
- [83] Shimizu K, Kobayashi K, Thompson GE, Wood GC. *Oxidation of metals* 1991;36:1-13.
- [84] Grabke HJ, Steinhorst M, Brumm M, Wiemer D. *Oxidation of metals* 1991;35:199-222.
- [85] BRUMM MW, GRABKE HJ. *Corrosion science* 1992;33:1677-1690.
- [86] Doychak J, Smialek JL, Mitchell TE. *Metallurgical transactions a* 1989;20:499-518.
- [87] Lykhach Y, Moroz V, Yoshitake M. *Applied surface science* 2005;241:250-255.
- [88] H.-J. Freund, H. Kuhlenbeck MN. *Adsorption on ordered surfaces of ionic solids and thin films*, ed. springer 1993.

- [89] JAEGER R, KUHLENBECK H, FREUND H, WUTTIG M, HOFFMANN W, FRANCHY R, IBACH H. *Surface science* 1991;259:235-252.
- [90] Freund H-J, Dillmann B, Ehrlich D, Haßel M, Jaeger RM, Kuhlenbeck H, Ventrice Jr. C a., Winkelmann F, Wohlrab S, Xu C. *Journal of molecular catalysis* 1993;82:143-169.
- [91] Klimenkov M, Kuhlenbeck H, Nepijko S a. *Surface science* 2003;539:31-36.
- [92] Magg N, Giorgi JB, Hammoudeh A, Schroeder T, Bäumer M, Freund H-J. *The journal of physical chemistry b* 2002;106:8756-8761.
- [93] Stierle A, Renner F, Streitl R, Dosch H, Drube W, Cowie BC. *Science (new york, n.y.)* 2004;303:1652-6.
- [94] Yang J, Schumann E, Levin I, Ruhle M. *Acta materialia* 1998;46:2195-2201.
- [95] Loginova E, Cosandey F, Madey T. *Surface science* 2007;601:L11-L14.
- [96] Gassmann P, Franchy R, Ibach H. *Surface science* 1994;319:95-109.
- [97] Sasaki H, Matsuda T, Kato T, Muroga T, Iijima Y, Saitoh T, Iwase F, Yamada Y, Izumi T, Shiohara Y, Hirayama T. *Journal of electron microscopy* 2004;53:497-500.
- [98] Brivio S, Magen C, Sidorenko a. a., Petti D, Cantoni M, Finazzi M, Ciccacci F, De Renzi R, Varela M, Picozzi S, Bertacco R. *Physical review b* 2010;81:1-10.
- [99] Voyles PM, Grazul JL, Muller D a. *Ultramicroscopy* 2003;96:251-73.
- [100] Jia CL, Lentzen M, Urban K. *Science (new york, n.y.)* 2003;299:870-3.
- [101] Vayssilov GN, Lykhach Y, Migani A, Staudt T, Petrova GP, Tsud N, Skála T, Bruix A, Illas F, Prince KC, Matolín V, Neyman KM, Libuda J. *Nature materials* 2011;10:310-5.
- [102] Enterkin J a, Poepfelmeier KR, Marks LD. *Nano letters* 2011:0-4.
- [103] David B. Williams CBC. *Transmission Electron Microscopy: A Textbook for Materials Science*. Springer, 2009.
- [104] Egerton RF. *Electron Energy-Loss Spectroscopy in the Electron Microscope*. Springer, 2011.
- [105] Varela M, Gazquez J, Pennycook SJ. *Mrs bulletin* 2012;37:29-35.
- [106] Gazquez J, Luo W, Oxley MP, Prange M, Torija M a, Sharma M, Leighton C, Pantelides ST, Pennycook SJ, Varela M. *Nano letters* 2011;11:973-6.

- [107] Martin N, Knudsen J, Blomberg S, Gustafson J, Andersen J, Lundgren E, Ingelsten HH, Carlsson P-a., Skoglundh M, Stierle a., Kresse G. *Physical review b* 2011;83:1-5.
- [108] Kourkoutis LF, Xin HL, Higuchi T, Hotta Y, Lee JH, Hikita Y, Schlom DG, Hwang HY, Muller D a. *Philosophical magazine* 2010;90:4731-4749.
- [109] Levin I, Brandon D. *Philosophical magazine letters* 1998;77:117-124.
- [110] Tilley DB, Eggleton RA. *Clays and clay minerals* 1996;44:658-664.
- [111] Doychak JK, Mitchell TE. High temperature oxidation of beta -nial. In: vol. 39. 1985. pp. 475-484.
- [112] Yu R, Hou PY. *Applied physics letters* 2007;91:011907.
- [113] Bauer E, van Der Merwe J. *Physical review b* 1986;33:3657-3671.
- [114] Frank FC, van Der Merwe JH. *Proceedings of the royal society a: mathematical, physical and engineering sciences* 1949;198:216-225.
- [115] Hellwig O. *Thin solid films* 1998;318:201-203.
- [116] Meier GH, Birks N, Pettit FS. *Introduction to the High-temperature Oxidation of Metals*. New York: Cambridge University Press, 2006.
- [117] Shankar S, Seigle LL. *Metallurgical transactions a* 1978;9:1467-1476.
- [118] BOBETH M, BOBETH, M, E. Bischoff, E. Schumann, M. Rockstroh MR. *Corrosion science* 1995;37:657-670.
- [119] Frenken J, Stoltze P. *Physical review letters* 1999;82:3500-3503.
- [120] Iddir H, Komanicky V, Ogut S, You H, Zapol P. *Journal of physical chemistry c* 2007;111:14782-14789.
- [121] Kaischew R. *Fortscht. miner.* 1960;38:7.
- [122] Bogicevic A, Jennison D. *Physical review letters* 1999;82:4050-4053.
- [123] Periana R a. *Science* 1998;280:560-564.
- [124] Shao-Horn Y, Sheng WC, Chen S, Ferreira PJ, Holby EF, Morgan D. *Topics in catalysis* 2007;46:285-305.
- [125] Small MW, Sanchez SI, Marinkovic NS, Frenkel AI, Nuzzo RG. *Acs nano* 2012;6:5583-95.

- [126] Roldan Cuenya B, Alcántara Ortigoza M, Ono L, Behafarid F, Mostafa S, Croy J, Paredis K, Shafai G, Rahman T, Li L, Zhang Z, Yang J. *Physical review b* 2011;84:1-14.
- [127] Paredis K, Ono LK, Behafarid F, Zhang Z, Yang JC, Frenkel AI, Cuenya BR. *Journal of the american chemical society* 2011;133:13455-64.
- [128] Uhl A, Sainio J, Freund H. *Surface science* 2007;601:5605-5610.
- [129] Sun K, Liu J, Nag N, Browning ND. *Catalysis letters* 2002;84:193-199.
- [130] Li D, Yu Q, Li S-S, Wan H-Q, Liu L-J, Qi L, Liu B, Gao F, Dong L, Chen Y. *Chemistry - a european journal* 2011;17:5668-5679.
- [131] Aaron Deskins N, Mei D, Dupuis M. *Surface science* 2009;603:2793-2807.
- [132] Kwak JH, Hu J, Lukaski A, Kim DH, Szanyi J, Peden CHF. *Journal of physical chemistry c* 2008;112:9486-9492.
- [133] Harding C, Habibpour V, Kunz S, Farnbacher AN-S, Heiz U, Yoon B, Landman U. *Journal of the american chemical society* 2009;131:538-48.
- [134] Fu Q, Li W-X, Yao Y, Liu H, Su H-Y, Ma D, Gu X-K, Chen L, Wang Z, Zhang H, Wang B, Bao X. *Science (new york, n.y.)* 2010;328:1141-4.
- [135] Challa SR, Delariva AT, Hansen TW, Helveg S, Sehested J, Hansen PL, Garzon F, Datye AK. *Journal of the american chemical society* 2011;133:20672-5.
- [136] Egerton RF. *Electron Energy-Loss Spectroscopy in the Electron Microscope*. New York: Plenum Press, 1986.
- [137] Egerton RF. *Reports on progress in physics* 2009;72:016502.
- [138] Ahn C C, Krivanek O L, Burgner R P DMM and SPR. *EELS Atlas A Reference Collection of Electron Energy Loss Spectra Covering All Stable Elements*. Gatan, Inc, 1983.
- [139] Jiang N, Spence JCH. *Ultramicroscopy* 2006;106:215-9.
- [140] Niluis N, Wallis T, Ho W. *Physical review letters* 2003;90:2-5.
- [141] Vitos L. *Surface science* 1998;411:186-202.
- [142] Sankaranarayanan S, Ramanathan S. *Physical review b* 2008;78:1-17.
- [143] Miracle DB. *Acta metallurgica et materialia* 1993;41:649-684.

- [144] Saunders S, Monteiro M, Rizzo F. Progress in materials science 2008;53:775-837.
- [145] Zhang Z, Li L, Yang JC. Acta materialia 2011;59:5905–5916.
- [146] Fujimura T, Tanaka S-I. Acta materialia 1997;45:4917-4921.
- [147] Young D, Gleeson B. Corrosion science 2002;44:345-357.
- [148] Fujiwara K. Acta materialia 2002;50:1571-1579.
- [149] Mott NF. Transactions of the faraday society 1939;35:1175.
- [150] Mott NF. Transactions of the faraday society 1940;35:472.
- [151] Mott NF. Transactions of the faraday society 1947;43:429.
- [152] Cabrera N, Mott NF. Reports on progress in physics 1949;12:163-184.
- [153] Carter P, Gleeson B, Young D. Acta materialia 1996;44:4033-4038.
- [154] Gesmundo F, Castello P, Viani F, Philibert J. Oxidation of metals 1997;47:91-115.
- [155] Gesmundo F, Castello P, Viani F, Philibert J. Oxidation of metals 1997;47:91-115.
- [156] Deal BE, Grove a. S. Journal of applied physics 1965;36:3770.
- [157] Grabke HJ. Intermetallics 1999;7:1153-1158.
- [158] Zhang Z, Jung K, Li L, Yang JC. Journal of applied physics 2012;111:034312.
- [159] Heuer AH, Reddy A, Hovis DB, Veal B, Paulikas A, Vlad A, Rühle M. Scripta materialia 2006;54:1907-1912.
- [160] Atkinson A. Reviews of modern physics 1985;57:437.
- [161] Gesmundo F, Viani F. Oxidation of metals 1986;25:269-282.
- [162] Gesmundo F, Viani F, Niu Y, Douglass DL. Oxidation of metals 1993;40:373-393.
- [163] Wagner C. Journal of the electrochemical society 1952;99:369.
- [164] Wei H, Sun X, Zheng Q, Guan H, Hu Z. Acta materialia 2004;52:2645-2651.
- [165] Kim S, Chang YA. Metallurgical and materials transactions a 2000;31:1519-1524.
- [166] Cserhati C. Intermetallics 2003;11:291-297.